

The GALAH+ survey: Third data release

Sven Buder^{1,2,3*}, Sanjib Sharma^{2,4}, Janez Kos⁵, Anish M. Amarsi⁶, Thomas Nordlander^{1,2}, Karin Lind^{3,7}, Sarah L. Martell^{2,8}, Martin Asplund⁹, Joss Bland-Hawthorn^{2,4}, Andrew R. Casey^{10,11}, Gayandhi M. De Silva^{12,13}, Valentina D’Orazi¹⁴, Ken C. Freeman^{1,2}, Michael R. Hayden^{2,4}, Geraint F. Lewis⁴, Jane Lin^{1,2}, Katharine J. Schlesinger¹, Jeffrey D. Simpson^{2,8}, Dennis Stello^{4,8,15}, Daniel B. Zucker^{13,16}, Tomaž Zwitter⁵, Kevin L. Beeson⁵, Tobias Buck¹⁷, Luca Casagrande^{1,2}, Jake T. Clark¹⁸, Klemen Čotar⁵, Gary S. Da Costa^{1,2}, Richard de Grijs^{13,16,19}, Diane Feuillet^{3,20}, Jonathan Horner¹⁸, Prajwal R. Kafle²¹, Shourya Khanna²², Chiaki Kobayashi^{2,23}, Fan Liu²⁴, Benjamin T. Montet⁸, Govind Nandakumar^{1,2}, David M. Nataf²⁵, Melissa K. Ness^{26,27}, Lorenzo Spina^{2,11,28}, Thor Tepper-García^{2,4,29}, Yuan-Sen Ting (丁源森)^{1,30,31,32}, Gregor Travençolo²⁰, Rok Vogrinčič⁵, Robert A. Wittenmyer¹⁸, Rosemary F. G. Wyse²⁵, Maruša Žerjal¹
and the GALAH Collaboration

Affiliations are listed at the end of the paper

Accepted 2021 April 27. Received 2021 April 26; in original form 2020 November 5

ABSTRACT

The ensemble of chemical element abundance measurements for stars, along with precision distances and orbit properties, provides high-dimensional data to study the evolution of the Milky Way. With this third data release of the Galactic Archaeology with HERMES (GALAH) survey, we publish 678 423 spectra for 588 571 mostly nearby stars (81.2 per cent of stars are within <2 kpc), observed with the HERMES spectrograph at the Anglo-Australian Telescope. This release (hereafter GALAH+ DR3) includes all observations from GALAH Phase 1 (bright, main, and faint survey, 70 per cent), K2-HERMES (17 per cent), TESS-HERMES (5 per cent), and a subset of ancillary observations (8 per cent) including the bulge and >75 stellar clusters. We derive stellar parameters T_{eff} , $\log g$, $[\text{Fe}/\text{H}]$, v_{mic} , v_{broad} , and v_{rad} using our modified version of the spectrum synthesis code Spectroscopy Made Easy (SME) and 1D MARCS model atmospheres. We break spectroscopic degeneracies in our spectrum analysis with astrometry from *Gaia* DR2 and photometry from 2MASS. We report abundance ratios $[\text{X}/\text{Fe}]$ for 30 different elements (11 of which are based on non-LTE computations) covering five nucleosynthetic pathways. We describe validations for accuracy and precision, flagging of peculiar stars/measurements and recommendations for using our results. Our catalogue comprises 65 per cent dwarfs, 34 per cent giants, and 1 per cent other/unclassified stars. Based on unflagged chemical composition and age, we find 62 per cent young low- α , 9 per cent young high- α , 27 per cent old high- α , and 2 per cent stars with $[\text{Fe}/\text{H}] \leq -1$. Based on kinematics, 4 per cent are halo stars. Several Value-Added-Catalogues, including stellar ages and dynamics, updated after *Gaia* eDR3, accompany this release and allow chrono-chemodynamic analyses, as we showcase.

Key words: methods: data analysis – methods: observational – surveys – stars: abundances – stars: fundamental parameters.

1 INTRODUCTION

During the history of the Milky Way, the abundances of the different elements that make up the Galaxy’s stars and planets have continually changed, as a result of the processing of the interstellar medium by successive generations of stars. As a result, the study of the elemental abundances in stars provides a direct record of the Galaxy’s history of star formation and evolution – a fact that has, in recent years, given birth to the science of Galactic Archaeology.

Until recently, however, observational limitations meant that the data available to answer the questions of how the Milky Way formed

and evolved was restricted to a few hundred or thousand stars with high-quality element abundances in our Solar neighbourhood (see e.g. Edvardsson et al. 1993; Nissen & Schuster 2010; Bensby, Feltzing & Oey 2014). In the last decade, advances in multi-object observations made by spacecraft (such as *Gaia*) and ground-based facilities have brought about a revolution in the field of Galactic Archaeology. Where once the field was forced to focus on single-star population studies, it is now possible to carry out surveys that allow large-scale structural analyses.

Due to the intrinsic difficulty in determining the distances of stars, studies of the chemodynamical evolution of our Milky Way were previously restricted to nearby stars which were mapped by the *Hipparcos* satellite (ESA 1997; Perryman et al. 1997; van Leeuwen 2007). In the era of the *Gaia* satellite (Gaia Collaboration 2016a, b,

* E-mail: sven.buder@anu.edu.au

2018), we can now use astrometric and photometric observables and their physical relations with spectroscopic quantities to improve the analysis of spectra and thus the estimation of element abundances.

The connections between the chemical compositions and dynamics of stars across the vast populations in our Galaxy are a topic of significant ongoing research. Although we speak of the Milky Way in terms of the thin and thick disc (Yoshii 1982; Gilmore & Reid 1983), the bulge (Barbuy, Chiappini & Gerhard 2018), and the stellar halo (Helmi 2020) as its main components (Bland-Hawthorn & Gerhard 2016), we understand that the Galaxy is more than a superposition of independent populations. With the data now at hand, we can analyse the Galaxy from a chemodynamical perspective, and use stars of different ages as time capsules to trace back the formation history of our Galaxy (see e.g. Rix & Bovy 2013; Bland-Hawthorn et al. 2019). As one example, the most recent data release from *Gaia* has enabled significant leaps in our understanding of the enigmatic Galactic halo (for an overview see e.g. Helmi 2020). 6D phase space information from *Gaia* has revealed a large population of stars in the Solar neighbourhood that stand out against the smooth halo background as a coherent dynamical structure, pointing to a significant accretion event that is currently referred to as ‘*Gaia*–Enceladus–Sausage’ (GES) a combination of ‘*Gaia*–Enceladus’ (Helmi et al. 2018) and ‘*Gaia* Sausage’ (Belokurov et al. 2018). Additionally, while we would expect the chemical composition of stars to be correlated with their ages and formation sites (see e.g. Minchev et al. 2017), observations can now clearly demonstrate these connections (see e.g. Feuillet et al. 2018; Buder et al. 2019), and can also demonstrate that stars within our Solar neighbourhood have experienced significant radial migration through their lifetimes (see e.g. Frankel et al. 2018; Hayden et al. 2020).

Despite these significant advances, the full detail of our Galaxy’s formation and history still elude us. Many of the pieces that make up that puzzle are presently missing, or remain contentious. As a result, a number of questions still remain to be answered. These include the discrete merger history of our Milky Way, the (non-)existence of an *in situ* halo and the reason for the sharp transition from formation of stars with high α -element abundances in what has historically been called the ‘thick disc’ to younger stars with Solar-like α -element abundances in the ‘thin disc’. We have learnt a great deal about contributions of supernovae to element abundances, starting from the foundational work by Burbidge et al. (1957), and how we can use diagrams displaying element abundances, e.g. in [Fe/H] versus $[\alpha/\text{Fe}]$ diagrams, as diagnostic tools of stellar and Galactic evolution. These advances in our understanding are largely thanks to the pioneering and seminal studies by Tinsley (1979, 1980) and others, building on the trail-blazing observational achievements of Wallerstein (1962) and others. To honour the fundamental contributions by Beatrice M. Tinsley and George Wallerstein, connecting the contributions of SNIa and SNII with element abundances in the [Fe/H] versus $[\alpha/\text{Fe}]$ diagrams, we will hereafter refer to these as the ‘Tinsley–Wallerstein diagrams’.

Previous and ongoing spectroscopic surveys by collaborations like RAVE (Steinmetz et al. 2020a,b), *Gaia*–ESO (Gilmore et al. 2012), SDSS-IV APOGEE (Ahumada et al. 2020), and LAMOST (Cui et al. 2012; Xiang et al. 2019) have certainly shed light on several of these outstanding questions. Answering them completely, requires more and/or better data to map out the correlations between stellar ages, abundances, and dynamics. Upcoming surveys like SDSS-V (Kollmeier et al. 2017), WEAVE (Dalton et al. 2018), 4MOST (de Jong et al. 2019), and PFS (Takada et al. 2014) will certainly continue to broaden our capabilities and understanding surrounding our Galaxy’s physical and chemical evolution. The data currently

at hand, derived from spectroscopy, photometry, astrometry, and asteroseismology, provide high-dimensional information, and we must develop methods to extract the most accurate and precise information from them (for reviews on this see e.g. Nissen & Gustafsson 2018; Jofré, Heiter & Soubiran 2019).

The recent growth in the quantity of available spectroscopic stellar data has delivered a new technique to galactic archaeologists – namely ‘Chemical Tagging’, which allows the identification of stars that formed together using their chemical composition and an understanding of the astrophysics driving the dimensionality of chemical space. This technique is proving a vital tool, enabling us to observationally isolate and characterize the building blocks of our Galaxy. As a result, it remains a major science driver for the GALactic Archaeology with HERMES¹ (GALAH) collaboration² (De Silva et al. 2015). With the large variety of nucleosynthetic channels that can enrich the birth material of stars (see e.g. Kobayashi, Karakas & Lugaro 2020), the hypothesis is that we should be able to disentangle stars with different enrichment patterns, provided we observe enough elements with different enrichment origins. The success of some chemical tagging experiments (see e.g. Kos et al. 2018; Price-Jones et al. 2020) is challenged by the broad similarities in chemical abundance in populations like the low- α disc (see e.g. Ness et al. 2018), and by the small but real inhomogeneities even within star clusters (Liu et al. 2016a, b). To put detailed chemical tagging into action, we will need a massive data set (see e.g. Ting, Conroy & Rix 2016) consisting of measurements made with outstanding precision (Ting & Weinberg 2021).

The publication of the previous second data release of the GALAH survey (Buder et al. 2018), entirely based on observations as part of GALAH Phase 1 with the HERMES spectrograph at the Anglo-Australian Telescope, has provided for the community abundance measurements of 23 elements based on 342 682 spectra. Observations for this phase have continued and we are able to publish all 476 863 spectra for 443 843 stars of the now finished Phase 1 observations as part of this third data release. In parallel, spectroscopic follow-up observations of K2 and TESS targets have been performed with HERMES and we are able to also include these observations (112 943 spectra for 99 152 K2-HERMES stars and 34 263 spectra for 26 249 TESS-HERMES stars) in our release. We further include ancillary observations of 54 354 spectra for 28 205 stars in fields towards the bulge and more than 75 stellar clusters. Given the significant contribution from these programmes to this GALAH release, we will hereafter refer to the release as GALAH+ DR3.

For the previous (second) data release of the GALAH survey (Buder et al. 2018), we made use of the data-driven tool *The Cannon* (Ness et al. 2015) to improve both the speed and the precision of the spectroscopic analysis. This was performed almost entirely without non-spectroscopic information for individual stars, using a ‘training set’ of stars with careful by-hand analysis. Although the data-driven approaches were successful for the majority of GALAH DR2 stars, we know that these approaches can suffer from signal aliasing (e.g. moving outliers closer to the main trends), can learn unphysical correlations between the input data and the output stellar labels, and that the results are not necessarily valid outside the parameter space of the training set. As part of this study, we aim to assess how accurately and precisely the stellar parameters and abundances were estimated by the data-driven approaches. We have therefore adjusted our approach to the analysis of the whole sample and

¹High Efficiency and Resolution Multi-Element Spectrograph

²<https://www.galah-survey.org>

now restrict ourselves to smaller wavelength segments of the four wavelength windows observed by HERMES per star with reliable line information for spectrum synthesis instead and include even more grids for an accurate computation of line strengths when the conditions depart from local thermodynamic equilibrium (LTE; e.g. Mihalas & Athay 1973; Asplund 2005; Amarsi et al. 2020).

The publication of *Gaia* DR2 (Gaia Collaboration 2018; Lindegren et al. 2018) provided phase space information up to 6 dimensions (coordinates, proper motions, parallaxes, and sometimes also radial velocities) for 1.3 billion stars, and having this information available for essentially all (99 per cent) stars in GALAH has allowed us to make major improvements to our stellar analysis. By combining our knowledge of the (absolute) photometry and spectroscopy of stars, we can break several of the degeneracies in our standalone spectroscopic analyses, which arise due to the fact that absorption lines do not always change to a detectable level as a function of stellar atmospheric parameters. The data analysis process for this third data release from the GALAH collaboration makes use of fundamental correlations, and this quantifiably improves the accuracy and precision of our measurements.

As large Galactic Archaeology-focused surveys continue to collect data (like GALAH in its ongoing Phase 2), the overlap between them increases. This enables us to compare results when analysing stars in the overlap, which have the same stellar labels (stellar parameters, abundances, or other non-spectroscopic stellar information), and it also allows us to propagate labels from one survey on to another (see e.g. Casey et al. 2017; Ho et al. 2017; Xiang et al. 2019; Nandakumar et al. 2020; Wheeler et al. 2020). This label propagation makes it possible to combine these complementary surveys for global mapping of stellar properties and abundances, and we show an example of this in Section 8, placing GALAH+ DR3 data in context with the APOGEE and LAMOST surveys.

This paper is structured as follows: We describe our target selection, observations, and reductions in Section 2. While the target selection and observation of the several projects like K2-HERMES and TESS-HERMES were slightly different from the main GALAH survey, we have reduced and analysed all data (combined under the term GALAH+) in a consistent and homogeneous way. The analysis of the reduction products is described in Section 3, focusing on the description of the general workflow of the analysis group and highlighting changes with respect to the previous release (GALAH DR2). Sections 4 and 5 address the validation efforts for stellar parameters and element abundances, respectively. These address the accuracy and precision of these labels as well as our algorithms to identify and flag peculiar measurements or peculiar stars. Based on experience with the data set, we stress the importance of the flags, but also how complex the flagging estimates are, with several examples of peculiar abundance patterns. We also highlight possible caveats (and possibly peculiar physical correlations) of our analysis in Section 6. We present the contents of the main catalogue of this data release in Section 7. In this section, we also present the Value-Added-Catalogues (VACs) that accompany this release, namely a VAC (see Section 7.3.1) created by cross-matching our targets with *Gaia* eDR3 (Gaia Collaboration 2021) and the distance estimates by Bailer-Jones et al. (2021), a VAC (see Section 7.3.2) with estimates (such as stellar ages and masses) from isochrone fitting, a VAC (see Section 7.3.3) with stellar kinematic and dynamic estimates, a VAC (see Section 7.3.4) with radial velocity estimates based on different methods, and a VAC (see Section 7.3.5) on parameters of binary systems. While we made use of data from *Gaia* DR2 (Gaia Collaboration 2018) for our spectroscopic analysis, we also provide a second version of each of our catalogues with

new cross-matches and VACs with updated data making use of *Gaia* eDR3 (Gaia Collaboration 2021), which was published shortly after our data release and supersedes *Gaia* DR2. We describe all changes of the catalogues between version 1 (based on *Gaia* DR2) and version 2 (with VACs now based on *Gaia* eDR3) in Section 7.1. We highlight the scientific potential of the data in this release in context by using the combination of dynamic information and ages together with the element abundances of the main catalogue in Section 8. We focus on Galactic Archaeology on a global scale and the chemodynamical evolution of our Galaxy. Along with the main and value-added-catalogues of this release, we publish the observed optical spectra for each of the arms of HERMES on the DataCentral³ and provide the scripts used for the analysis as well as post-processing online in an open-source repository⁴ GALAH+ DR3 was timed to allow the scientific community to directly use abundances together with the latest *Gaia* eDR3 information. We have not yet incorporated the latter into our abundance analysis, but plan to do so in future data releases, as we outline in Section 9. In this section, we conclude and give an outlook to future observations as part of the ongoing observations of the GALAH survey (called phase 2 with an adjusted target selection) and our next data release.

2 TARGET SELECTION, OBSERVATION, REDUCTION

While our previous data release (Buder et al. 2018) contained only stars from the main GALAH survey, the current catalogue combines data from multiple projects with different science goals, all conducted with the HERMES spectrograph (Sheinis et al. 2015) and the 2dF fibre positioning system (Lewis et al. 2002) at the 3.9-metre Anglo-Australian Telescope. All the spectra have therefore been processed through the same data reduction pipeline. The collection into a single catalogue, which includes the K2-HERMES (S. Sharma et al., in preparation) and TESS-HERMES (S. Sharma et al., in preparation) surveys, was chosen for ease of use. Full details of these additional surveys are presented in their corresponding data release papers and users are advised to refer to those when using data from these surveys. The column `survey_name` in the catalogue denotes the survey each star belongs to. Data from four main projects, plus a number of smaller observing programmes, are included in GALAH+ DR3. Fig. 1 shows their on-sky distribution. The majority of the stars are nearby, with a median distance of 826 pc (see Fig. 2a), and cover a large variety of stellar types and evolutionary stages, as can be seen in the colour–magnitude diagrams both with *Gaia* (Fig. 2b) and 2MASS (Fig. 2c) bandpasses. Below, we describe the target selection for each of the four main projects.

2.1 Target selection

The GALAH input catalogue was made by combining the 2MASS (Skrutskie et al. 2006) catalogue of infrared photometry with the UCAC4 (Zacharias et al. 2013) proper motion catalogue. We only included stars with reliable 2MASS data, as captured in their data quality flags ($Q='A'$, $B='1'$, $C='0'$, $X='0'$, $A='0'$, $prox_{\geq 6}$ arcsec). We also rejected any star that had a nearby bright neighbour, with a rejection radius dependent on the bright star's V magnitude, such that the potential target is rejected if the bright star is closer than $(130 - [10 \times V])$ arcsec. The APASS photometric

³<https://docs.datacentral.org.au/galah/>

⁴http://github.com/svenbuder/GALAH_DR3

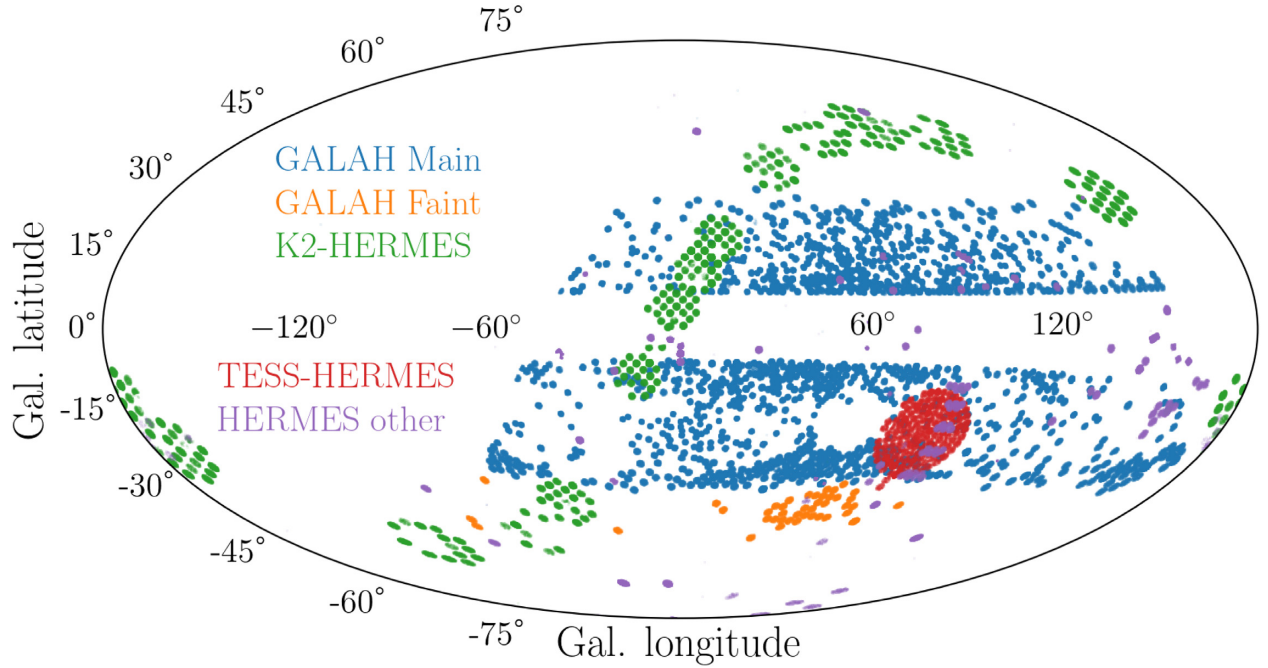


Figure 1. Overview of the distribution of stars included in this data release in Galactic coordinates with the centre of the Galaxy at the origin. Shown are the GALAH main (blue) and faint (orange) targets, which avoid the Galactic plane. The targets of the K2-HERMES follow-up (green) fall within with the K2 campaigns along the ecliptic and show the characteristic tile-pattern of the *Kepler* telescope. The TESS-HERMES observations (red) are focused on the TESS Southern Continuous Viewing Zone. Other HERMES targets (purple) are distributed across the sky and were observed during independent programmes.

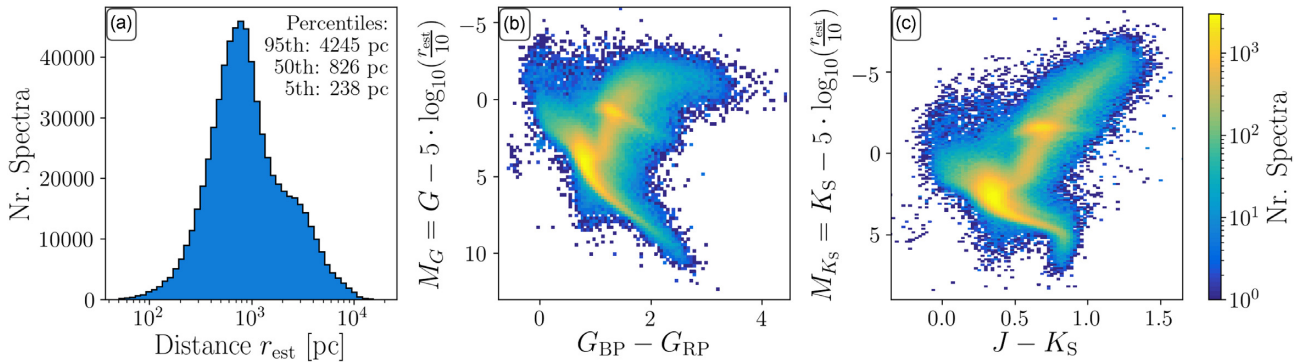


Figure 2. Overview of distances and photometric information corresponding to the spectra (including repeats for some stars) observed as part of GALAH+ DR3 up to 2019 February 25. Panel (a) shows the Bailer-Jones et al. (2018) distances of stars in GALAH+ DR3. Due to the magnitude limited selection of stars, the majority of stars are not only dwarfs but also nearby; that is, within 1 kpc. Only 5.8 per cent of stars are beyond 4 kpc. Panel (b) shows a colour–absolute magnitude diagram in the optical *Gaia* passbands. Panel (c) shows an analogous diagram made with the infrared 2MASS passbands.

catalogue (Henden et al. 2012) was not complete in the Southern sky at the start of GALAH observations in 2013, so we use a synthetic V_{JK} magnitude calculated from 2MASS photometry: $V_{JK} = K + 2(J - K + 0.14) + 0.382e^{(J - K - 0.2)/0.5}$. Sharma et al. (2018) demonstrate by using PARSEC isochrones (Marigo et al. 2017) that this is a reasonable approximation for the V magnitude for the types of stars observed in GALAH.

Four main projects are included in the GALAH+ DR3 catalogue (GALAH-main, GALAH-faint, K2-HERMES, and TESS-HERMES), each of which has its own selection function. We have attributed each possible pointing of the major sub-surveys to a specific `field_id`, as listed in Table 1. The main GALAH survey takes as potential targets all stars with $12.0 < V_{JK} < 14.0$, $\delta < +10^\circ$ and $|b| > 10^\circ$ in regions of the sky that have at least 400 targets in π square degrees (the 2dF field of view). We then segment this data

Table 1. Field selection (`field_id`) for the programmes included in this data release. Note the gaps between different TESS-HERMES fields are caused by other HERMES programmes in between them.

Programme	field_id	Nr. Spectra	survey_name
GALAH Main	0..6545	462045	galah_main
GALAH Faint	6831...7116	14818	galah_faint
K2-HERMES	6546...6830	112943	k2_hermes
TESS-HERMES	7117...7338	34263	tess_hermes
	7358...7365	–	–
	7426...7431	–	–
HERMES other	other	54354	other
Total	–	678423	–

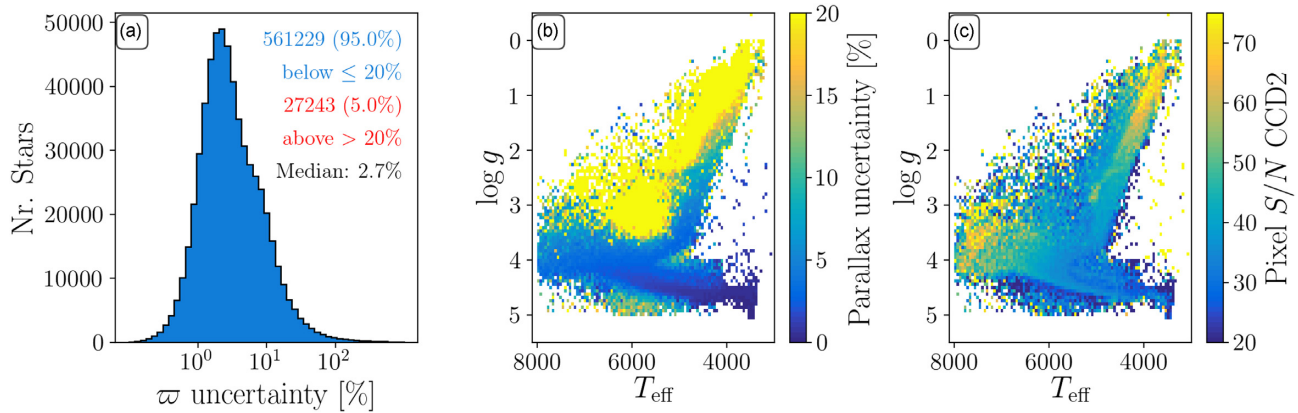


Figure 3. Overview and distribution of parallax uncertainty and S/N for different types of stars (not spectra as in Fig. 2). Panel (a) Parallax (ϖ) uncertainty provided by *Gaia* DR2. We note that the median uncertainty has decreased from 2.7 per cent to 1.5 per cent between *Gaia* DR2 and *Gaia* eDR3. 561 229 (95 per cent) stars sit below 20 per cent in fractional uncertainty, and 27 243 (5 per cent) stars fall above 20 per cent. Panel (b) Distribution of *Gaia* DR2 fractional parallax uncertainty across the stellar parameters T_{eff} and $\log g$ derived by GALAH+ DR3. Local cool dwarfs have the most reliable parallax information, while giants, and especially luminous giants have the worst. Panel (c) Distribution of S/N per pixel for the green channel (CCD2) across the stellar parameters T_{eff} and $\log g$. Hot dwarfs (brighter than cool stars in the green channel) and luminous giants (brightest within the magnitude limited cohort) have the highest S/N in the green channel. The S/N for hot stars is typically better in the blue and green CCDs (relative to cool stars), whereas it is higher in the red and IR CCDs for the cool stars (relative to hot stars).

set into 6546 ‘fields’ with a fixed centre and radius between 0.7° and 1° . Fields containing more than 400 stars are observed multiple times with separate target lists. The GALAH-faint programme was aimed at extending survey observations to regions with low target density. The target selection was shifted to $12 < V_{\text{JK}} < 14.3$ as a way to maintain at least 400 stars per field. The GALAH survey also includes a few other extensions. The GALAH-bright programme targets bright stars ($9.0 < V_{\text{JK}} < 12.0$) to be observed in twilight or poor observing conditions. For bright stars, we use the same field centres as in regular survey observing, and require at least 200 stars per field. The GALAH-ultrafaint programme targets very faint stars $14 < V_{\text{JK}} < 16$. This was aimed at extending the survey into regions further away from the Sun. These fields were only observed under dark conditions.

The K2-HERMES survey leverages the excellent match between the two degree diameter of the 2dF fibre positioner and the five square degrees covered by each detector in the *Kepler* spacecraft to create an efficiently observed spectroscopic complement for red giants in the K2 campaign fields. The K2-HERMES programme has both ‘bright’ ($10 < V_{\text{JK}} < 13$) and ‘faint’ ($13 < V_{\text{JK}} < 15$, $J - K_s > 0.5$) target cohorts, to complement the asteroseismic targets that are the focus of the K2 Galactic Archaeology Program (Stello et al. 2015, 2017). Analysis of asteroseismic and spectroscopic data together is key for GALAH+ DR3, and enables in-depth exploration of the structure and history of the Milky Way (e.g. Sharma et al. 2016, 2019). The spectroscopic data also provide essential insights for the planet hosting stars identified in K2 data (Wittenmyer et al. 2018, 2020).

The TESS-HERMES survey collected spectra for stars in the range $10.0 < V_{\text{JK}} < 13.1$ in the TESS Southern Continuous Viewing Zone, within 12° of the Southern ecliptic pole. TESS-HERMES aimed to provide accurate stellar parameters for candidate TESS input catalogue stars (Stassun et al. 2019), to better focus TESS target selection on the most promising asteroseismic targets. The results of the TESS-HERMES project are publicly available, and the project and outputs are described in Sharma et al. (2018). 54 354 in the ‘HERMES other’ programme are from targeted observations of stars

in open clusters, the GALAH Pilot Survey (Martell et al. 2017), or targets from other HERMES observing that were not part of any of these surveys.

Since GALAH observes stars mainly nearby stars (81.2 per cent of the sample is within 2 kpc, as shown in Fig. 2), almost all GALAH targets have well measured 5D (99 per cent) or even 6D (45 per cent) information from *Gaia* (Gaia Collaboration 2018; Lindegren et al. 2018). An overview of the astrometric and spectroscopic quality for the observed stars can be found in Fig. 3(a). The median fractional parallax error for GALAH stars is 2.7 per cent, and 95 per cent (561 229) of GALAH stars have parallax errors below 20 per cent (see panel a). A total of 588 571 of our observations are of stars with matched *Gaia* parallax measurements. When dividing the sample into giants ($T_{\text{eff}} < 5500$ K and $M_{K_s} < 2$ mag) and dwarfs ($T_{\text{eff}} \geq 5500$ K or $M_{K_s} \geq 2$ mag), 96 per cent (369 227/383 088) of the observed dwarf stars have parallax uncertainties below 10 per cent and 70 per cent (140 840/200 927) of the observed giant stars have parallax uncertainties below 10 per cent. The inferred distance estimates from Bailer-Jones et al. (2018), used for the spectroscopic analysis in this release, are crucial for the small fraction of GALAH+ DR3 stars with parallax uncertainties above 20 per cent.

Additionally, the available asteroseismic information is growing steadily as the analysis of data from the K2 campaigns progresses. The overlap between GALAH targets and K2 targets from campaign C1-C8 and C10-C18 has increased to more than 10 000 stars with measured asteroseismic v_{max} values (Zinn et al. 2020) and spectroscopic information, and covers almost the entire red giant branch ($\log g \sim 1.5-3.0$ dex) and helium-core burning red clump.

The magnitude limited selection of the GALAH survey (see the magnitude distribution in Fig. 4a) causes a strong correlation between increasing distance (and decreasing parallax quality) with increasing luminosity. This tradeoff between luminosity and parallax uncertainty was also visible for the stars in common between *Gaia* DR1 and GALAH DR2 (Buder et al. 2019) and is still present with the use of *Gaia* DR2, as we illustrate in Kiel diagrams in Fig. 3(b), showing that especially giants with larger distances suffer from large parallax uncertainties.

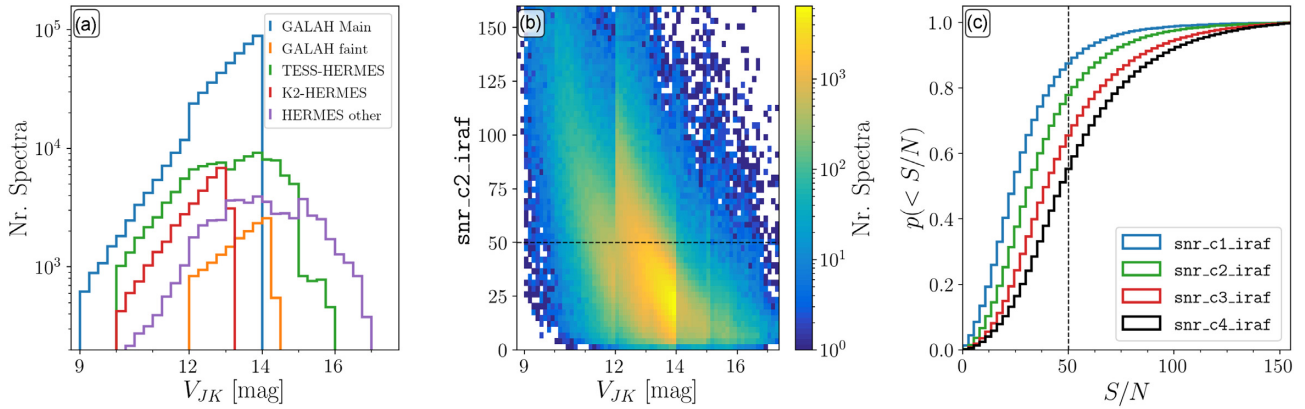


Figure 4. Distributions of magnitudes and S/N of GALAH+ DR3. Panel (a) Distribution of V magnitude calculated from 2MASS J and K_s . Panel (b) Distribution of average achieved S/N per pixel for the green band (CCD 2) as a function of V_{JK} . Panel (c) Cumulative distribution of the S/N per pixel of the different bands/CCDs of HERMES for GALAH+ DR3. A black, dashed line indicates the overall S/N of 50 that we initially aimed for for CCD2.

2.2 Observations

GALAH data are acquired with the 3.9-metre Anglo-Australian Telescope at Siding Spring Observatory. Up to 392 stars can be observed simultaneously using the 2dF robotic fibre positioner (Lewis et al. 2002) that sits at the telescope’s prime focus. The fibres run to the High Efficiency and Resolution Multi-Element Spectrograph (HERMES; De Silva et al. 2015; Sheinis et al. 2015), where the light is dispersed at $R \sim 28000$ and captured by four independent cameras. HERMES records $\sim 1000 \text{ \AA}$ of the optical spectrum across its four non-contiguous channels (4713–4903, 5648–5873, 6478–6737, and 7585–7887 \AA). Details of the instrument design and as-built performance of HERMES can be found in Barden et al. (2010), Brzeski, Case & Gers (2011), Heijmans et al. (2012), Farrell et al. (2014), and Sheinis et al. (2015).

Since HERMES was first commissioned, raw data it obtains has been contaminated by odd saturated points with vertical streaking, which was traced back to the choice of glass for the field flattening lens inside each of the four cameras (Martell et al. 2017). The original glass had been chosen for its high index of refraction, but uranium in the glass emitted α particles that caused the saturated points and vertical readout streaks when they were captured by the HERMES CCDs (Edgar et al. 2018). In the first half of 2018, the original field flattening lenses were replaced with lenses made from a less radioactive glass, and the vertical streaks have almost stopped occurring in the data. The point spread function in the HERMES cameras changed as a result of changing the field flattening lenses, and is now larger and less symmetric in the corners of the detectors. As part of HERMES recommissioning, the GALAH team fed light from a Fabry–Perot interferometer into HERMES to characterize the new PSF across each detector, and this information has been incorporated into the data reduction procedure.

The observing procedure and targeting strategy for this data release are the same as for previous public GALAH data, including the selection of fields via the GALAH-internal OBSMANAGER (keeping track of already observed fields and suggesting fields with lowest airmass at a given observing time for a given programme) and the assignment of targets on to 2dF fibres via CONFIGURE (Miszalski et al. 2006). For further information on the strategy of GALAH Phase 1, with the GALAH main and faint observations, we refer the reader to Buder et al. (2018). For the K2-HERMES observing strategy, the reader is referred to Wittenmyer et al. (2018) and Sharma et al. (2019), and for TESS-HERMES to Sharma et al. (2018).

GALAH+ DR3 expands the number of targets from DR2 significantly and includes all data taken between 2013 November and 2019 February. The distribution of GALAH+ DR3 stars across V_{JK} and signal-to-noise ratio (S/N) is shown in Fig. 4(b) and adds another perspective on the complex correlation of luminosity (or surface gravity $\log g$) with S/N for the observed stars, as shown in Fig. 3(c).

GALAH, K2-HERMES, and TESS-HERMES observers choose from a data base of available fields depending on conditions, limiting the hour angle to within ± 2 h whenever possible. The standard observing procedure for regular GALAH survey fields is to take three 1200 s exposures, with an arc lamp and flat lamp exposure taken at the same sky position as each field to enable proper extraction and calibration of the data. Bright-star fields are observed in evening and morning twilight, and when the seeing is too poor for the regular survey fields. They receive three 360 s exposures and the same calibration frames as for the regular fields.

The median seeing at the AAT is $1''.5$, and the exposure time is extended by 33 per cent if the seeing is between $2''.0$ and $2''.5$ and by 100 per cent if the seeing is between $2''.5$ and $3''.0$. This exposure time was chosen to achieve an S/N of 50 per pixel (equivalent to 100 per resolution element) in the HERMES green channel (CCD 2). This is accomplished in nominal seeing when a star has an apparent magnitude of 14 in the photometric band matched to the camera ($B = 14$ and CCD 1, $V = 14$ and CCD 2, etc.) Mismatches between predicted and actual data quality are mainly caused by a combination of seeing, cloud, and airmass. We show the distribution for the actual S/N per pixel as a cumulative distribution for all four HERMES channels in V_{JK} in Fig. 4(c). Depending on the spectral type, the S/N achieved for a given star in each CCD varies (i.e. a hot star will be brighter in the blue and green passbands and fainter in the red and infrared passbands).

2.3 Reductions

Since the release of GALAH DR2, we have improved our reduction pipeline (Kos et al. 2017), and as a result, all spectra included in DR3 have been reduced using the new, improved pipeline. As in GALAH DR2, raw images are corrected for bias level and flat-field, and cosmic rays are removed with a modified LaCosmic algorithm (van Dokkum 2001). Scattered light and fibre cross-talk signals are removed. The wavelength solution for the extracted spectra is found via fitting of ThXe arc lamp observations. Sky spectra are modelled from the 25 sky fibres included in each field and subtracted, and

synthetic telluric lines are computed using `MOLECFIT` (Kausch et al. 2015; Smette et al. 2015) and removed from observed spectra. The reduction pipeline runs a cross-correlation with `AMBRE` spectra (De Laverny et al. 2012) to provide a first estimate of the stellar parameters effective temperature T_{eff} , surface gravity $\log g$, iron abundance $[\text{Fe}/\text{H}]$, as well as radial velocity v_{rad} , and to normalize the spectra.

The main improvement is the wavelength solution, which is now more stable at the edges of the green and red CCDs, where we lack arc lines. This has been achieved by monitoring the solution and fixing the polynomial describing the pixel-to-wavelength transformation, if deviations from a typical or average solution are detected. The solution is described by a 4th order Chebyshev polynomial. We use IRAF's `IDENTIFY` function to find the positions of arc lines in each image and match them with our linelist. Fitting the solution, however, is now done in a more elaborate way. Initially, all spectra from the same image are allowed to have an independent solution. Then the four coefficients of the Chebyshev polynomial are compared. The first coefficient defines the zero-point. Because the 2dF fibres are not arranged monotonically in the pseudo-slit, the first coefficient is truly independent of the spectrum number (spectra being numbered 1 to 400 in each image). The values of the other three coefficients should be a smooth function of the spectrum number. If a coefficient for a specific spectrum deviates by more than 3σ from a smooth function, it is corrected to lie on the smooth function. This successfully fixes the previous problems with incorrect wavelength solutions at the edge of the image.

Our improved reduction pipeline also features an improved parametrization of cross-talk. It can only be measured in larger gaps between every 10th spectrum. Cross-talk was previously represented as a function of the position in the image, but now each batch of 10 spectra (from one slitlet) is assigned the measured cross-talk without any interpolation. The cross-talk is still a function of the direction along the dispersion axis. The normalization has been improved with a new identification of continuum sections (regions of a spectrum where the continuum is measured) and optimized polynomial orders. The pipeline has been actively maintained and adapted to perform well with the recommissioned instrument following the replacement of the field flattening lenses in 2018 May. Other minor improvements and computing optimizations were made.

As we lay out in the next section, with the analysis approach via spectrum synthesis chosen for GALAH+ DR3, we will not make use of the full spectra of GALAH, but restrict ourselves to absorption features with reliable line information for spectrum synthesis, when estimating stellar parameters and abundances.

3 DATA ANALYSIS

In this section, we describe how the outputs from the data reduction process are used to estimate the final stellar parameters for each spectrum as well as up to 30 element abundances. The starting points for the analysis are the products of the reduction pipeline, described in Section 2.3, that is reduced spectra, initial estimates of radial velocity v_{rad} , as well as initial estimates of the stellar parameters T_{eff} , $\log g$, and $[\text{Fe}/\text{H}]$. Contrary to GALAH DR2, we do not use the reduction-pipeline based, v_{rad} -shifted, normalized spectra for the spectrum analysis of this release.

3.1 Changes from GALAH DR2 to GALAH+ DR3

The two most important differences to the workflow of our analysis are the following: First, we are using astrometric information from the *Gaia* mission to break spectroscopic degeneracies. Secondly,

we do not use data-driven approaches for the spectrum analysis in GALAH+ DR3, but only the spectrum synthesis code `Spectroscopy Made Easy` (Valenti & Piskunov 1996; Piskunov & Valenti 2017, hereafter SME), which had only been used for the training set analysis in DR2. We visualize the reasons for this step with the comparison of GALAH DR2 and DR3 in Fig. 5. We found in DR2 that stars at the periphery in stellar label space, e.g. high temperature (compare panels a and d) or low metallicity (compare panels b and e) did not receive optimal labels from the data-driven process.

Data-driven models that also use astrometric information may likely perform equally well as, or possibly better than, our DR3 analysis for many aspects. In DR3, we chose to apply the more traditional method to the full sample to assess the limitations of the data-driven approach. This includes testing the flexibility of the model we used, as we found that quadratic models (as used for GALAH DR2) are too inflexible to be applicable across the entire stellar parameter space. Training by using χ^2 -optimization may give too much weight to outliers. Furthermore, we want the results to be independent of the exact selection criteria used to define the training set, since data-driven models can struggle to inter- and extrapolate for spectra which are not sufficiently represented and modelled in the training step. Limited by the scope of the training set, we had to flag several abundance measurements for a vast majority of elements, where we suspected extrapolation. The flagged results are shown as the lighter blue background in Fig. 5, where we find in panel (a) that some of the inferred stellar parameters are unphysical, such as the upturn in the low-mass main sequence and the correlation between T_{eff} and $\log g$ for hot stars. The effect of flagging on the number of inferred stellar abundances can best be seen in the drastic increase in Li detections in DR3 (compare panels c and f), where detections in DR2 were limited to warm dwarfs and Li-rich giants. This was a direct result of the choice of training set stars, with the numbers of detections in DR2 being further lowered by our use of more conservative criteria of detections for lines.

Being able to estimate reliable stellar parameters for hot stars (see panel d) has also enabled the determination of several of their abundance patterns, which was not possible in DR2. Intriguingly, some of the A- and F-type main sequence stars exhibit underabundant $[\alpha/\text{Fe}]$ (see lowest measurements in panel e) and overabundant iron-peak and neutron-capture elements, which is the peculiar chemical compositions of Am/Fm stars (see e.g. Xiang et al. 2020). In DR3, we are also able to estimate more accurate element abundances for metal-poor stars ($[\text{Fe}/\text{H}] < -1$ dex), in particular those with the previously identified low- α^5 ‘outer’ halo pattern (see e.g. Nissen & Schuster 2010).

For this data release, we run the analysis pipeline only for spectra that have initial radial velocity estimates either as part of previous unflagged GALAH data releases, unflagged measurements from the DR3 reduction pipeline, or from Gaussian fits to the Balmer lines with less than 5 km s^{-1} uncertainty. We therefore excluded 81 007 spectra⁶. Further we restrict this release to stars with external information on parallaxes from *Gaia* (Lindgren et al. 2018), thus excluding 9080 spectra. For a few tens of bright stars that are not in *Gaia* DR2, we take distances and parallaxes from *Hipparcos* (van Leeuwen 2007), which can be identified via missing extended astrometric information.

⁵These stars have lower abundances in the α -elements at fixed $[\text{Fe}/\text{H}]$ when compared to the high- α disc population.

⁶We note that these observations include spectra with low S/N as well as a few calibration observations like sky or dome flats falsely labelled as stellar observations over the course of 5 yr of observations.

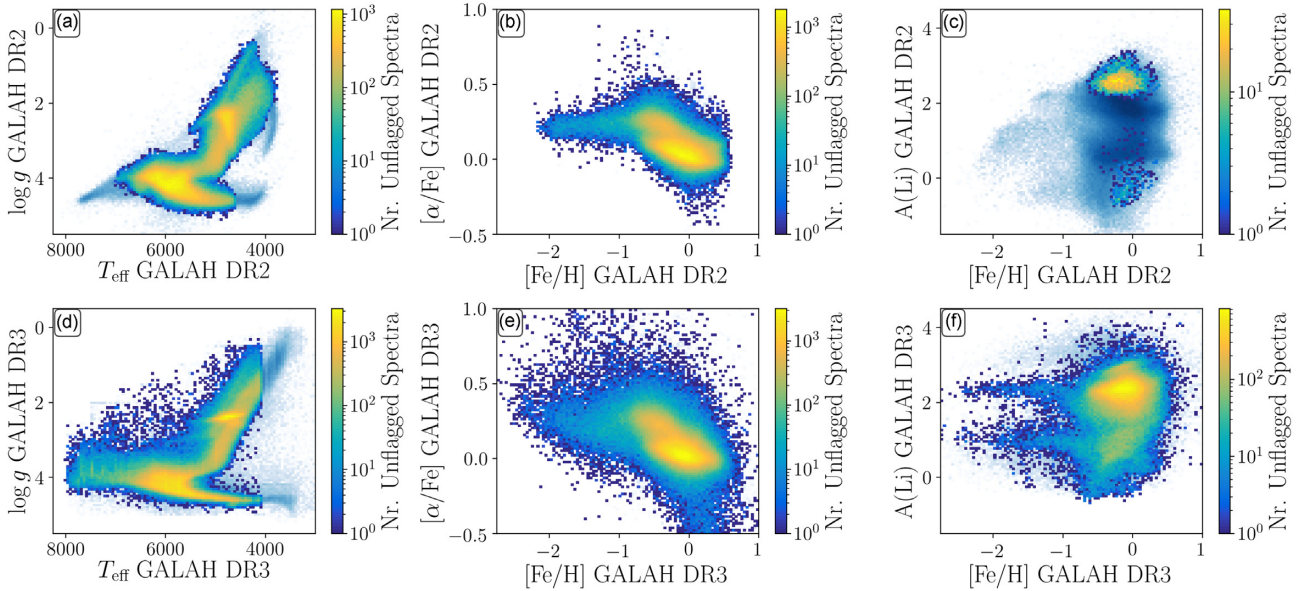


Figure 5. Comparison of GALAH DR2 (upper panels) and GALAH+ DR3 (lower panels, this release). The light-blue background indicates all measurements, whereas the colourmap shows the number of successful (unflagged) measurements at each point. Left-hand panels: Kiel diagrams, i.e. T_{eff} versus $\log g$, for stars of DR2 (a) and DR3 (d). Middle panels: Abundance pattern of iron versus α -process elements, i.e. Tinsley–Wallerstein diagrams displaying $[\text{Fe}/\text{H}]$ versus $[\alpha/\text{Fe}]$, for DR2 (b) and DR3 (e). Right-hand panels: Absolute Li abundance as a function of iron abundance, i.e. $[\text{Fe}/\text{H}]$ versus $A(\text{Li})$, for DR2 (c) and DR3 (f). The stellar parameters and abundances from GALAH DR2 appear more tightly constrained, but we note that this is an artefact of the data-driven approach, which tends to find solutions closer to the mean parameter/abundance patterns. We include all DR2 and DR3 stars in these panels, and not just the stars common to both to highlight the increase in observations, accuracy of stellar parameters, and coverage of abundances, rather than the improvement in precision for the same spectra.

3.2 The general workflow

Our general workflow follows the same approach as the spectrum synthesis analysis for DR2, with the aim to homogeneously and automatically analyse a large number of spectra that intrinsically look very different. The analysis is divided into two fundamental steps: first, we estimate the stellar parameters; and secondly, we keep the stellar parameters fixed while only fitting one abundance at a time for the different lines/elements in the GALAH wavelength range. For the stellar parameter estimation (first step), we first perform a normalization and a first rough stellar parameter fit with one iteration, followed by a final normalization and finer parameter fit that is iterated on until convergence. For this, we limit ourselves to 46 selected segments of the GALAH spectra which include the lines with reliable line data for the stellar parameter analysis, as described in detail in Section 3.3. For the abundance analysis (second step), we perform only one normalization and iteratively optimize the abundance based on those data points of the lines/elements that we estimate to be unblended enough after comparing a synthetic spectrum with all lines with another one that only has the lines of the element in question. To achieve most accurate results, our analysis is based on the most recent line data, atmosphere grids, and grids to compute departures from the common LTE assumption during the line formation, as described in detail in Section 3.3. Below we describe this workflow in more detail, which illustrates the challenges of homogeneously analysing very different spectra:

(i) Initialize SME (version 536) with choices of line data, atmosphere grid, non-LTE departure grids, observed spectrum (limited to the 46 segments⁷ used for the parameter estimation) including

selection of continuum and line masks, initial parameters for χ^2 optimization. Check if all external information is provided and then update the initial $\log g$ with this external information and the initial stellar parameters as outlined in the explanation of $\log g$ (Section 3.3).

(ii) Normalize all 46 segments individually with the chosen initial setup by fitting linear functions first to the observed spectrum (iteratively and with sigma-clipping) and then to the difference of the observed and synthetic spectrum.

(iii) Optimize the stellar parameters T_{eff} , $[\text{Fe}/\text{H}]$, v_{broad} ($v_{\text{sin } i}$ with v_{mac} set to 0⁸), and global v_{rad} with 2 major SME update loops (calculating double-sided partial derivatives and exploring the local χ^2 surface with up to 5 different parameter choices). Consistently update $\log g$ and v_{mic} from physical and empirical relations, respectively, with every change of T_{eff} or $[\text{Fe}/\text{H}]$. In our test, this already led to updated parameters close to the χ^2 global minima.

(iv) Normalize all 46 segments again individually as in step 2, but with updated stellar parameters.

(v) Optimize the stellar parameters T_{eff} , $[\text{Fe}/\text{H}]$, v_{broad} , and v_{rad} with up to 20 major SME update loops as in step 3 until the fractional change of χ^2 is below 0.001.

(vi) Collect stellar parameters for validation. Save covariance uncertainties, based on the statistical χ^2 uncertainties given the uncertainties of the normalized flux, in addition to the uncertainties delivered by SME (see Piskunov & Valenti 2017, for more details). The validation of stellar parameters (see Section 4) led to an

⁷These can be found in our online documentation.

⁸At the resolution of GALAH, $v_{\text{sin } i}$ and v_{mac} are degenerate broadening influences. We thus fit them with SME by setting v_{mac} to 0 and only fit $v_{\text{sin } i}$.

adjustment of the estimated atmospheric [Fe/H] (SME.feh) by adding 0.1 dex.⁹

(vii) Initialize SME for the element abundance estimation with choices of line data, atmosphere grid, non-LTE departure grids, observed spectrum (limited to line segment(s) used for the element abundance estimation) including selection of continuum and line masks, final global atmosphere parameters for χ^2 optimization. Contrary to steps 3 and 5, hereafter the aforementioned global parameters, including v_{rad} , are kept fixed.¹⁰

(viii) Normalize the segment(s) for the particular line (for the line-by-line analyses, e.g. Sr6550) or for all lines of the particular chemical species (e.g. Ca) with the chosen initial setup by fitting linear functions first to the observed spectrum. Improve this normalization by fitting a linear function to the difference between the observed and synthetic spectrum to create a ‘full’ synthetic spectrum.

(ix) Because the same line exhibits different degrees of blending in different stars, which are complex and difficult to predict ab-initio, perform a blending test by creating a ‘clean’ synthetic spectrum only based on the lines of the element to be fitted. Then compare the ‘full’ and ‘clean’ spectra for elements other than Fe for the chosen line mask pixels and neglect those which deviate more than $\Delta\chi^2 > 0.005$.

(x) Optimize the relevant element abundance entry in the abundance table (SME.abund) with up to 20 major SME update loops until fractional change of χ^2 is below 0.001. The atmosphere is updated with each change of chemical composition to stay consistent, but we note that for the sake of computation cost with SME, the abundances, that are not fitted, are kept at scaled-solar, with the exception of Li with $A(\text{Li}) = 2.3$, an enhancement of 0.4 dex for N in giants, and the pre-computed α -enhancement for α -process elements.

(xi) Collect stellar parameters and element abundances for validation and post-processing.

(xii) Calculate upper limits for each element/line for non-detections by estimating the lowest abundance that would lead to a line flux depression of 0.03 below the normalized continuum (see more detailed explanations at the end of this section).

(xiii) Post-processing: apply flagging algorithms, calculate final uncertainties from accuracy and precision estimates, combine line-by-line measurements of element abundances weighted by their uncertainties.

For each star, the computational costs amount to between 50 CPU minutes (for the hottest stars with few lines), 2 CPU hours for the Sun, up to 6 CPU hours (for the coolest stars with most lines), with around 30–50 per cent of that used for the stellar parameter step and the rest for abundance estimation for all lines. The total computational costs amount to 1.2 Mio CPU hours for the stellar parameter and abundance fitting, that is, neglecting data collection and post-processing.

3.3 Details of the spectroscopic analysis

The line data are based on the corresponding compilation for the *Gaia*–ESO survey (Heiter et al. 2015a; Heiter 2020, Heiter et al. 2021) with updated oscillator strengths ($\log gf$ values) for some

elements, in particular VI (Lawler et al. 2014), CrI (Lawler et al. 2017), Co I (Lawler, Sneden & Cowan 2015), Ni I (Wood et al. 2014) and Y II (Palmeri et al. 2017). In addition, we ‘astrophysically’ tuned (based on solar abundances and observations) the $\log gf$ values for approximately 100 lines that were not used for abundance measurements, but affected the continuum placement and blending fraction for the main diagnostic lines. The final compilation of the lines used for stellar parameter and element abundance estimation together with the most important line data are listed in Table A1.

The 46 segments and masks for stellar parameter estimation are based on selected neutral and ionized Sc, Ti, and Fe lines as well as the two Balmer lines H_α and H_β . We chose these lines based on the high quality of their experimental or theoretical line data and limit ourselves to the least blended lines or parts of lines. The masks used for parameter and abundance optimization were selected based on the line shapes of several thousand randomly selected spectra (including those of crowded spectra of cool stars with dominant molecular absorption bands). The masks used for continuum placement were selected on-the-fly as the regions with smallest amount of line absorption, ensuring a sufficient number of (pseudo-)continuum points on either side of the line mask.

The model atmospheres used for our analysis are theoretical 1D hydrostatic models taken from the MARCS grid (Gustafsson et al. 2008; MARCS2014). The adopted grid is the same as in GALAH DR2 (Buder et al. 2018; Section 3.2). In brief, they cover $2500 \leq T_{\text{eff}} \leq 8000$ K, $-0.5 \leq \log g \leq 5.5$ dex with the exclusion of the hottest and lowest surface gravity regions, $-5 \leq [\text{Fe}/\text{H}] \leq 1$, and were computed with the Solar chemical composition of Grevesse, Asplund & Sauval (2007), scaled by [Fe/H] and with α -enhancements as laid out later in this section. Plane-parallel models were adopted for $\log g \geq 4$, and spherically symmetric models for $\log g < 4$.

The non-LTE grids of departure coefficients that we use for the on-the-fly synthesis of 1D non-LTE spectra are described in Amarsi et al. (2020). In brief, new grids of departure coefficients were constructed by adopting the non-LTE model atoms presented for H (Amarsi et al. 2018a), Li (Lind, Asplund & Barklem 2009; Wang et al. 2021), C (Amarsi et al. 2019), O (Amarsi et al. 2018b), Na (Lind et al. 2011), Mg (Osorio et al. 2015), Al (Nordlander & Lind 2017), Si (Amarsi & Asplund 2017), K (Reggiani et al. 2019), Ca (Osorio et al. 2019), Mn (Bergemann et al. 2019), and Ba (Gallagher et al. 2020), and running on the MARCS model atmosphere grid using the non-LTE radiative transfer code BALDER (Amarsi et al. 2018a), a modified version of MULTI3D (Leenaarts & Carlsson 2009). For Fe, the same non-LTE grids of departure coefficients that were used in GALAH DR2 were adopted here (Amarsi et al. 2016; Lind et al. 2017). As we demonstrated in Amarsi et al. (2020), relaxing LTE reduces the dispersion in the [X/Fe] versus [Fe/H] plane significantly, for example by 0.1 dex for Mg and Si, and it can remove spurious differences between the dwarfs and giants by up to 0.2 dex. Recent progress in this field will allow the implementation of non-LTE also for other large surveys (Amarsi et al. 2020; Osorio et al. 2020). The use of non-LTE grids is unique to GALAH, whereas most other current major surveys, like APOGEE (Jönsson et al. 2020), RAVE (Steinmetz et al. 2020a), and *Gaia*–ESO (Smiljanic et al. 2014) report 1D LTE results in their public data releases.

Initial stellar parameters and abundances are chosen depending on the quality of reduction products and their availability in GALAH DR2 (Buder et al. 2018). If the stellar parameters of GALAH DR2 (and non-published spectra of K2-HERMES, TESS-HERMES, and other spectra analysed in the same way via *The Cannon*) are not flagged, we use those. Otherwise, we use initial rough stellar parameters provided as part of the reduction pipeline

⁹This is not the final [Fe/H] = FE.H as reported in this data release, but a pseudo iron abundance SME.feh = FE.H_ATMO, estimated from H, Sc, Ti, and Fe lines.

¹⁰For the Li line, at the end of CCD3, we have found that for roughly 10 per cent of the spectra, the wavelength solution is not reliable enough and therefore simultaneously fitted [Li/Fe] and v_{rad} .

during its radial velocity estimation with grid interpolation, if they are unflagged. Otherwise we use a set of fiducial stellar parameters ($T_{\text{eff}} = 5500$ K, $\log g = 3.0$ K, and $[\text{Fe}/\text{H}] = -0.5$ dex as well as the result of Gaussian fits to the two Balmer lines for v_{rad}). We initialize the abundance pattern as scaled-solar, but adjust the alpha-enhancement as described later in this section.

Surface gravities are updated self-consistently with the other stellar parameters for each synthesis step via the fundamental relation of $\log g$, stellar mass \mathcal{M} , and bolometric luminosity L_{bol}

$$\log g = \log g_{\odot} + \log \frac{\mathcal{M}}{\mathcal{M}_{\odot}} + 4 \log \frac{T_{\text{eff}}}{T_{\text{eff},\odot}} - \log \frac{L_{\text{bol}}}{L_{\text{bol},\odot}} \quad (1)$$

Bolometric luminosities are estimated via

$$\log \frac{L_{\text{bol}}}{L_{\text{bol},\odot}} = -0.4 \cdot \left(K_S - 5 \cdot \log \frac{D_{\sigma}}{10} + BC(K_S) - A(K_S) - M_{\text{bol},\odot} \right) \quad (2)$$

from the 2MASS (Skrutskie et al. 2006) K_S band, a consistently calculated bolometric correction $BC(K_S)$ for this band using stellar parameters for each synthesis step, distances $D_{\sigma} = r_{\text{est}}$ from Bailer-Jones et al. (2018) as well as extinctions A_{K_S} in the K_S band. If both 2MASS H (Skrutskie et al. 2006) and WISE $W2$ (Cutri et al. 2014) band information have quality A (98 per cent of our sample) we used the RJCE method (Majewski, Zasowski & Nidever 2011) to compute $A_{K_S} = 0.917 \cdot (H - W2 - 0.08)$. For the remaining 2 per cent of our sample we used $A_{K_S} = 0.38 \cdot E(B - V)$ (Savage & Mathis 1979).

Bolometric corrections were estimated via interpolation of the grids from Casagrande & Vandenberg (2014, 2018). The interpolation needs stellar parameters and extinction and is performed whenever a stellar parameter is adjusted during its optimization step to ensure a self-consistent set of bolometric corrections and stellar parameters at any time. The upper limit of the extinction $E(B - V)$ for 95 per cent of our sample is below 0.48 mag based on the maps from Schlegel, Finkbeiner & Davis (1998), and to speed up calculations, we have therefore truncated the extinction input for the interpolation to this value.

Stellar masses are needed to estimate the surface gravities according to equation (1), but also depend on the surface gravity, luminosities, or absolute magnitudes, when estimated via isochrone interpolation. We therefore estimate those masses iteratively and self-consistently together with $\log g$ via isochrone interpolation whenever a stellar parameter $O_i \in [T_{\text{eff}}, \log g, [\text{Fe}/\text{H}], \text{and } L_{\text{bol}}]$ is updated during the parameter optimization. We assume that these parameters have Gaussian uncertainties and no covariances. This is a bold assumption, given that we use both $\log g$ and L_{bol} , which convey very similar information. However, we use large uncertainties for $\log g$, to limit its influence to extreme cases and can then write a likelihood for each isochrone point with model parameters S_i

$$\mathcal{L} \sim \prod_i \frac{1}{\sqrt{2\pi} \sigma_i} \cdot \exp \left(-\frac{(O_i - S_i)^2}{2\sigma_i^2} \right) \quad (3)$$

As we do not have final uncertainties for the stars at this stage of the analysis, we assume that the parameter uncertainties σ_i are 100 K, 0.5 dex, 0.2 dex, and $0.1 \cdot L_{\text{bol}}$ for T_{eff} , $\log g$, $[\text{Fe}/\text{H}]$, and L_{bol} , respectively. We want to stress that these are not the final average uncertainties, but that these values were chosen after extensive tests of ensuring enough isochrone points to be considered for the mass interpolation within the uncertainties. For the final uncertainties of this release, we use a more sophisticated implementation (see Section 4). We convert the iron abundances into a measurement of

metallicity Z by assuming the α enhancement to follow the stellar parameter relation laid out later in this section and combine this $[\alpha/\text{Fe}]$ and the atmospheric iron abundance to $[\text{M}/\text{H}]$ via the correlation by Salaris & Cassisi (2006) and into Z with the Solar value from the PARSEC+COLIBRI isochrones (Bressan et al. 2012; Marigo et al. 2017). We then use these PARSEC+COLIBRI isochrones on a grid with ages of $0.5 \dots (0.5) \dots 13.5$ Gyr and $[\text{Fe}/\text{H}] = -2.4 \dots (0.1) \dots 0.6$ dex to estimate maximum-likelihood masses on-the-fly.

Microturbulence velocities v_{mic} were computed consistently from the empirical relations estimated for the GALAH survey. For cool main sequence stars ($T_{\text{eff}} \leq 5500$ K and $\log g \geq 4.2$ dex) we use

$$v_{\text{mic}} = 1.1 + 1.6 \times 10^{-4} \cdot (T_{\text{eff}} - 5500 \text{ K}) \quad (4)$$

and for hotter or evolved stars ($T_{\text{eff}} \geq 5500$ K or $\log g \leq 4.2$ dex) we use

$$1.1 + 1.0 \times 10^{-4} \cdot (T_{\text{eff}} - 5500 \text{ K}) + 4 \times 10^{-7} \cdot (T_{\text{eff}} - 5500 \text{ K})^2, \quad (5)$$

where v_{mic} is given in km s^{-1} . In Section 6, we elaborate on the possible systematic trends that this simplified function could introduce.

Element abundances are computed during the analysis with the SME-internal notation of relative abundances for the first 99 elements, such that their sum amounts to 1. These are initialized consistently with the MARCS pattern from the Solar abundances of Grevesse et al. (2007). This notation is different from the usual $A(X) = A_{\text{X}} = \log \epsilon(X)$ and we thus convert them when reading out the final abundance pattern. In our final notations of element X, we report $A(X)$ on the customary astronomical scale for logarithmic abundances, where H is defined to be $A(H) = 12.00$, that is, $A(X) = \log \frac{N_X}{N_H} + 12$, where N_X and N_H are the number densities of elements X and H, respectively. We further report relative abundances as $[X/H] = A(X) - A(X)_{\odot}$ and $[X/\text{Fe}] = [X/H] - [\text{Fe}/\text{H}]$. For the explanation of our chosen values of $A(X)_{\odot}$ see Section 5.1 and for their values see Table A2. This table also lists the lines used for the line-by-line analysis, which were later combined for the final element abundances reported as X_{FE} for element X.

Line-by-line versus combined abundance analysis was selected based on the time and computation resources available. We have therefore measured only the following elements line-by-line (and report a value based on error-weighted means): α (see next paragraph), Li, C, K, Ti, V, Co, Ni, Cu, Zn, Rb, Sr, Y, Zr, Mo, Ru, La, Ce, Nd, Sm, Eu. To estimate the abundance of the following elements, we ran combined all lines of the particular elements to fit a global abundance at the same time: O, Na, Mg, Al, Si, Ca, Sc, Cr, Mn, Fe, Ba. We want to stress that the use of non-LTE grids does not affect the computation time. We chose to run several elements in a combined way because of the ongoing developments of their line selection or non-LTE grids. During the development of the pipeline we have tested all individual lines for the elements run with non-LTE and only selected those with similar trends and absolute abundances to run combined. By using individual lines, we are less prone to unreliable line data, such as unreliable $\log gf$ values. Incorrect oscillator strengths introduce a bias in the absolute abundance for each line. When the Solar abundance for these lines are however estimated independently from the others, they can still be used for the combined $[X/\text{Fe}]$ abundance, after applying individual Sun-based corrections to the absolute abundances (see Table A2).

Alpha-enhancement $[\alpha/\text{Fe}]$ is treated differently during the stellar parameter estimation step and the abundance determination step for each of the alpha-elements. In all cases, we initialize the abundances with the scaled-Solar pattern. We then adjust the alpha-enhancement for the elements O, Ne, Mg, Si, S, Ar, Ca, and Ti with the common

enhancement pattern of $[\alpha/\text{Fe}] = 0.4$ dex for $[\text{Fe}/\text{H}] \leq -1.0$ dex as well as $[\alpha/\text{Fe}] = 0.0$ dex for $[\text{Fe}/\text{H}] \geq 0.0$ dex and a linear function between both iron abundances. We update this value consistently whenever $[\text{Fe}/\text{H}]$ changes. For the individual lines of O, Mg, Si, Ca, and Ti as part of GALAH+ DR3, we then update their actual abundances while keeping the other abundances fixed. The final reported global $[\alpha/\text{Fe}] = \text{alpha_fe}$ is then an error-weighted combination of selected Mg, Si, Ca, and Ti lines (Mg5711, combined Si, combined Ca, Ti4758, Ti4759, Ti4782, Ti4802, Ti4820, and Ti5739). We stress however, that this combination is dependent on the detection of these lines and might come down to a single measurement, whereas other estimates are a combination of up to 9 measurements.

Upper limits are calculated for all measured lines/elements if no detection was possible. In this case, we estimate the smallest abundance needed to explain the strength of a line, that is the difference of line to continuum flux in the normalized spectrum of at least 0.03 or at least $1.5/(S/N)$ in the line mask. We interpolate these values from pre-computed estimates of line strengths for a set of stellar parameters and abundances. This approach was chosen and tested to estimate a larger number of upper limits for Li, but we want to caution the users to not blindly use them because we have not performed extensive tests for the other elements. They should only be used when essential for the science case and after thorough inspection of the observed and synthetic spectra.

4 VALIDATION OF STELLAR PARAMETERS

In this section, we describe the tests that we perform to validate the stellar parameters we obtain in terms of their accuracy (systematic uncertainties) and precision. In addition, we then describe several other algorithms that we have developed in order to identify peculiar stars or spectra – cases for which our standard pipeline might fail. The result of the performed quality tests are summarized in the stellar parameter flag `flag_sp` with flags that can be raised explained in Section 4.3. We do strongly recommend that all users take these flags into account, and make use of them unless the flags are explicitly not advisable for their particular science case. By default we recommend to use quantities with `flag_sp 0`, as this indicates that the stellar parameter estimates have passed all quality tests. Several influences on the accuracy, like unresolved binarity, as well as some possible systematics / caveats that we have not been able to quantify and therefore not flag, are addressed in Section 6.

To assess the quality of the stellar parameters we obtain, we resort to the commonly used comparison samples for accuracy, that is, the Sun (see our results for sky flat observations compared to literature in Table A3) and other *Gaia* FGK Benchmark stars (GBS; Jofré et al. 2014, 2015; Heiter et al. 2015b; Hawkins et al. 2016; Jofré et al. 2018), photometric temperatures from the Infrared Flux Method (IRFM; Casagrande et al. 2010), stars with asteroseismic information, and open as well as globular cluster stars. For the precision assessment, we use the internal uncertainty estimates and repeat observations of the same stars. We calculate the final stellar parameter errors for a given parameter P via

$$e_{\text{final}}^2(P) = e_{\text{accuracy}}^2(P) + e_{\text{precision}}^2(P). \quad (6)$$

The precision uncertainty $e_{\text{precision}}^2(P)$ is usually quantified by either fitting uncertainty $(e_{\text{fit}}^2(P))^{11}$ or uncertainty from repeated

¹¹In our case we use the square root of diagonal elements of the fitting covariance matrix to trace the fitting uncertainty (Piskunov & Valenti 2017).

Table 2. Accuracy values and expected precision at $S/N = \text{SNR}_{\text{C2_IRAF}} = 40$ per pixel for the stellar parameters. The stated precision value for $\log g$ is the mean precision of the whole sample.

Parameter (Unit)	Accuracy value	Precision ($S/N = 40$)
T_{eff} (K)	67	49
$\log g$ (cm s^{-2})	0.12	0.07
$[\text{Fe}/\text{H}]$ (dex)	0.034	0.055
$[\text{Fe}/\text{H}]_{\text{atmo}}$ (dex)	0.059	0.041
v_{broad} (km s^{-1})	2.0	0.83
v_{rad} (km s^{-1})	0.1	0.34

measurements ($e_{\text{repeats}}^2(P)$), which are typically expected to be of the same order. We compare and rescale these values to match in Section 4.2, so that we can use their maximum values for the individual measurements. Our repeat precision estimates are based on the behaviour with respect to our reference S/N , that is `snr_c2_iraf`, and lead to our applied uncertainty estimation of

$$e_{\text{final}}^2(P) = e_{\text{accuracy}}^2(P) + \max(e_{\text{fit}}^2(P), e_{\text{repeats}}^2(P, \text{snr}_{\text{C2_IRAF}})). \quad (7)$$

For the repeat observations, we make use of the 51 539 spectra of explicit repeat observations (typically at different nights) of stars, not the three individual observations scheduled for each star. Such repeat observations were mainly performed for the TESS-HERMES as well as bulge and cluster observations, but a smaller contribution comes from repeat observations of GALAH fields with bad seeing. Checks of the parameter distribution of the repeat observations and the overall sample suggest that they are representative of the sample.

The uncertainties in terms of accuracy and mean expected precision at $S/N = 40$ for the stellar parameters are listed in Table 2. We explain how we estimate the accuracy in Section 4.1¹² and elaborate on the choice of uncertainty combination when we assess the precision of the stellar parameters in Section 4.2. To identify the stars and spectra that have less reliable or unreliable information, we have implemented a combination of the flagging algorithms already applied to GALAH DR2 (see Buder et al. 2018) and new algorithms, which we will present in Section 4.3.

4.1 Accuracy of stellar parameters

4.1.1 Effective temperature

Our effective temperatures are estimated from our spectra rather than photometry and because they correspond to the best-fitting spectroscopic solution, we do report them rather than values calibrated to the photometric scale, but assess their accuracy.

We see typically good agreement with the GBS that are representative of the stars in this data release, as well as with the general trends from the IRFM method within the uncertainties, as laid out below. We therefore do not correct biases or trends for T_{eff} and use the scatter with respect to the GBS as accuracy measure for our T_{eff} . For purposes that need the temperatures to be tied to the photometric scale, we report however also IRFM temperatures to allow users to (re-)assess the temperatures and possible uncertainties on a star-by-star basis.

¹²For v_{broad} , we used the comparison with the *Gaia* FGK Benchmark Stars and estimate the accuracy via the scatter of 2 km s^{-1} with respect to the square sum of the rotational and macroturbulence velocity as accuracy limit.

4.1.1.1 Gaia FGK benchmark stars (GBS) We have observed the GBS (Jofré et al. 2014, 2015; Heiter et al. 2015b; Hawkins et al. 2016; Jofré et al. 2018) in the Southern hemisphere as reference stars with external non-spectroscopic measurements of stellar parameters. Their reference T_{eff} are based on angular diameter measurements (e.g. Karovicova et al. 2018, 2020) and when we compare with the GALAH+ DR3 results (blue error bars in upper panel of Fig. 6), we find an excellent agreement with these temperatures for most of the stars between 3500 and 6250 K. We note, however, significant differences for the two massive ($\sim 3 M_{\odot}$) giant stars ξ Hya, ϵ Vir, and the subgiant ϵ For. For these three stars, both $\log g$ and $[\text{Fe}/\text{H}]$ agree with the benchmark values within the uncertainties, however. We also notice an increasing disagreement for F stars (hotter than 6250 K), that is Procyon, HD 84937, HD 49933. None the less, our estimated values of $\log g$ and $[\text{Fe}/\text{H}]$ also agree within the uncertainties. We note, however, that the majority of stars of the GALAH sample have significantly lower masses (on average $1.08 \pm 0.28 M_{\odot}$) than these stars.

4.1.1.2 Infrared flux method (IRFM) temperatures We apply the IRFM (Casagrande et al. 2010) to estimate photometric T_{eff} . We use the 2MASS and *Gaia* photometry to estimate photometric temperatures as described by Casagrande et al. (2020) and compare the differences between these temperatures in Fig. 7. Because the IRFM is sensitive to extinction, we subsequently limit the quantitative comparison (stating 16th, 50th, and 84th percentiles) to stars with small extinction $E(B - V) < 0.15$ mag (see panel d). Most of the outliers can be explained by high extinction values (compare panel b and d).

The overall agreement is good for stars with lower temperatures ($T_{\text{eff}} < 5500$ K, see panel a) as well as stars with lower surface gravities ($\log g < 3.5$ dex, see panel b). We see a trend towards underestimated T_{eff} for hotter dwarfs, similar to previous GALAH analyses as well as the trend of the few benchmark stars.

For giants ($T_{\text{eff}} < 5500$ K and $\log g < 3.5$ dex) we find a very good agreement for their whole temperature range of -6_{-78}^{+80} K. For stars in the red clump region ($T_{\text{eff}} = 4800 \pm 400$ K, $\log g = 2.4 \pm 0.2$ dex), we find a difference of 2_{-75}^{+74} K.

When inspecting dwarfs ($T_{\text{eff}} \geq 5500$ K or $\log g \geq 3.5$ dex) in bins of 4125..(250)..7250 K (covering 97 per cent of the dwarfs), we find an increasing differences from -8_{-133}^{+138} K at 4500 K towards -125_{-176}^{+184} K at 6750 K. For Solar twins, that is stars similar to the Solar T_{eff} , $\log g$, and $[\text{Fe}/\text{H}]$ within 100 K, 0.1 dex, 0.1 dex following the definition by Bedell et al. (2018), we find a typical difference of -95_{-119}^{+128} K.

Because the distribution of overall T_{eff} difference as a function of $[\text{Fe}/\text{H}]$ (panel c) is not clear enough for a diagnostic of $[\text{Fe}/\text{H}]$ trends, we analyse the difference as a function of different $[\text{Fe}/\text{H}]$ bins for dwarfs (panel e) and giants (panel f). We find that our estimated T_{eff} best agrees for stars with Solar $[\text{Fe}/\text{H}]$ (coinciding with the peak of the GALAH metallicity distribution function) but we tend to overestimate T_{eff} for stars with super-Solar $[\text{Fe}/\text{H}]$, while we tend to underestimate them for stars with sub-Solar $[\text{Fe}/\text{H}]$.

We note that discrepancies between spectroscopic and photometric temperatures, similar to the offsets that we find of $-1.3_{-2.2}^{+2.4}$ per cent on average, are common (see e.g. Mészáros et al. 2013) and it is contentious if they should be corrected or not. Given that our spectroscopic temperatures correspond to the best spectroscopic fit, we choose to not correct our spectroscopic temperatures, unlike, for example, the approach followed by the APOGEE collaboration (Jönsson et al. 2020). We do, however, provide IRFM temperatures along with adopted reddening values in our main catalogue. We note

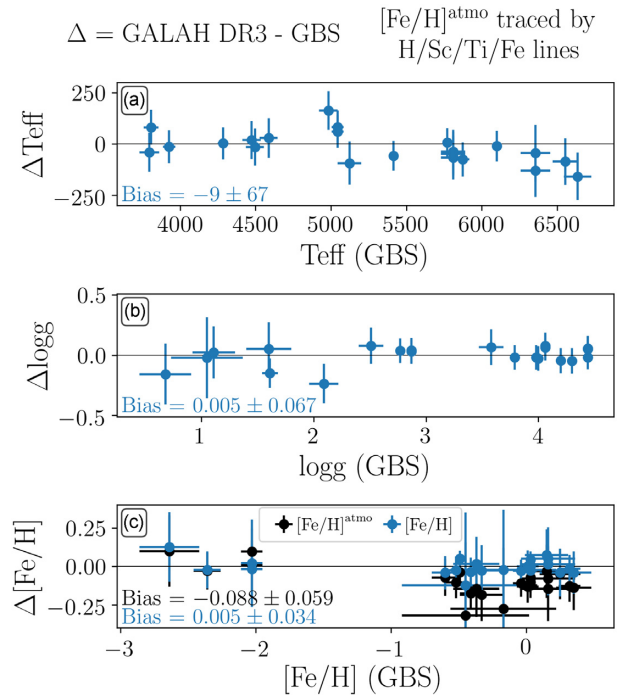


Figure 6. Comparison of the stellar parameters T_{eff} (top), $\log g$ (middle), and $[\text{Fe}/\text{H}]$ (bottom) for the observed *Gaia* FGK Benchmark stars. Differences are stated as GALAH+ DR3 – GBS (Jofré et al. 2018) and biases are error-weighted. The biases of T_{eff} are small but show similar to previous data releases, systematic deviations for F stars. The biases of $\log g$ are small thanks to the improved $\log g$ estimation. The disagreement between the GBS $\log g$ values and ours has decreased significantly from DR2 (-0.06 ± 0.16 dex). During the stellar parameter estimation, the atmospheric iron abundance (black error bars) is estimated from mask regions of well selected H, Ti, Sc, and Fe lines and underestimates the true iron abundance. For the abundance fits, we have thus increased the atmospheric iron abundance by $+0.1$ dex. The final reported iron abundance (blue error bars) is only based on Fe lines and shows no bias. GBS with $T_{\text{eff}} > 6000$ K were observed with $S/N \sim 60$, whereas the other stars all cover S/N between 150 and 800.

that we have not included the results of the IRFM T_{eff} comparisons for our accuracy estimates of our spectroscopic T_{eff} and therefore caution the user to decide which temperatures might be more useful for their science case and decide if they want to adjust the uncertainties by a systematic factor, for example a quadratic increase of accuracy uncertainty estimated from the difference of IRFM and spectroscopic T_{eff} .

4.1.2 Surface gravity

We find excellent agreement and negligible biases between our derived surface gravities and those from the GBS, as well as those obtained for stars with asteroseismic information. Due to the larger sample size of the stars with asteroseismic information, we apply the estimated scatter of this sample as an accuracy estimate for our $\log g$.

4.1.2.1 GBS The surface gravities we obtain are in excellent agreement with the accepted values for the GBS (Heiter et al. 2015b; Jofré et al. 2018), as expected given that both studies used the same approach to estimate these via bolometric relations. Due to the different implementations of this method, it is however reassuring to see the excellent agreement and low scatter (second panel of Fig. 6). We note a slight disagreement for the highest bolometric luminosities and masses, which cancel each other out and lead to a

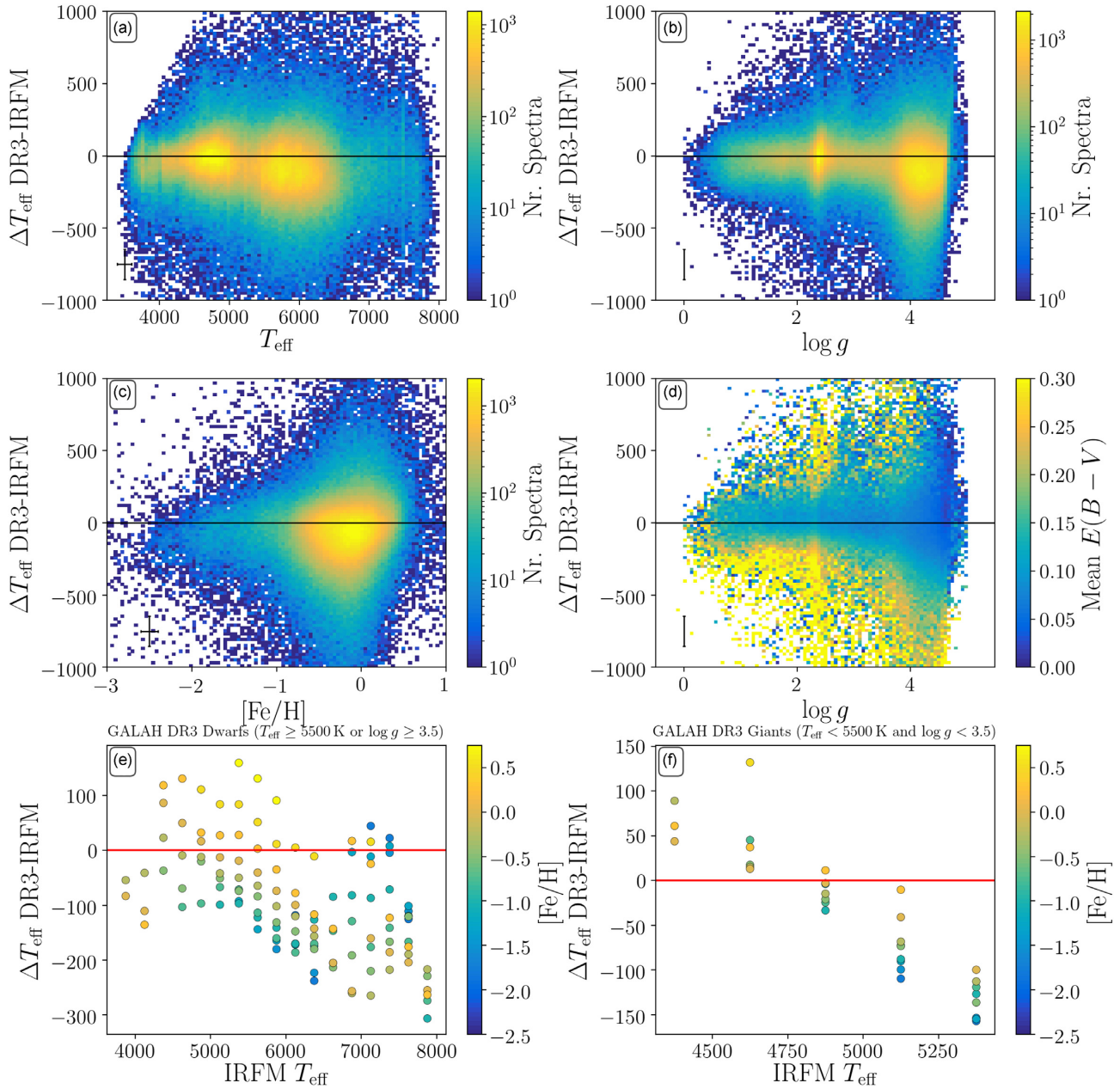


Figure 7. Comparisons of spectroscopically determined T_{eff} with T_{eff} estimated via the Infrared Flux method following Casagrande et al. (2010), Casagrande et al. (2020). Panel (a)–(c) Density distributions of the deviation of GALAH+ DR3 versus IRFM T_{eff} as a function of GALAH+ DR3 T_{eff} , $\log g$, and $[\text{Fe}/\text{H}]$, respectively. Panel (d) Density distributions of the deviation of T_{eff} as function of GALAH+ DR3 T_{eff} coloured by the mean extinction $E(B - V)$ per bin. Panels (e) and (f) Distributions of deviations of T_{eff} (3875..(250)..7875 K) as a function of IRFM T_{eff} for different $[\text{Fe}/\text{H}]$ bins (–2.50..(0.25)..0.75 dex) for dwarfs ($T_{\text{eff}} \geq 5500$ K or $\log g \geq 3.5$ dex) and giants (i.e. not dwarfs), respectively. Points are coloured by the $[\text{Fe}/\text{H}]$ bin and represent the median deviation for bins with at least 50 stars.

good agreement in $\log g$. The only outlier of these measurements is the giant star HD 107328 (which has the largest relative mass and $\log g$ uncertainty of the GBS and a significant change from *Hipparcos* to *Gaia* parallaxes); however, both T_{eff} and $[\text{Fe}/\text{H}]$ are in excellent agreement with the GBS values.

4.1.2.2 Stars with asteroseismic information To test the GALAH+ DR3 pipeline, we analyse a subset of 3175 spectra, for which asteroseismic ν_{max} estimates were available from the seismic SYD pipeline (Huber et al. 2009) as part of the K2 Galactic Archaeology Program (GAP) data release 3 (J. Zinn et al., in

preparation). We compare the GALAH+ DR3 pipeline (‘bolometric’ or ‘lbol’ pipeline) with an adjusted version (‘asteroseismic’ or ‘seis’ pipeline) that uses the empirical (metallicity-independent) asteroseismic scaling relations of solar-like oscillators (see e.g. Kjeldsen & Bedding 1995; Bedding et al. 2010):

$$\log g = \log g_{\odot} + \log \frac{\nu_{\text{max}}}{\nu_{\text{max},\odot}} + \log \sqrt{\frac{T_{\text{eff}}}{T_{\text{eff},\odot}}} \quad (8)$$

with $\nu_{\text{max},\odot} = 3090 \mu\text{Hz}$ (Huber et al. 2017) and $T_{\text{eff},\odot} = 5772$ K (see Table A3).

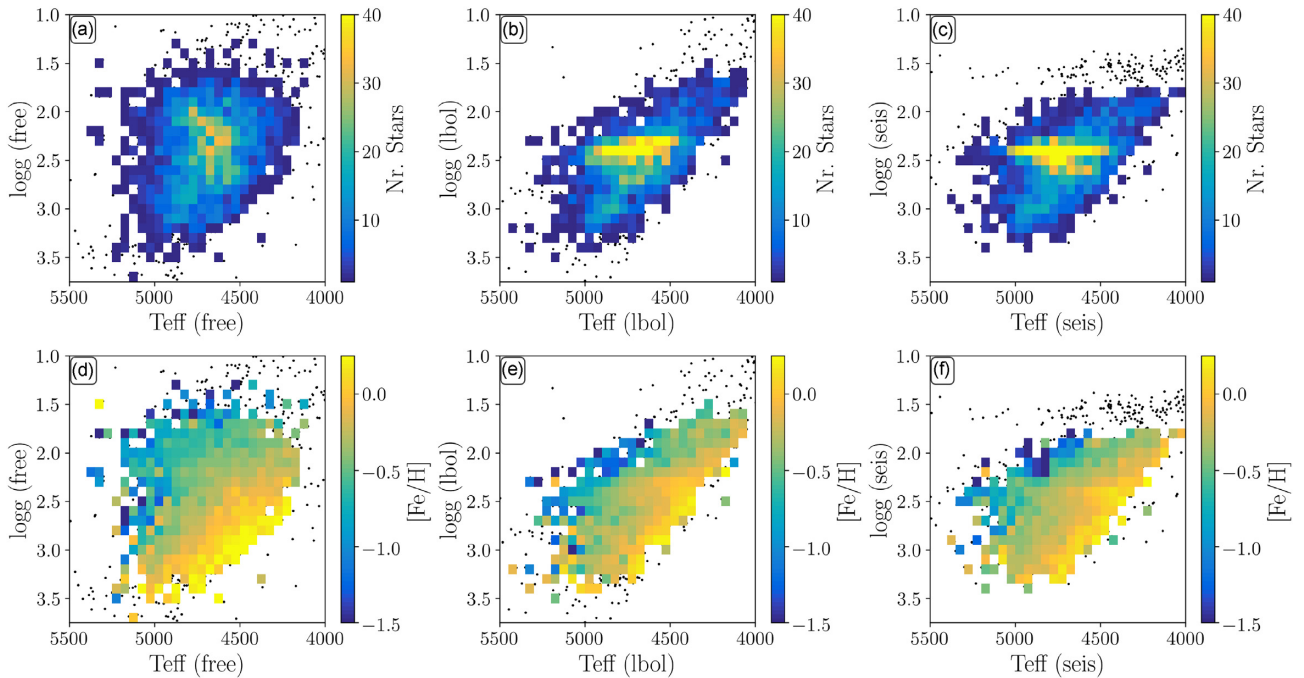


Figure 8. Results of testing different pipeline versions with ‘free’ (left-hand panels), ‘bolometric’ (middle panels), and ‘seismic’ (right-hand panels) estimates of $\log g$ for the stars with both asteroseismic and parallax information available. Shown are the number density (upper panels) as well as the mean iron abundance (lower panels) in binned distributions. The plots show that with good astrometric and photometric information, the ‘bolometric’ pipeline (chosen for GALAH+ DR3) delivers accurate results similar to the ‘seismic’ pipeline. The ‘bolometric’ pipeline further shows much smaller scatters and biases than the ‘free’ pipeline.

The difference in estimated T_{eff} of -20^{+25}_{-26} K and $[\text{Fe}/\text{H}]_{\text{atmo}}$ of $-0.02^{+0.03}_{-0.03}$ dex are both very small. Additionally, we have used the pipeline where $\log g$ is a free parameter for the spectrum fit (‘free’) to assess the improvement of our parameter estimation thanks to the use of external information (see Fig. 8). The ‘free’ pipeline can only estimate $\log g$ from the spectra and shows a significant scatter (especially for the red clump stars) for this stellar parameter, which propagates into larger scatter for T_{eff} and $[\text{Fe}/\text{H}]$ as well. With the new constraints on $\log g$ from external information from astrometry and photometry, the scatter of all parameters decreases significantly and the red clump stars show a tight distribution around $\log g \sim 2.4$ dex. This is consistent with the most reliable measurements, which take into account asteroseismic information (right-hand panels), although even finer structure within this small sample such as the separation between the red clump and the RGB bump is only seen when seismology is included.

We assess the final accuracy of $\log g$ (and not the initial performance test described above) with all SYD-pipeline K2 GAP measurements from J. Zinn et al. (in preparation) overlapping with GALAH+ DR3. When comparing the difference of the final values for $\log g$ estimated via equation (8) (seis) and GALAH+ DR3 (lbol) in Fig. 9(a), we see that both the difference and the scatter of the $\log g$ values has decreased from -0.06 ± 0.29 dex in GALAH DR2 (see fig. 17 from Buder et al. 2018) to $-0.04^{+0.12}_{-0.11}$ dex on average and we see a good agreement with the majority of asteroseismic values (colourbar) for a large parameter range of 2 dex. We note that the raw measurements of the K2 GAP overlap included 7.5 per cent K2 dwarf observations that were blended by giants in the K2 data, a slightly higher number than the 4 per cent blends found for the *Kepler* field (Hon et al. 2019). In the final K2 GAP sample, only a few tens of dwarfs (see high $\log g$ stars in Fig. 9b) are likely blends.

4.1.3 Metallicity and iron abundance

For GALAH+ DR3, we strictly separate the notation of metallicity $[\text{M}/\text{H}]$ and iron abundance $[\text{Fe}/\text{H}]$. We also refer to the atmosphere iron abundance $\text{FE}_H\text{-ATMO}$ (of the MARCS grids and SME.feh). The last quantity is estimated mainly from Fe lines, but we also included Sc and Ti lines and thus would refer to it as pseudo-iron abundance. Only when we talk about the abundance estimated solely using Fe lines do we refer to $[\text{Fe}/\text{H}]$ or FE_H . We report the scatter of our measurements with those of the GBS as accuracy measures for both atmosphere ($\text{FE}_H\text{-ATMO}$) and pure iron abundance FE_H .

After the collection of results from the stellar parameter estimations, we compare the atmosphere iron abundance to the values from Jofré et al. (2018) and find a significant bias (see black error bars in bottom panel of Fig. 6). We have thus decided to shift the atmosphere value SME.feh by $+0.1$ dex for the later abundance estimations.

From the observation of the sky flat as Solar reference, we estimate a final zero-point value of $A(\text{Fe})_{\odot} = 7.38$. This value is significantly smaller than the literature values of 7.45 and 7.50 from Grevesse et al. (2007) and Asplund et al. (2009), respectively, and confirms that the absolute iron abundances would be estimated too low without zero-point shifts. When using this value for the computation of the final $[\text{Fe}/\text{H}]$ values, however, we find not only the Solar values, but also the GBS stars to be in agreement with the literature. We furthermore see that the scatter of this pure $[\text{Fe}/\text{H}]$ value (black) is smaller than that of the atmosphere values (blue) in Fig. 6(c).

We note, however, that the coverage of the GBS in terms of iron abundance is very sparse. This is easily visible in the bottom panel of Fig. 6 for the iron abundances around -1.5 dex, but also concerns the most metal-rich stars, especially giants, for which we have to assume that the general agreement also applies.

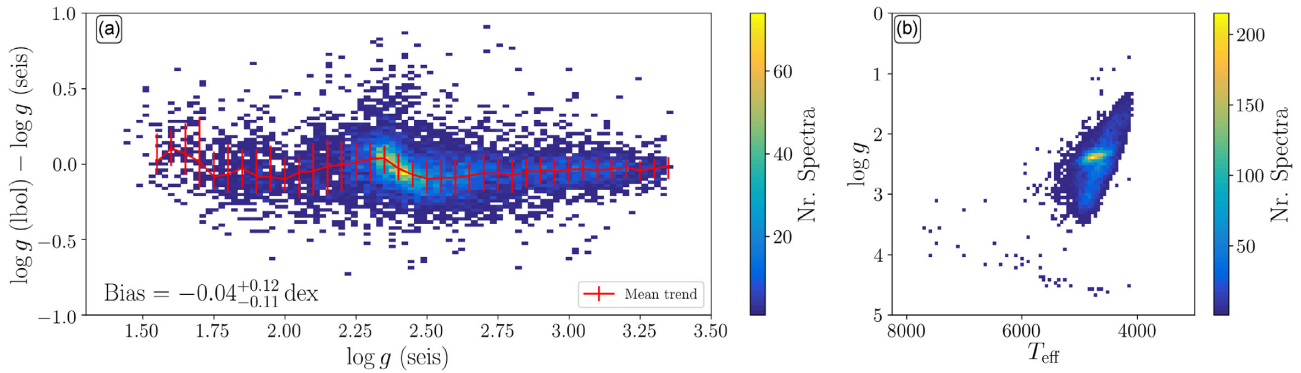


Figure 9. Comparison of surface gravities of the stars with asteroseismic information from the K2 asteroseismic analyses (SYD pipeline). Panel (a) shows the density distribution of the deviation between our surface gravities (lbol) and those estimated from scaling relations (seis). Panel (b) showing the same stars, but in the Kiel diagram. Most stars are giants with $\log g$ between 1.5 and 3.5 dex, but a few tens of dwarfs are visible. These are likely cases of photometric blends from dwarfs by giants (see the text for further details).

4.1.4 Radial velocities

In contrast to the approach taken in GALAH DR2, we have estimated the radial velocities as a free parameter in the stellar parameter estimation and have thus been able to overcome a systematic trend of the reduction pipeline, which would otherwise have been overestimating the positive and underestimating the negative radial velocity by 1 per cent, respectively.

In version 2 of our data catalogues, we provide several different estimates for the community in a value-added-catalogue and add the values that we recommend to use for each spectrum in the column `rv_galah`.¹³

For each spectrum, we at least try to fit the radial velocity as part of the spectrum synthesis comparison, reported as `rv_sme_v2`. We have identified that a wrong barycentric correction was used for shifting the reduced spectra. The first version of the SME radial velocity measurements (`rv_sme_v1`), solely based on these spectra were therefore on average lower by $0.35 \pm 0.19 \text{ km s}^{-1}$, with 14 estimates shifted by more than 1 km s^{-1} . We have uploaded a second version based on correct barycentric corrections.

In addition to the v_{rad} provided by SME as part of the stellar parameter pipeline, our VAC for v_{rad} also provides measurements which are done with the method described by Zwitter et al. (2018, 2020) via template spectra (stacked from observed GALAH spectra), rather than synthetic spectra, as well as the radial velocities reported by *Gaia* eDR3 (Gaia Collaboration 2020).

We recommend users to consider the choice of radial velocity measurement for their specific science case. Our most accurate measurements are reported via `rv_obst` and are recommended (if available) for Galactic stellar dynamics studies. If the user wants to compare radial velocities with other studies, we recommend the use of `rv_nogr_obst` (if available) or `rv_sme_v2` otherwise, as these do not correct for gravitational redshifts (and are currently the most commonly reported measurements by stellar spectroscopic surveys).

To assess the accuracy of our radial velocity estimates, we therefore focus on the comparison of measurements from `rv_nogr_obst` and `rv_sme_v2` with those from *Gaia* eDR3 and APOGEE DR16 (Jönsson et al. 2020). Here, we limit ourselves to the unflagged

GALAH spectra with sufficient signal-to-noise ratio in the second CCD, $S/N(C2) > 40$, and *Gaia* eDR3 as well as APOGEE DR16 measurements with less than 2 km s^{-1} uncertainty. The differences with respect to *Gaia* eDR3 and APOGEE DR16 can be best approximated with 2 Gaussian distributions, with the values listed in Table 3.

For the difference of the template measurements (`rv_nogr_obst`) with respect to *Gaia* eDR3, we find a narrow Gaussian peaking at $-0.02 \pm 0.48 \text{ km s}^{-1}$ and a broader Gaussian (with amplitude ratio 1:2.0) at $-0.13 \pm 1.22 \text{ km s}^{-1}$. For the stars overlapping with APOGEE DR16, the difference of `rv_sme_v2` and `VHELIO_AVG` can best be described by a narrow Gaussian peaking at $-0.02 \pm 0.25 \text{ km s}^{-1}$ and a broader Gaussian (with amplitude ratio 1:3.7) at $-0.02 \pm 0.57 \text{ km s}^{-1}$.

For the difference of the SME measurements (`rv_sme_v2`) with respect to *Gaia* eDR3, we find a narrow Gaussian peaking at $-0.09 \pm 0.45 \text{ km s}^{-1}$ and a broader Gaussian (with amplitude ratio 1:1.8) at $-0.22 \pm 1.18 \text{ km s}^{-1}$. For the stars overlapping with APOGEE DR16, the difference of `rv_sme_v2` and `VHELIO_AVG` can best be described by a narrow Gaussian peaking at $-0.02 \pm 0.25 \text{ km s}^{-1}$ and a broader Gaussian (with amplitude ratio 1:3.7) at $-0.02 \pm 0.57 \text{ km s}^{-1}$.

These comparisons confirm that `rv_nogr_obst` is very accurate and on the same scale as both *Gaia* eDR3 and APOGEE DR16 with only -0.02 km s^{-1} bias. The SME measurements (`rv_sme_v2`) are slightly underestimated, with a bias of -0.09 to -0.13 km s^{-1} . We therefore add an accuracy uncertainty of 0.1 km s^{-1} to our `rv_sme_v2` measurements and prefer the template measurements where available.

The source of the recommended, that is most accurate, values `rv_galah` is indicated via the flag `use_rv_flag`, as we outline in the catalogue description in Section 7.2.

4.2 Precision of stellar parameters

To estimate the precision of our stellar parameters, we use both internal SME covariance errors and repeat observations of the same star for all stellar parameters except for $\log g$, for which we Monte Carlo sample the uncertainties.

4.2.1 Stellar parameters except $\log g$

We have estimated the standard deviations of repeat observations for three situations: star in the same fibre for each observation, star in

¹³We have updated this notation for convenience to allow the user to easily use our best estimate of radial velocities. In version 1 of the main catalogues, we reported only the SME based radial velocities, which used a erroneous barycentric correction, as we outline in this section.

Table 3. Comparison of GALAH DR3 radial velocities methods with *Gaia* eDR3 and APOGEE DR16. We have fitted 2 Gaussian distributions to the data and report their mean values and standard deviations as well as their amplitude ratios (AR). Note that all methods except *rv_obst* do not apply a gravitational redshift (GR), leading to significant shifts between these different methods. For quality cuts applied, see the text.

Method Component	<i>rv_obst</i> (GR)			<i>rv_nogr_obst</i> (no GR)			<i>rv_sme_v2</i> (no GR)		
	Narrow (km s ⁻¹)	Broad (km s ⁻¹)	AR	Narrow (km s ⁻¹)	Broad (km s ⁻¹)	AR	Narrow (km s ⁻¹)	Broad (km s ⁻¹)	AR
<i>Gaia</i> eDR3	-0.16 ± 0.45	-0.46 ± 1.13	1:1.7	-0.02 ± 0.48	-0.13 ± 1.22	1:2.0	-0.09 ± 0.45	-0.22 ± 1.18	1:1.8
APOGEE DR16	-0.07 ± 0.18	-0.37 ± 0.44	1:0.4	-0.02 ± 0.25	-0.02 ± 0.57	1:3.7	-0.13 ± 0.25	-0.07 ± 0.68	1:5.3

different fibres and lastly all repeats irrespective of fibre. The results are shown in Fig. 10, where we plot the standard deviations as a function of S/N in CCD2¹⁴ together with the median SME covariance errors for the fitted stellar parameters T_{eff} , $\log g$, iron line abundance $[\text{Fe}/\text{H}]$, the atmosphere iron abundance $[\text{Fe}/\text{H}]$, rotational broadening v_{broad} , and radial velocity v_{rad} .

The trends of internal and repeat precision are expected to be similar, but we find that, for the stellar parameters, the uncertainties from the internal SME covariance uncertainties, based on χ^2 optimization tend to overestimate the absolute quality of fit and are typically significantly lower than those from repeat observations, although tracing them well in a relative sense, when rescaled. As discussed when introducing the final error estimation with equation (7), the two precision estimates should be the same and we thus rescale the internal SME-based uncertainties with a combination of factors and shifts, noted as (factor, shift) with (3, 7.5) for T_{eff} , (4, 0.01) for $[\text{Fe}/\text{H}]$, (2, 0.0125) for $[\text{Fe}/\text{H}]_{\text{atmo}}$, (1.75, 0.3) for v_{broad} , and (2, 0.15) for v_{rad} towards a minimum difference with respect to the exponential fit for the repeat observations (black curve in Fig. 10). For the estimation of these linear rescaling functions, we have focused on the S/N interval of 40 to 200, which typically leads to larger internal uncertainties for those stars below $S/N < 20$, for which we believe a more conservative uncertainty estimate is justifiable. We use all repeats (orange lines), because we find typically a good agreement between same (green) and different (purple) fibre repeats. Only in the case of v_{broad} , we see significant differences between the different repeat types, which is likely caused by unaccounted resolution variations which translate into a different broadening estimate of the same star in different fibres.

This rescaled internal precision now allows for a combination of the individual estimate of the fit quality (through the internal SME-based uncertainty) with the general precision expected for a given S/N , which could otherwise be underestimated when only using to the raw internal uncertainty.

We further note that we have changed our definition of S/N in these figures compared to DR2 (Buder et al. 2018) to show the S/N of the higher quality observation (DR3) instead of the lower one (DR2). The quantitative improvement of the precision from GALAH DR2 to GALAH+ DR3 is thus not necessarily an indicator of the decreasing precision, but of a more reliable precision estimate.

4.2.2 Precision of surface gravities $\log g$

We stress that $\log g$ values are not optimized from the χ^2 -determination of the spectra like the other parameters, but from equation (1). Instead of the internal SME uncertainties, we sample the parameters used for equation (1) via Monte Carlo (MC) sampling. For computational reasons, we assume the uncertainties for the formula to be Gaussian and sample the parameters with uncertainties

$\sigma(M) = 0.1 \cdot M$, $\sigma(BC) = 0.1$ mag, $\sigma(T_{\text{eff}})$, $\sigma(D_{\text{par}})$, $\sigma(K_s)$, and $\sigma(A_{K_s})$. With this approach we estimate a mean internal uncertainty for $\log g$ of 0.07 dex. With this implementation, the uncertainty is driven by the mass uncertainty (contributing 0.044 dex for star with Solar mass) and the combination of the photometric uncertainties. For stars with precise parallaxes, the parallax uncertainty is contributing only a small fraction (the median parallax uncertainty of the sample of 2.7 per cent translates into roughly 0.024 dex uncertainty in $\log g$ through equations 2 and 1), it is dominating the $\log g$ uncertainty for the 5 per cent stars with parallax uncertainties above 20 per cent (see Fig. 3).

By construction and due to the exquisite astrometric and photometric external information available, this internal precision is significantly better than the previous spectroscopic estimates from GALAH DR2. We note, however, that these estimates do not take external influences like binarity or correlations of uncertainties into account.

4.2.3 Iron abundances of cluster stars

Based on the open cluster membership analysis by Cantat-Gaudin & Anders (2020), we estimate that we have intentionally and unintentionally observed members of 75 stellar clusters. The eight open clusters with most observations are NGC 2682 (278 spectra, M 67), NGC 2632 (117, M 44, Praesepe), NGC 2516 (83), NGC 2204 (81), Ruprecht 147 (80), Melotte 22 (74), Blanco 1 (67), and NGC 6253 (50). Furthermore we have observed 10 of the 128 open clusters¹⁵ of the OCCAM survey (Donor et al. 2020), included as VAC from SDSS DR16 (Ahumada et al. 2020). The analysis of all open clusters observed with GALAH is addressed in the dedicated paper by Spina et al. (2021). Here we only focus on three open clusters which cover a large range of stellar evolutionary stages and are also reported by the OCCAM survey.¹⁶

We show the coverage of evolutionary stages for these clusters in the left-hand panels of Fig. 11 for both GALAH and OCCAM, which cover dwarfs for all clusters and giants for both NGC 2682 (M 67) and Ruprecht 147. When looking at the average values of $[\text{Fe}/\text{H}]$ for these clusters as a function of T_{eff} (middle panels) as well as $\log g$ (right-hand panels), we first see very good agreement for the average values of Melotte 22 between GALAH and OCCAM. The $[\text{Fe}/\text{H}]$ values for Ruprecht 147 and NGC 2682 disagree within the standard error of the mean, but agree within the standard deviation. We have limited the stars used for this averaging to those stars with $4500 < T_{\text{eff}} < 6500$ K. We implement these cuts to avoid systematic trends on either side of the range, where either GALAH or APOGEE/OCCAM

¹⁵These are ASCC 16 (22 spectra), ASCC 16 (22), ASCC 21 (11), Berkeley 33 (8), Melotte 22 (74), NGC 2204 (81), NGC 2232 (20), NGC 2243 (8), NGC 2318 (2), NGC 2682 (278), and Ruprecht 147 (80).

¹⁶The same plots as in Fig. 11 are available in our online documentation for all our clusters observed by GALAH.

¹⁴For the repeat observations we use the S/N of the higher quality observation.

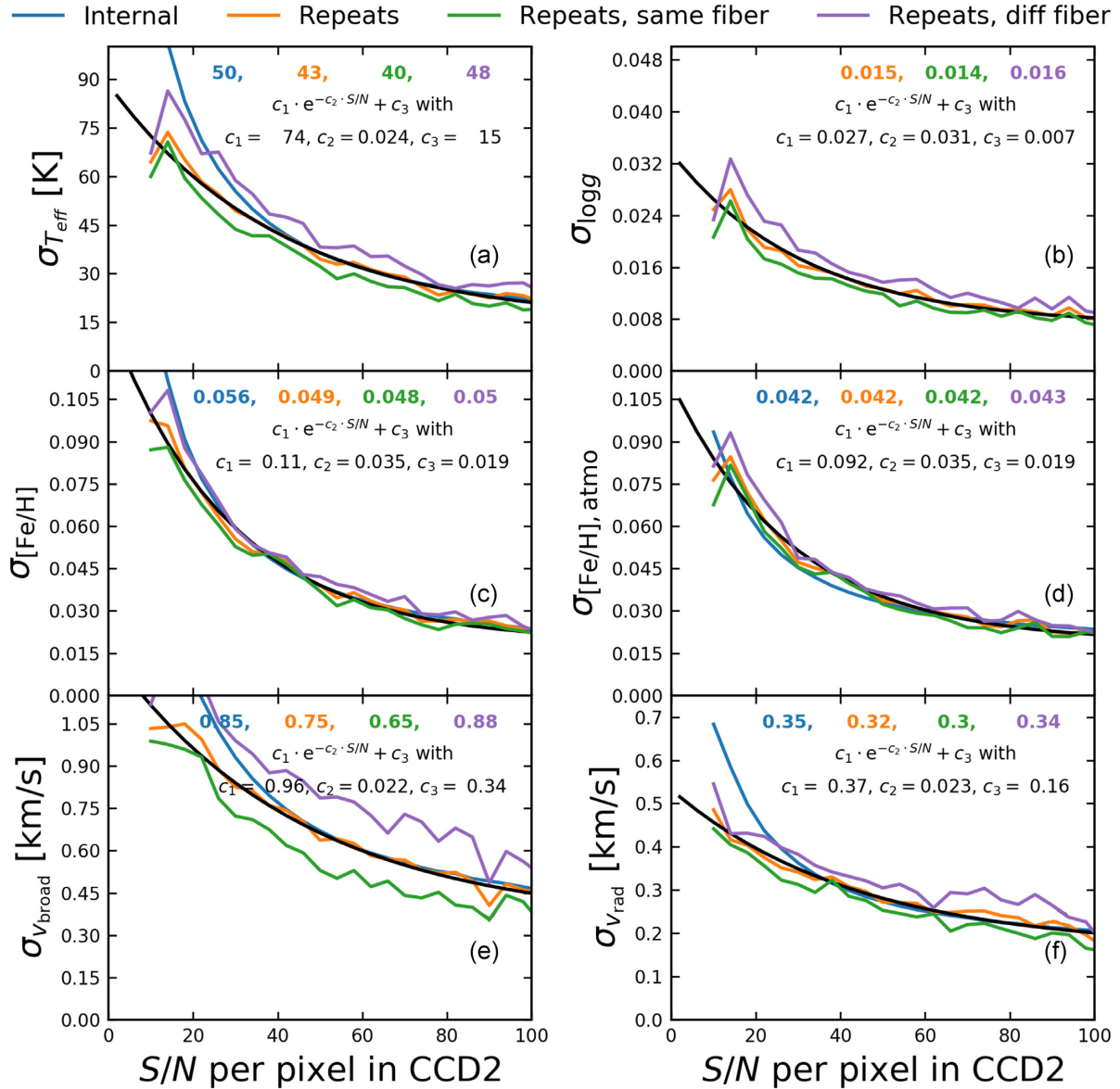


Figure 10. Precision estimates from internal SME covariance uncertainties (blue) as well as standard deviations from all (orange), same fibre (green), and different fibre (violet) repeat observations. The black lines indicate the exponential fit to the orange lines. The functional form and best-fitting coefficients are annotated for each panel and were used for the final assessment of precision. The numbers given across the top of each panel indicate the uncertainties estimated for $S/N = 40$ per pixel, similar to fig. 15 from Buder et al. (2018). Note that the internal precision was already adjusted for each parameter with the scaling relations outlined in the text. The internal precision for $\log g$ is not given, because it was not fitted, but estimated via external information, as outlined in the text on the precision of $\log g$.

underperforms. The parallax uncertainties of the cluster members are on average well below 12 per cent, suggesting that these observations should be reliable and representative for validation purposes.

We also have observed several globular clusters, and plot the Kiel diagrams as well as $[\text{Fe}/\text{H}]$ histograms for four of them, namely 47 Tuc, NGC 288, NGC 7099 (M30), and NGC 5139 (ω Cen) in the four panels of Fig. 12. For each of them we show the unflagged (black) and flagged (red) measurements from GALAH+ DR3 and where possible also the likely members observed as part of APOGEE DR16.¹⁷ In particular, 47 Tuc and ω Cen show excellent

¹⁷We have selected likely members via selecting stars within the mean cluster estimates by Baumgardt et al. (2019).

agreement between APOGEE DR16 and GALAH+ DR3 in their mean $[\text{Fe}/\text{H}]$. The $[\text{Fe}/\text{H}]$ distribution looks sharper for APOGEE in 47 Tuc due to that survey's higher S/N observations and the spurious trends between $[\text{Fe}/\text{H}]$ and T_{eff} , and $[\text{Fe}/\text{H}]$ and $\log g$, found in the GALAH data. For ω Cen they look similar and show a large spread in $[\text{Fe}/\text{H}]$. When comparing the literature compilation by Harris (1996, H96) with our mean, standard deviation, and standard error $[\text{Fe}/\text{H}]$ values (subsequently $\mu \pm \sigma \pm \sigma_{\mu}$), we obtain

$$\begin{aligned} [\text{Fe}/\text{H}] &= -0.70 \pm 0.12 \pm 0.01 \text{ dex (47 Tuc, } -0.76 \text{ H96),} \\ [\text{Fe}/\text{H}] &= -0.95 \pm 0.18 \pm 0.07 \text{ dex (NGC 6362, } -1.06 \text{ H96),} \\ [\text{Fe}/\text{H}] &= -1.99 \pm 0.28 \pm 0.07 \text{ dex (NGC 6397, } -1.91 \text{ H96),} \\ [\text{Fe}/\text{H}] &= -2.20 \pm 0.19 \pm 0.04 \text{ dex (NGC 7099, } -2.12 \text{ H96),} \\ [\text{Fe}/\text{H}] &= -1.53 \pm 0.32 \pm 0.02 \text{ dex (NGC 5139, } -1.57 \text{ H96),} \end{aligned}$$

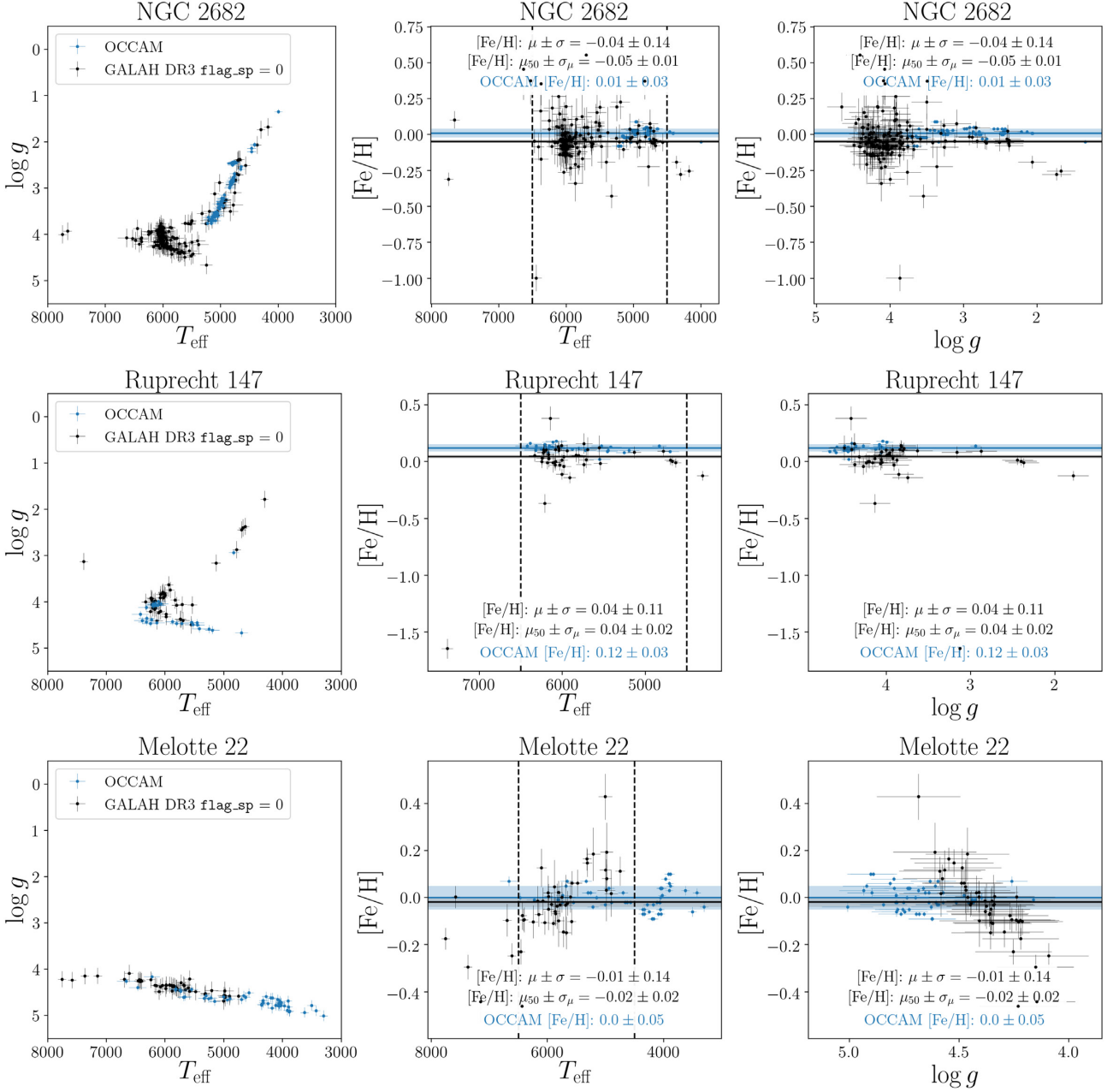


Figure 11. Stellar parameters (combinations of T_{eff} , $\log g$, and $[\text{Fe}/\text{H}]$) of the three open clusters NGC 2682 (278 spectra, M 67), Ruprecht 147 (80), and Melotte 22 with data from GALAH+ DR3 (unflagged in black). Unflagged data from the OCCAM survey (Donor et al. 2020) is plotted in blue. The horizontal bars indicate the mean abundances of the clusters from GALAH in grey (estimated from unflagged measurements for stars with $4500 < T_{\text{eff}} < 6500$ K) and the OCCAM survey (blue).

$[\text{Fe}/\text{H}] = -0.97 \pm 0.06 \pm 0.02$ dex (NGC 1851, -1.26 H96),
 $[\text{Fe}/\text{H}] = -1.07 \pm 0.09 \pm 0.01$ dex (NGC 288, -1.24 H96), and
 $[\text{Fe}/\text{H}] = -1.00 \pm 0.10 \pm 0.01$ dex (NGC 362, -1.16 H96).

Thus we find good agreement for high and low $[\text{Fe}/\text{H}]$, that is for 47 Tuc, NGC 6362, NGC 6397, NGC 7099, and NGC 5139. However, for the intermediate $[\text{Fe}/\text{H}]$ clusters NGC 1851, NGC 288, and NGC 362 we find disagreement with Harris (1996), for which we have no explanation. While APOGEE DR16 also has higher $[\text{Fe}/\text{H}]$ for NGC 1851 (-1.08 ± 0.07 dex) and NGC 362 (-1.09 ± 0.05 dex), their $[\text{Fe}/\text{H}]$ for NGC 288 agrees with Harris (1996). We note that the parallax uncertainties of stars in each of the three clusters is 30–40 per cent, which is significant and significantly

higher than the uncertainties for 95 per cent of GALAH’s targets. Taking also into account the parallax uncertainties of NGC 7099 and NGC 5139 of on average 60 and 46 per cent respectively, we conclude that these clusters are not suitable to reliably validate our pipeline.

4.2.4 Stellar parameters of wide binaries

We used the approach by El-Badry & Rix (2018) to select wide binaries using *Gaia* and further limit the selection to those with similar GALAH+ DR3 v_{rad} (within 1 km s^{-1}). We find 268 pairs, including dwarf-giant pairs. In Fig. 13 we plot the stellar parameters

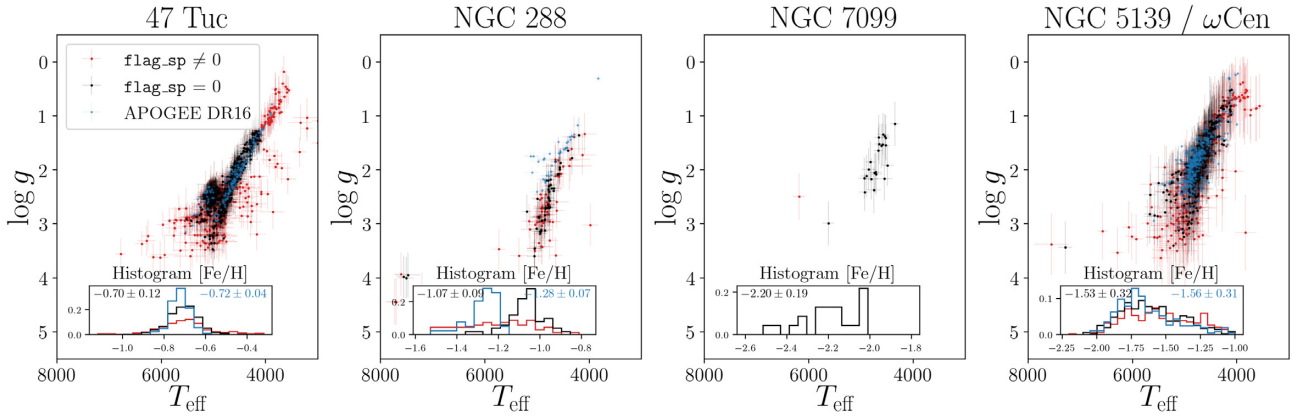


Figure 12. Kiel diagrams (T_{eff} versus $\log g$) for four globular clusters observed by GALAH. Unflagged measurements are shown in black, flagged ones in red. When available, unflagged data from APOGEE DR16 survey (Ahumada et al. 2020) is plotted in blue. Inset plots in each panel indicate the normalized $[\text{Fe}/\text{H}]$ distribution of the plotted stars with text annotating the simple mean and standard deviations of these stars.

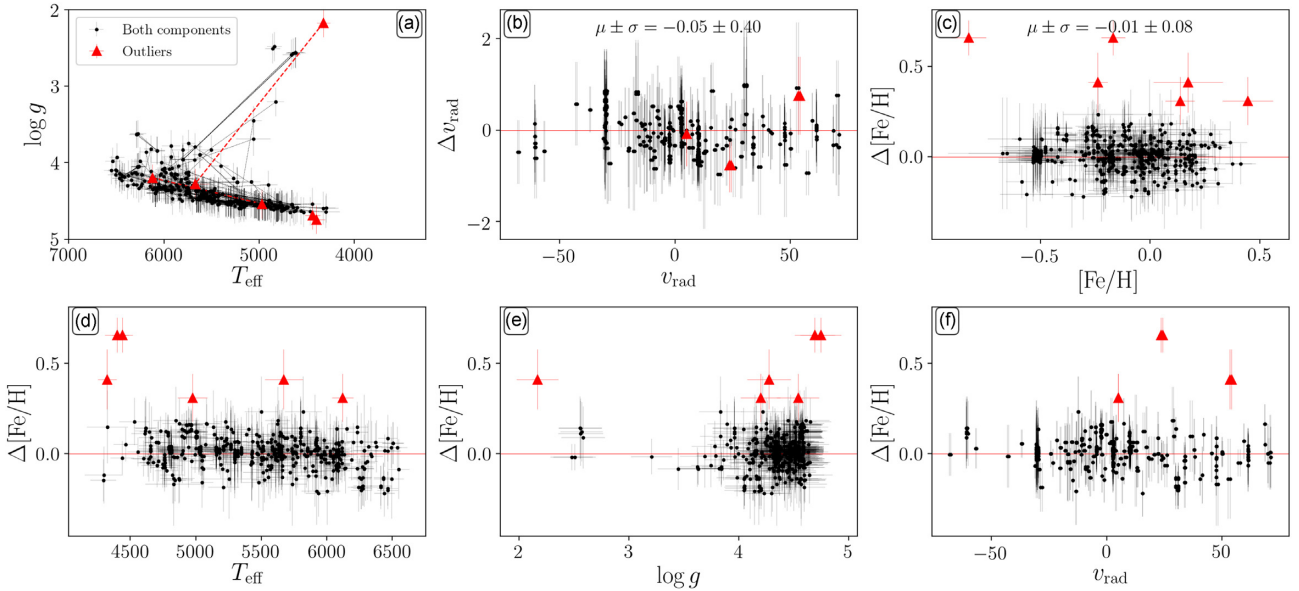


Figure 13. Comparison of stellar parameters T_{eff} , $\log g$, $[\text{Fe}/\text{H}]$, and v_{rad} for wide binaries identified with the algorithm by El-Badry & Rix (2018). We plot different combinations of these parameters as references (black) and assess the difference in $[\text{Fe}/\text{H}]$ and v_{rad} . The red dots show significant outliers in $\Delta[\text{Fe}/\text{H}]$, that is, two very cool dwarfs as well as two stars with more than 1000 K difference in T_{eff} (see panel d). We include stars with `flag_sp` up to 128.

T_{eff} , $\log g$, $[\text{Fe}/\text{H}]$, and v_{rad} to illustrate the difference of $[\text{Fe}/\text{H}]$ and v_{rad} for these stars with sometimes quite different stellar parameters. We want to stress that we include also stars with `flag_sp` up to 128 (for example the very cool, flagged stars as well as apparent photometric binary stars with unreliable $\log g$). As previous studies have shown (El-Badry et al. 2018b; El-Badry & Rix 2018), we expect very similar abundances for these pairs and indeed can confirm that their $[\text{Fe}/\text{H}]$ and v_{rad} are consistent within the uncertainties for almost all cases. The average differences of $\Delta v_{\text{rad}} = -0.05 \pm 0.41 \text{ km s}^{-1}$ and $\Delta[\text{Fe}/\text{H}] = -0.01 \pm 0.08 \text{ dex}$ show excellent agreement over large scales (when neglecting the 8 outliers of 268 pairs, shown in red). We furthermore do not see significant trends of the differences of $[\text{Fe}/\text{H}]$ with T_{eff} , $\log g$, $[\text{Fe}/\text{H}]$, or v_{rad} , which lends confidence that our analysis is reliable within the stellar parameter range of the observed wide binaries. Even most of the dwarf-giant pairs show a very good agreement.

4.3 Flagging of stellar parameters

After the stellar parameters have been estimated, we raise flags according to the individual criteria listed in Table 4. Fig. 14 shows the derived parameter values associated with all flagged spectra. The most used flags are 8 (8.6 per cent), 1 (8.5 per cent), 256 (8.0 per cent), 4 (5.6 per cent), 512 (2.4 per cent), and 1024 (2.2 per cent). Less than 2 per cent of spectra have raised flags 2, 16, 32, 64, or 128.

As for GALAH DR2 (Buder et al. 2018), we have applied the algorithm developed by Traven et al. (2017), which combined the dimensionality reduction method t-SNE (van der Maaten & Hinton 2008) with the clustering algorithm DBSCAN (Ester et al. 1996) to arrange similar looking spectra close to each other. With these techniques we have been able to identify clusters of spectra with reduction issues, emission features, as well as clear line-splitting binaries. We have further identified possible astrometric binaries or

Table 4. Flags used for GALAH+ DR3 to estimate the final bit-flag `flag_sp` (stellar parameters), `flag_X.fe` (final reported element abundances), and `ind.flag_X1234` (individual raw line/element abundances measurements) via addition of the individual bitmask flags.

flag_sp	
1	<i>Gaia</i> RUWE > 1.4 (unreliable astrometric solution, see Lindegren 2018)
2	Unreliable broadening
4	Low S/N (below 10 for CCD 2)
8	Reduction issues a) Wavelength solution (propagating of <code>red_flag</code>), b) t-SNE projected reduction issues, c) Negative/positive fluxes, spikes, etc.
16	t-SNE projected emission features
32	t-SNE projected binaries
64	Binary sequence/pre-main sequence flag
128	SNR-dependent high SME chi2 (bad fit)
256	Problems with Fe: line flux is not between 0.03 and 1.00, [Fe/H]unreliable, or blending suspected
512	SME did not finish a) No convergence == non-finite stellar parameters b) Gaussian RV fit failed
1024	MARCS grid limit reached or outside of reasonable parameter range
flag_X.fe	
1	Upper Limit
32	No reliable measurement reported
ind.flag_X1234	
1	Upper Limit
2	Bad fit / large χ^2
4	Uncertain measurement / saturation
8	Bad wavelength solution / rv for Li6708
16	Bad stellar parameter flag (≥ 128)
32	No measurement available

pre-main sequence stars (`flag_sp` = 64) by selecting the oldest PARSEC isochrones for the particular iron abundance of each star and selecting all stars with surface gravity lower by $\Delta \log g = 0.15$ and cooler by $\Delta T_{\text{eff}} = 150$ K. This selection is most effective for the identification of binaries on the secondary main-sequence (with slightly lower $\log g$). For stars with equal bolometric luminosity, for example a binary system with the same stellar parameters, the estimated $\log g$ can be smaller by up to ~ 0.3 . This deviation can be approximated via equation (1) when assuming that the bolometric luminosity of the system is twice that of a single star and the mass is estimated to be that of a single star, so that $\Delta \log g \sim -\log L_{\text{bol,binary}} + \log L_{\text{bol,single}} = -\log(2 \cdot L_{\text{bol,single}}) + \log L_{\text{bol,single}} = -\log 2$. We have also identified unreliable parameter estimates for the coolest bright giants, for which unreasonably low iron abundances have been estimated (see tip of the RGB in Fig. 14d with many stars with incorrectly low [Fe/H]). We elaborate on this in Section 6 when addressing v_{mic} and metallicity trends. Based on the overall distribution of stars in the S/N versus χ^2 plane (median $\chi^2 = 0.748$), we have implemented a χ^2 flag (`flag_sp` = 128) for $\chi^2 > 0.1 \cdot S/N + \exp(0.08 \cdot S/N)$

5 VALIDATION OF ELEMENT ABUNDANCES

We validate element abundances in terms of accuracy and precision and discuss the two validations separately. Unlike for GALAH DR2, we are now not limited by the influence of the training set for this

data release. We have also tried to estimate more upper limits and outline our approach in this section, followed by the description of our flagging algorithms with the aim to allow the community to make informed choices on the use of abundance measurements. As for the previous data releases, we want to stress that we discourage the use of flagged element abundances without consideration of the possible systematics that the inclusion of these flagged measurements can introduce.

For our accuracy studies (Section 5.1), the techniques we could adopt for comparisons with accurate benchmark are limited. Contrary to the stellar parameters, where multiple methods, and especially those which are independent of spectroscopy, are available for accuracy estimations, the available benchmarks for abundance accuracy are based on spectroscopy and – with exception of the Sun and Solar twins – also strongly limited in terms of accuracy (e.g. due to neglected 3D and non-LTE effects). We are therefore only using the Sun and Solar twins to validate the accuracy of our measurements to zeroth order (abundance zero points). We do not assess our abundance accuracy quantitatively beyond this, but we do also investigate systematic trends with respect to other spectroscopic studies presented in the literature. We want to stress that a proper estimation of the accuracy uncertainties would have to involve the systematic influence of the individual stellar parameters within their uncertainties, the uncertainties of the absolute abundances / zero points in terms of $\log gf$ values and additional uncertainties from the fit to the sky flat, Arcturus, the comparison with the Solar circle sample, as well as the Solar twin comparison. For computational reasons we have not been able to quantify all of these influences, but report them if possible (see e.g. Table A2).

Our precision estimates for abundances show a similar behaviour to that of the fitting uncertainties $e_{\text{fit}}(X)$ and the S/N -dependent repeat uncertainties $e_{\text{repeats}}(X, S/N)$, as we will explore in Section 5.2. Our reported final uncertainties are thus limited to a formula depending on element/line X and S/N of CCD2

$$e_{\text{final}}^2(X, S/N) = \max[e_{\text{fit}}(X), e_{\text{repeats}}(X, S/N)]. \quad (9)$$

5.1 Accuracy of element abundances

We estimate our element abundances by changing the absolute abundance for each element that is measured in the initially scaled-Solar chemical composition by Grevesse et al. (2007) of the model atmosphere. We convert the abundances to the customary astronomical scale for logarithmic abundances and report the raw values of these measurements, $A(X1234)$ for the 1234 Å line of element X in the `allspec` catalogue (see Section 7.2). We subtract the Solar value $A(X1234)$, that we define for this data release (see Table A2), from this measurement to estimate the ratio $[X/H]$ and for elements other than Fe, we further subtract the iron abundance to estimate the ratio $[X/Fe]$.

In addition to the definition of the abundance zero points, we also validated the accuracy of our element abundances by comparison to measurements of the GBS and Solar twin stars, as well as members of open and globular clusters.

5.1.1 Abundance zero points

Following the definition of the bracket notation, the Solar value $A(X1234)$ should be strictly estimated from the measurement of the particular line in the Solar spectrum. For several lines within the GALAH wavelength range, however, we are facing difficulties in estimating the Solar $A(X1234)$. First, via 2df-HERMES, we can

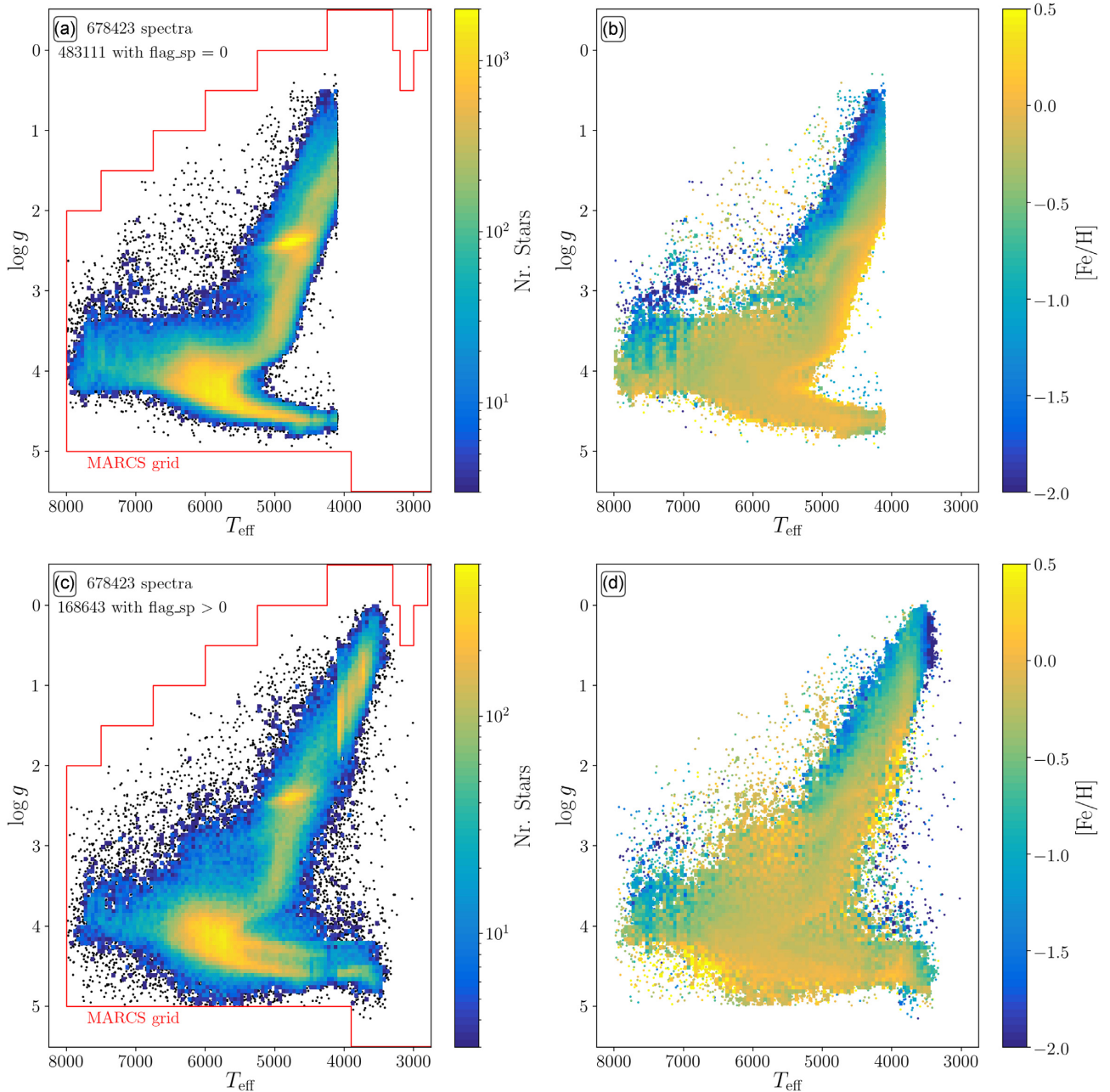


Figure 14. Density and mean [Fe/H] distribution in Kiel diagrams (T_{eff} versus $\log g$) for the spectra of GALAH+DR3. Panels (a) and (c) show the density distribution of all unflagged and flagged spectra, respectively (note that cool stars are typically flagged as unreliable due to issues with [Fe/H] as outlined in Section 6. Panels (b) and (d) show the same distribution as panels (a) and (c), but here coloured by mean [Fe/H] values for each bin. The total number of spectra and those with or without flags are annotated in the upper left-hand corner of the left-hand panels. In the same panels, red lines indicate the grid limit of the MARCS atmosphere grid, which marks the limits of the synthesis computations.

only perform sky (flat) observations rather than observing the Sun directly. Secondly, our observation setup is much shorter as for the normal setup of our observations. Thirdly, some lines are either not detectable (even within high S/N spectra) or their equivalent width or line strength does not increase significantly with increasing $A(X)$, that is, we perform a measurement at a plateau on the curve of growth. Contrary to many other studies or surveys, we choose to report the absolute abundances, and only use laboratory oscillator strengths ($\log gf$) rather than tuning these astrophysically based on the Solar spectrum with literature abundances. There are thus several

solutions available to still estimate abundance zero points, which we will discuss subsequently:

- (i) Measure $A(X)$ from the same line in Solar / sky flat / asteroid spectrum.
- (ii) Use a different line in the Solar spectrum (because $A(X)$ has to be the same).
- (iii) Use another benchmark star (like Arcturus) via bridge measurements. To do this, one would measure the line that is weak in the Sun in Arcturus as well as another line of the element that is

strong enough in both stars. In that case the difference in $A(X)$ for the lines in Arcturus can be used to transfer them on to lines in the Sun.

(iv) Use the element abundance ratios of stars in the Solar circle, for studies suggest that the abundances should be Solar. APOGEE has followed this approach to estimate their zero points since their DR14 (see Holtzman et al. 2018; Ahumada et al. 2020).

(v) Compare with a literature study, e.g. via the estimates for Arcturus (e.g. Ramírez & Allende Prieto 2011), Solar twins (e.g. Bedell et al. 2018), or the overlap with a different survey, e.g. APOGEE DR16 (Ahumada et al. 2020).

For GALAH+ DR3 we try to use the first method whenever reliable and validate it using the other approaches. Whenever this approach was not advisable or the differences to the other methods were too significant (pointing to issues in the sky flat spectra), we used the fourth and fifth option to ensure the best overall consistency.

Ultimately, we have decided to adopt the zero points for the lines and elements that are stated in Table A2. For convenience, we also list the values estimated by Asplund et al. (2009) to allow the identification of lines with issues such as possibly erroneous $\log gf$ values. We also list the results for the aforementioned sky flat of GALAH+ DR3 as well as the average abundances for stars in the Solar circle with near-Solar iron abundances.¹⁸ We expect that this data release will be used in combination with APOGEE DR16 to explore the Galaxy, so we also list the values from APOGEE DR16 for the asteroid 4 Vesta as well as the differences of the overlapping observations¹⁹ of GALAH+ DR3 and APOGEE DR16.

We want to stress that more work is needed to further scrutinize the line selection and abundance zero points. Due to time and computation restrictions during the implementation of the new non-LTE grids, we have only been able to run these elements combined, rather than line-by-line. However, we have found that the line-by-line analysis of element abundances is important for several elements (e.g. Al, Ca, and Ba), which are estimated from several different HERMES bands, and thus suffer from unreliable wavelength solutions in either band, and has to be done in future releases to improve the accuracy and precision of abundance measurements further.

5.1.2 Abundances of Arcturus and other GBS stars

For the validation of our abundance accuracy, we also turn to the best studied giant star, Arcturus, and the *Gaia* FGK benchmark stars. For Arcturus, we use the seminal study by Ramírez & Allende Prieto (2011), which is also used by APOGEE as reference. We list the values for Arcturus in Table A4, which in general show good agreement between our measurements and those of Ramírez & Allende Prieto (2011), both performed in the optical.

For the GBS, we use the compilation by Jofré et al. (2018) to compare average $[X/Fe]$ differences (see Table 5). All values suggest good agreement in light of the total median GBS uncertainties of 0.11 – 0.16 dex for each of the elements.

¹⁸We select these stars via $-0.1 < fe_h < 0.1$, $r_{est} < 500$, $snr_{c2_iraf} > 40$, $flag_cannon = 0$, $4500 < t_{eff} < 6500$, and for abundances of element X additionally $flag_{X,fe} = 0$.

¹⁹We have used all x-matches, including repeats, via 2MASS IDs and then further restricted the overlap sample to stars with $flag_{sp} = 0$, $snr_{c2_iraf} > 100$, $ASPCAFFLAG = 0$, $SNR > 100$, and for abundances additionally to reasonable, finite measurements ($[X/Fe] > -5$ dex) of unflagged elements with $flag_{X,fe} = 0$ and $X_{FE_FLAG} = 0$.

Table 5. Average differences of GALAH+ DR3 abundances with respect to the compilation by Jofré et al. (2018).

DR3-GBS	16/50/84th percentile
$\Delta[Mg/Fe]$	$0.03^{+0.05}_{-0.07}$ dex
$\Delta[Si/Fe]$	$0.03^{+0.05}_{-0.03}$ dex
$\Delta[Ca/Fe]$	$0.00^{+0.20}_{-0.17}$ dex
$\Delta[Ti/Fe]$	$0.02^{+0.06}_{-0.11}$ dex
$\Delta[Sc/Fe]$	$0.06^{+0.08}_{-0.03}$ dex
$\Delta[V/Fe]$	$0.00^{+0.18}_{-0.10}$ dex
$\Delta[Cr/Fe]$	$-0.03^{+0.09}_{-0.04}$ dex
$\Delta[Mn/Fe]$	$0.03^{+0.17}_{-0.14}$ dex
$\Delta[Co/Fe]$	$0.07^{+0.04}_{-0.12}$ dex
$\Delta[Ni/Fe]$	$0.04^{+0.13}_{-0.03}$ dex

5.1.3 Abundances of the Solar twins

We compare the abundances of Solar twins in the Solar neighbourhood in Fig. 15 with the results from the studies performed by Spina et al. (2016) and Bedell et al. (2018). We follow the definition of these studies and select high-quality Solar twin abundances with the selection of $\Delta T_{eff} < 100$ K, $\Delta \log g < 0.1$ dex, and $\Delta[Fe/H] < 0.1$ dex with respect to the Solar listed in Table A3. For such stars, these and other studies (e.g. Nissen 2015) have found tight correlations with abundances and stellar ages, that is, chemical clocks. Given that these studies have been performed with significantly higher S/N and resolution, they are useful indicators to assess our abundance zero points, if we assume that first the age-abundance relations they found apply to our selection (typically further away than their sample) and secondly our age estimates agree on average with theirs. For the comparisons in this section, we do not use the stellar ages estimated as part of the VAC, but the ones calculated on-the-fly by the spectroscopic analysis pipeline. For the comparison in Fig. 15, we shift the age scale by the difference of our Solar age and the 1.26 Gyr lower one reported by Bonanno, Schlattl & Paternò (2002). We plot the age-abundances distribution of the Solar twins from GALAH+ DR3 in Fig. 15 together with the fitted relations from Bedell et al. (2018) and state the mean difference between these curves and our data for each panel. We see good agreement in the plots for O, Na, Si, Ca, Sc, Ti, Ti II, Mn, Zn, Y, and Ba, thus confirming our abundance zero points. We see some smaller differences for Mg, Cr, Ni, Cu. For Ni and Cu, the difference is still well within the uncertainties. We are unsure of the origin of the larger differences for Mg and Cr; especially since our other zero-point comparisons (Table A2) show agreement to better than 0.05 dex. Systematic offsets could, however, be introduced by the different line selections and information (for Mg and Cr for example, only one line is in common between each analysis). For C and V the data are inconclusive.

5.1.4 Abundances of the cluster stars

Similar to GALAH DR2, we could assess the element abundances for selected clusters with numerous observed members. These are, however, not useful in a straightforward manner to estimate the accuracy and precision of our measurements, due to internal processes like atomic diffusion and dredge-up changing the observed photospheric abundances for different evolutionary stages for open clusters (see e.g. Bertelli Motta et al. 2018; Gao et al. 2018; Souto et al. 2018, 2019) as well as the presence of multiple populations in

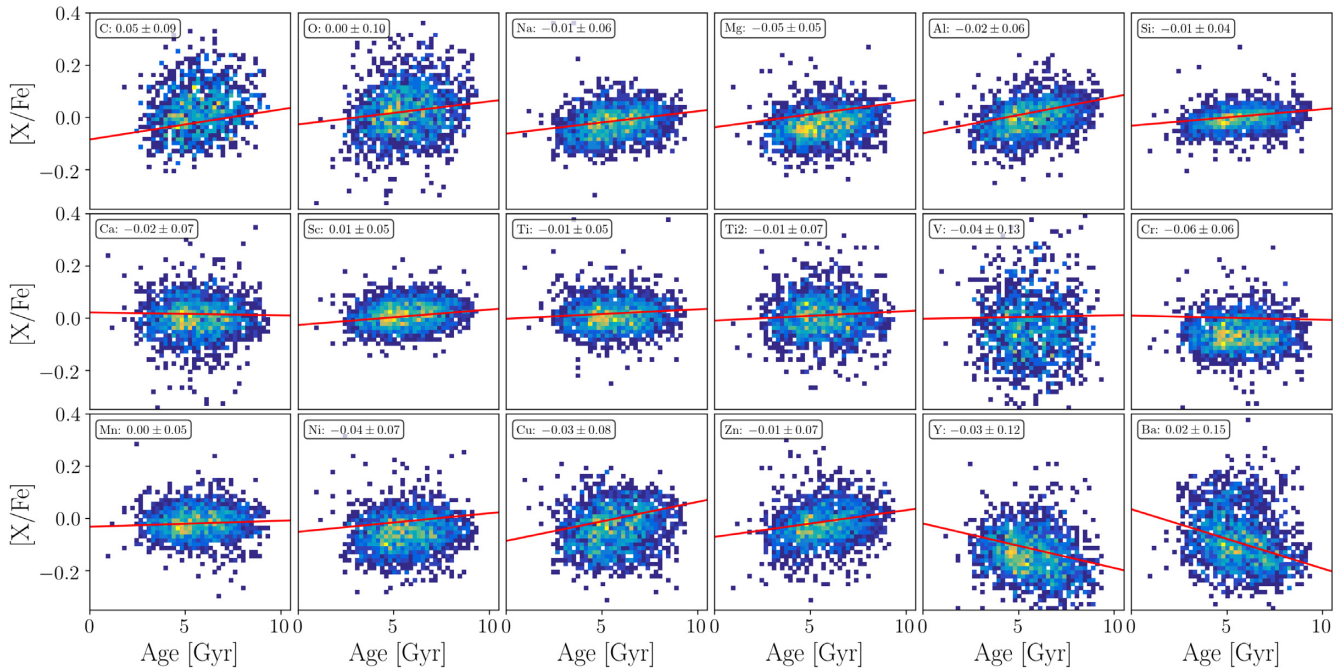


Figure 15. Chemical abundances $[X/Fe]$ of solar twin stars as a function of on-the-fly computed stellar age. Ages are shifted by -1.26 Gyr. We note that this age is different from the one reported in the VAC on stellar ages. We overplot in red the functions calculated by Spina et al. (2016) and Bedell et al. (2018).

several globular clusters, leading to the spread in metallicities (see e.g. Carretta et al. 2009b) and anticorrelations in several elements, like Na–O or Mg–Al (see e.g. Carretta et al. 2009a; D’Orazi et al. 2010).

Since we lack good calibrators for these abundances, we choose to include overviews of several abundances for open clusters, as we expect the evolutionary effect within these to be seen, but predictable. Significant differences in abundances above the expected evolutionary effects are therefore indicative of systematic trends within our analysis. A more detailed analysis of abundances and trends in open and globular clusters will be performed in the studies by Spina et al. (2021) and D. M. Nataf et al. (in preparation), respectively, but we make the overview plots available in our online documentation. For the vast majority, our trends agree with the literature values, change such as the OCCAM survey (Donor et al. 2020), as shown in Fig. 16, where we plot the abundances of Si, Cr, Cu, and Ba for a selection of open clusters.

Some of the differences that we find between dwarfs and giants in two of the open clusters with many members, namely M 67 (NGC 2682) and Ruprecht 147, are however significantly higher than would be expected from such evolutionary effects. We list the 16/50/84th percentiles for both clusters separated into dwarfs ($T_{\text{eff}} \geq 5500$ K or $\log g \geq 3.5$ dex) and giants ($T_{\text{eff}} < 5500$ K and $\log g < 3.5$ dex) in Table 6. While for M 67 the agreement seems quite good for most elements in view of the average precision uncertainties, we find significant differences between dwarfs and giants for Al, Ni, Zn, Ba, and La for both clusters. We also find significant differences in at least one cluster for O, Na, Si, Ti II, V, Zr, Ce, Nd, and Sm. We will elaborate more on these findings in Section 6.5, where we describe caveats of abundances for Solar and metal-rich giants, especially for the elements Al, Ti II, Ni, and Ba, which seem to show in general elevated values for Solar and metal-rich giants.

5.1.5 Element abundances of wide binaries

We use wide binaries from GALAH, selected using the algorithms presented in El-Badry & Rix (2018), for the validation of our elemental abundances, in the same way as described earlier for $[Fe/H]$. We plot the difference in element abundances of the two components for different nucleosynthesis channels in Fig. 17. For this comparison, we limit ourselves to those stars with similar $[Fe/H]$ (within 0.25 dex) and similar v_{rad} (within 1 km s^{-1}), and no raised stellar parameter flags. The average differences of these stars, which are believed to (on average) share very similar composition, are typically small as a function of $[Fe/H]$, T_{eff} , and $\log g$, as shown in the left-hand, middle, and right-hand panels for the α -enhancement, O, Na, Si, Mn, and Ba, confirming that our analysis works rather well for stars with similar astrometric information.

For completeness, we list the average differences of all analysed elements in Table 7 together with their average quoted uncertainties from GALAH+ DR3. If our assumptions of equal chemical compositions among the binary stars are correct, one would expect no bias between their measured element abundances and a scatter corresponding to the measurements uncertainty. For many of these elements, we see an overall small average difference between the binary components among the elements for which we had enough abundance estimates of both components. Only for O, V, Zr, La, Ce, and Sm we see a disagreement above 0.05 dex. For these elements, however, we note that the scatter is larger compared to the other elements suggesting less precise measurements. This is confirmed by the larger precision uncertainties, confirming that our precision estimates are reliable, although not always to scale. While the scatter of the binary differences and the average reported uncertainties agree roughly for most elements, they differ significantly for Li, O, Ti II, V, La, Ce, and Sm, suggesting that our uncertainties due to precision are underestimated for these particular elements or accuracy uncertainties play an important role, which is

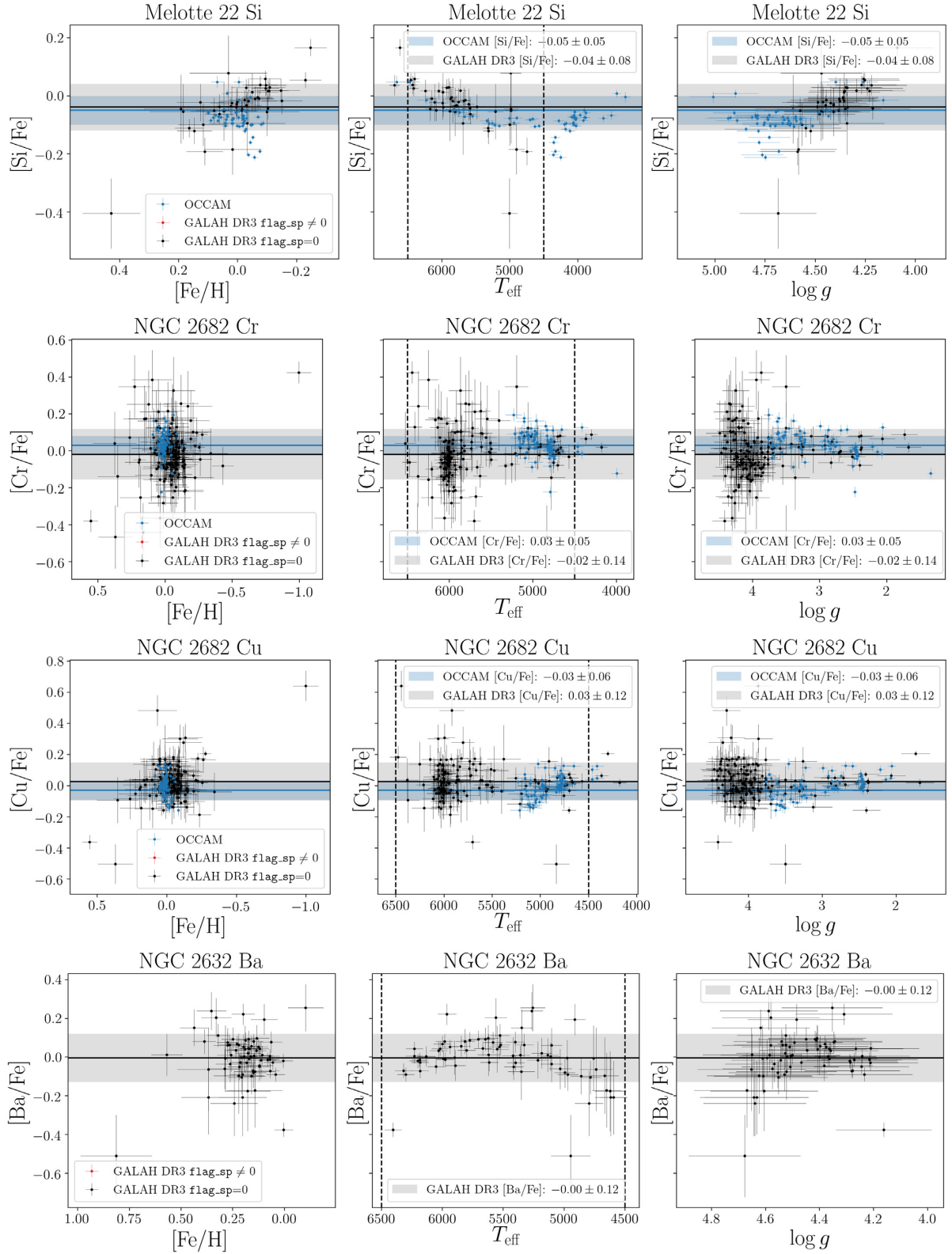


Figure 16. Element abundances $[X/Fe]$ as a function of stellar parameters $[Fe/H]$, T_{eff} , and $\log g$ for a selection of elements X from the four clusters with information from both GALAH+ DR3 (unflagged in black, flagged in red) and the OCCAM survey (unflagged data, blue Donor et al. 2020) in Fig. 11. Horizontal bars indicate the mean abundances of the clusters from GALAH in grey (estimated from unflagged measurements for stars with $4500 < T_{\text{eff}} < 6500$ K) and the OCCAM survey (blue).

Table 6. Comparison of GALAH DR3 element abundances of dwarfs and giants in M67 and Ruprecht 147. Values are only listed if more than five pairs with unflagged [X/Fe] were available.

Elem.	M67		Ruprecht 147	
	Dwarfs	Giants	Dwarfs	Giants
[Fe/H]	$-0.05^{+0.11}_{-0.08}$	$-0.05^{+0.06}_{-0.09}$	$0.04^{+0.07}_{-0.07}$	$0.01^{+0.08}_{-0.04}$
[α /Fe]	$0.01^{+0.07}_{-0.05}$	$0.01^{+0.04}_{-0.05}$	$-0.01^{+0.03}_{-0.03}$	$0.02^{+0.02}_{-0.05}$
[Li/Fe]	$1.38^{+0.21}_{-0.28}$	–	$1.26^{+0.22}_{-0.27}$	–
[C/Fe]	$0.06^{+0.11}_{-0.13}$	–	$-0.00^{+0.12}_{-0.09}$	–
[O/Fe]	$0.05^{+0.14}_{-0.15}$	$0.12^{+0.14}_{-0.14}$	$-0.00^{+0.15}_{-0.10}$	$0.19^{+0.05}_{-0.17}$
[Na/Fe]	$0.06^{+0.07}_{-0.11}$	$0.06^{+0.12}_{-0.13}$	$0.09^{+0.05}_{-0.05}$	$0.17^{+0.05}_{-0.05}$
[Mg/Fe]	$-0.02^{+0.10}_{-0.08}$	$-0.05^{+0.12}_{-0.02}$	$-0.04^{+0.04}_{-0.04}$	$-0.02^{+0.03}_{-0.04}$
[Al/Fe]	$0.01^{+0.10}_{-0.11}$	$0.17^{+0.05}_{-0.07}$	$-0.00^{+0.06}_{-0.03}$	$0.19^{+0.01}_{-0.03}$
[Si/Fe]	$-0.00^{+0.07}_{-0.06}$	$0.21^{+0.18}_{-0.19}$	$-0.01^{+0.03}_{-0.03}$	$0.07^{+0.02}_{-0.08}$
[K/Fe]	$-0.01^{+0.14}_{-0.11}$	$-0.00^{+0.14}_{-0.14}$	$0.02^{+0.04}_{-0.07}$	$-0.07^{+0.04}_{-0.07}$
[Ca/Fe]	$0.05^{+0.09}_{-0.08}$	$0.04^{+0.10}_{-0.09}$	$0.08^{+0.06}_{-0.06}$	$0.14^{+0.01}_{-0.06}$
[Sc/Fe]	$0.04^{+0.06}_{-0.07}$	$-0.02^{+0.05}_{-0.06}$	$0.07^{+0.05}_{-0.08}$	$-0.04^{+0.02}_{-0.01}$
[Ti/Fe]	$0.04^{+0.12}_{-0.08}$	$-0.01^{+0.04}_{-0.04}$	$-0.01^{+0.05}_{-0.04}$	$-0.00^{+0.01}_{-0.03}$
[Ti2/Fe]	$0.02^{+0.12}_{-0.10}$	$0.05^{+0.06}_{-0.06}$	$-0.02^{+0.07}_{-0.08}$	$0.15^{+0.03}_{-0.03}$
[V/Fe]	$0.05^{+0.24}_{-0.17}$	$0.17^{+0.22}_{-0.11}$	$-0.06^{+0.19}_{-0.10}$	–
[Cr/Fe]	$-0.03^{+0.14}_{-0.10}$	$0.02^{+0.06}_{-0.05}$	$-0.08^{+0.08}_{-0.03}$	$0.00^{+0.02}_{-0.02}$
[Mn/Fe]	$0.00^{+0.09}_{-0.07}$	$0.05^{+0.09}_{-0.08}$	$0.01^{+0.04}_{-0.03}$	$0.06^{+0.03}_{-0.07}$
[Ni/Fe]	$0.01^{+0.12}_{-0.10}$	$0.09^{+0.06}_{-0.07}$	$-0.08^{+0.07}_{-0.04}$	$0.10^{+0.02}_{-0.06}$
[Cu/Fe]	$0.02^{+0.11}_{-0.08}$	$0.02^{+0.04}_{-0.05}$	$0.03^{+0.03}_{-0.08}$	$0.01^{+0.04}_{-0.03}$
[Zn/Fe]	$0.06^{+0.13}_{-0.11}$	$-0.11^{+0.12}_{-0.12}$	$0.03^{+0.06}_{-0.06}$	$-0.15^{+0.03}_{-0.07}$
[Rb/Fe]	–	–	–	–
[Sr/Fe]	–	–	–	–
[Y/Fe]	$0.01^{+0.14}_{-0.15}$	$0.01^{+0.25}_{-0.20}$	$0.07^{+0.06}_{-0.16}$	$0.09^{+0.03}_{-0.04}$
[Zr/Fe]	$0.73^{+0.66}_{-0.51}$	$-0.02^{+0.08}_{-0.07}$	–	$-0.02^{+0.04}_{-0.09}$
[Mo/Fe]	–	–	–	–
[Ru/Fe]	–	$0.17^{+0.60}_{-0.09}$	–	–
[Ba/Fe]	$0.03^{+0.10}_{-0.15}$	$0.17^{+0.14}_{-0.15}$	$0.05^{+0.10}_{-0.14}$	$0.35^{+0.05}_{-0.07}$
[La/Fe]	$0.47^{+0.37}_{-0.30}$	$-0.02^{+0.13}_{-0.09}$	$0.22^{+0.34}_{-0.07}$	$-0.08^{+0.05}_{-0.02}$
[Ce/Fe]	$0.14^{+0.44}_{-0.25}$	$-0.07^{+0.13}_{-0.09}$	$-0.04^{+0.10}_{-0.16}$	$-0.05^{+0.05}_{-0.03}$
[Nd/Fe]	$0.46^{+0.45}_{-0.17}$	$0.16^{+0.14}_{-0.09}$	–	$0.10^{+0.05}_{-0.05}$
[Sm/Fe]	$0.37^{+0.62}_{-0.31}$	$-0.20^{+0.57}_{-0.13}$	–	–
[Eu/Fe]	–	$-0.01^{+0.09}_{-0.08}$	–	–

neglected in our analysis. We can also not exclude the possibility that there are actual differences in the abundances of the wide binaries, which is expected at least for Li for binary components at different T_{eff} .

5.2 Precision of element abundances

We assess the precision of our element abundances by comparing the internal SME covariance uncertainties with those from repeat observations of the same star in Fig. 18. In contrast with the case for the stellar parameter estimation, we see that the covariance errors from the individual line measurements are typically in good agreement for almost all lines. The standard deviations of the measurements are also consistent irrespective of the fibre combination.

We note, however, that our final estimates of the internal SME-based uncertainties are lower than those from the repeat observations, when a large number of lines is fitted in combination rather than line-by-line, in particular Fe, which we discussed in Section 4.2.

Table 7. Comparison of element abundances of wide binaries in GALAH DR3. Values are only listed if more than five pairs with unflagged [X/Fe] were available.

Elem.	16/50/84th perc.	Avg. e_x_fe
α	$-0.00^{+0.06}_{-0.06}$	0.04
Li	$-0.10^{+0.27}_{-0.04}$	0.08
C	$0.00^{+0.09}_{-0.11}$	0.10
O	$-0.02^{+0.20}_{-0.29}$	0.13
Na	$0.00^{+0.07}_{-0.09}$	0.06
Mg	$0.03^{+0.08}_{-0.11}$	0.09
Al	$-0.01^{+0.08}_{-0.08}$	0.07
Si	$-0.00^{+0.08}_{-0.06}$	0.06
K	$-0.03^{+0.12}_{-0.12}$	0.09
Ca	$-0.01^{+0.09}_{-0.09}$	0.08
Sc	$0.02^{+0.07}_{-0.09}$	0.06
Ti	$0.00^{+0.08}_{-0.08}$	0.08
Ti2	$0.02^{+0.13}_{-0.14}$	0.08
V	$-0.05^{+0.23}_{-0.22}$	0.11
Cr	$0.01^{+0.07}_{-0.08}$	0.08
Mn	$0.02^{+0.08}_{-0.09}$	0.09
Ni	$-0.01^{+0.10}_{-0.10}$	0.08
Cu	$0.01^{+0.07}_{-0.08}$	0.06
Zn	$0.00^{+0.13}_{-0.11}$	0.11
Rb	–	–
Sr	–	–
Y	$0.03^{+0.20}_{-0.19}$	0.15
Zr	$0.10^{+0.13}_{-0.15}$	0.10
Mo	–	–
Ru	–	–
Ba	$0.01^{+0.10}_{-0.12}$	0.09
La	$-0.04^{+0.33}_{-0.27}$	0.11
Ce	$-0.11^{+0.22}_{-0.10}$	0.11
Nd	–	–
Sm	$-0.19^{+0.18}_{-0.16}$	0.13
Eu	–	–

This suggests that either the SME-internal method has problems in estimating realistic errors when many pixels are involved, or that our spectrum quality indicator (`snr_c2.iraf`) is not representative in those cases. With the exception of Fe, we have however managed to estimate abundances of elements with many lines in a line-by-line manner, such that the fitting and repeat uncertainty show a similar behaviour. Unlike for the case of the stellar parameter estimation, we only report the final abundance uncertainty based on the maximum of the raw internal covariance error for the abundance fit and the S/N -scaled repeat observation uncertainty.

5.3 Flagging of element abundances

As for all of our previous GALAH releases, we want to stress that we discourage the use of flagged element abundances without consideration of the possible systematic trends that these probably less reliable measurements can introduce. However, setting flags for element abundance measurements is extremely difficult and will never be perfect. In this section, we lay out which flags we have implemented. We also point to identified possible caveats, where no flags are raised, but caution should be applied.

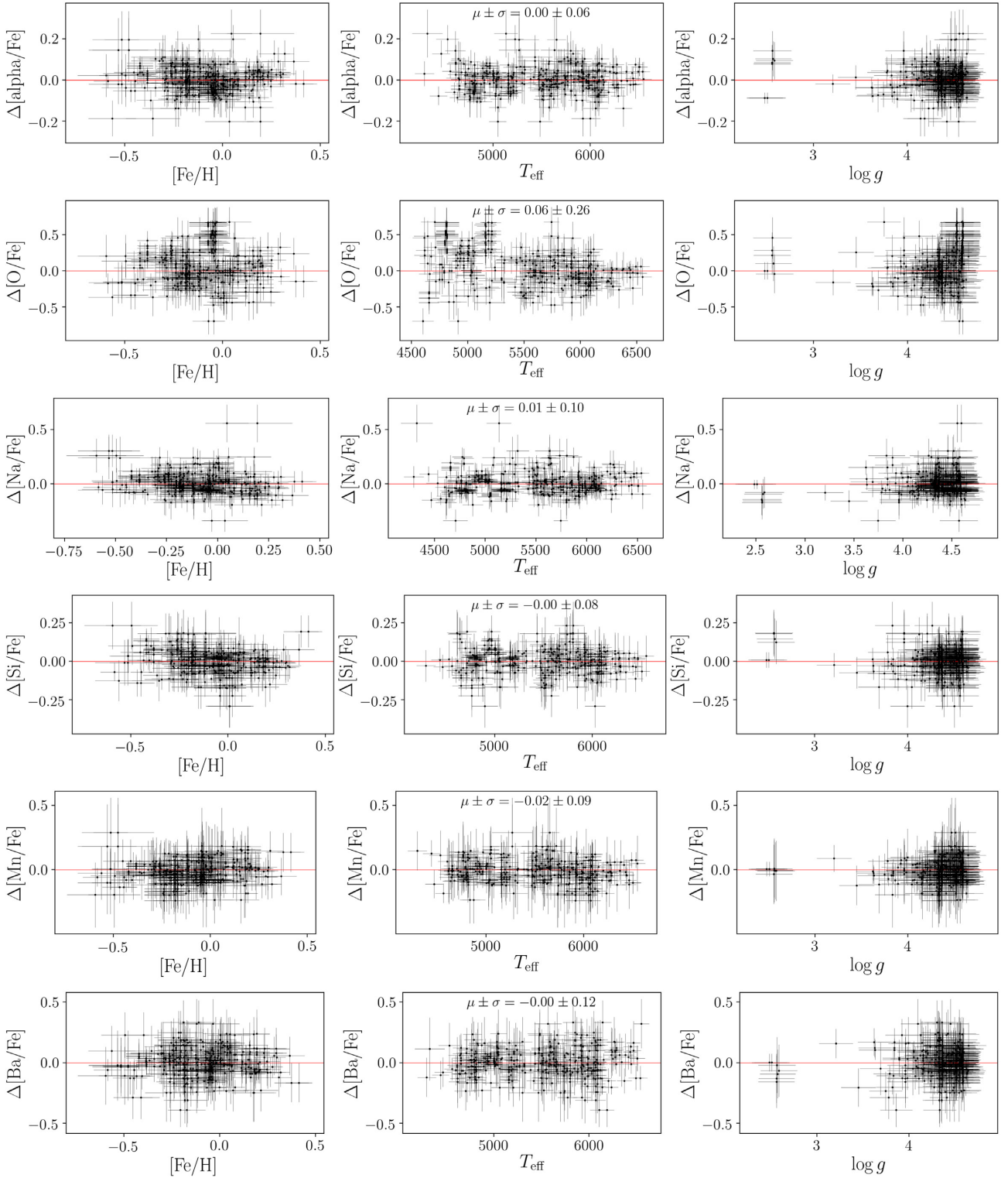


Figure 17. Comparison of unflagged element abundances for wide binaries for the selected elements alpha, O, Na, Si, Mn, and Ba. Pairs were identified with the algorithm by El-Badry & Rix (2018).

The major abundance flags are reported as `flag_X_fe` for each element X and are listed in Table 4. For the final element abundances, we only report measurements that have passed all our quality checks with no flag raised or are an upper limit (with flag 1, see our description of upper limits in Section 3.3). For ease of use we have

raised a flag value 32 if the measurement is not reported, because it did not pass the quality checks.

For each individual abundance measurement (`ind_X1234_fe` for line/combined measurements X1234), we have run a series of quality checks, which are summarized in the `ind_flag_X1234` as listed in

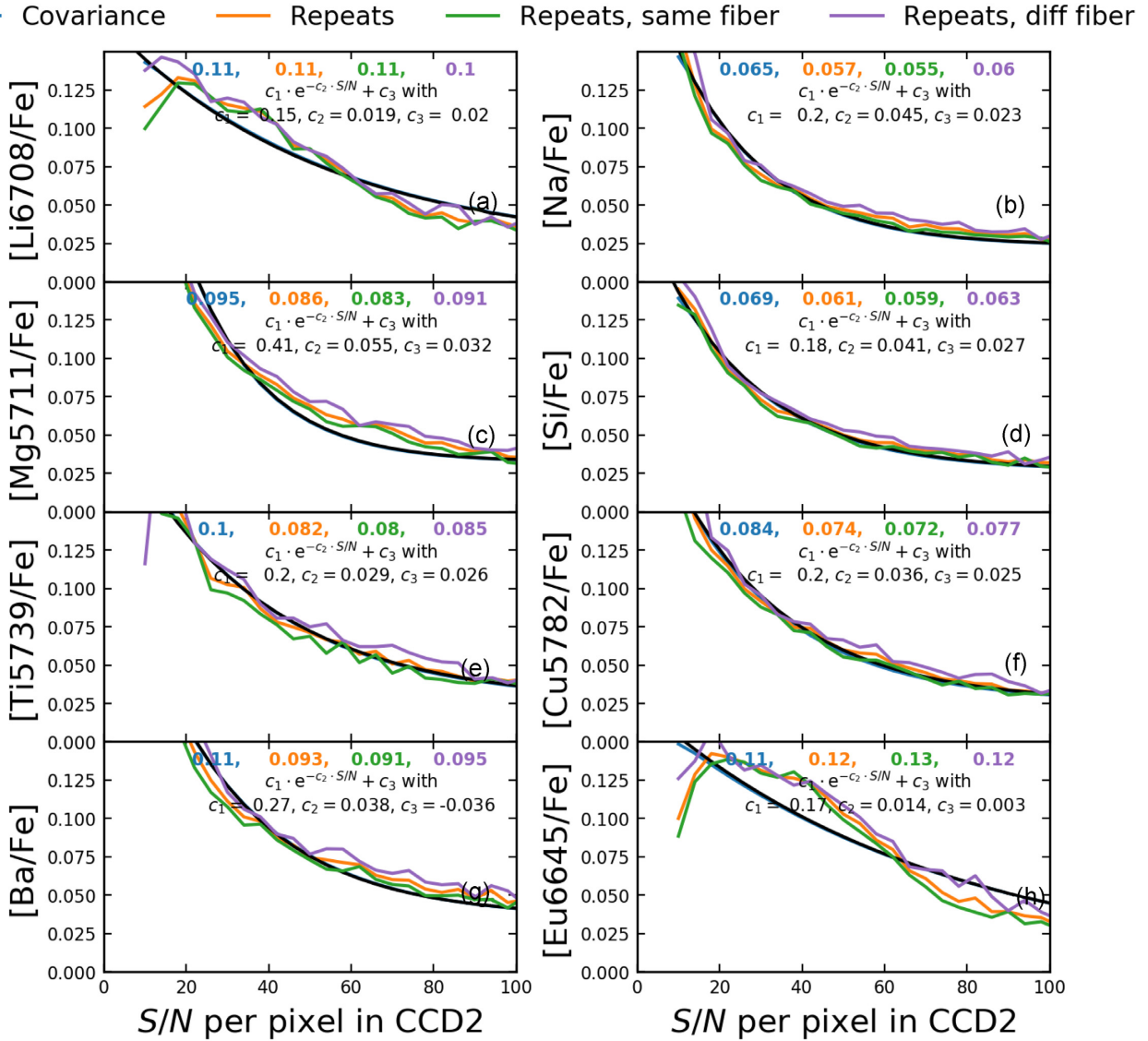


Figure 18. Standard deviation of element abundances for eight different elements/lines in different bins of S/N (snr.c2.iraf). Shown are the mean (internal) covariance fit uncertainties from SME (blue), as well as the standard deviations for repeat observations of the same star for all fibre-combinations (orange), same fibre combination (green), and different fibre combinations (purple). An exponential function (black) was fitted to all (orange) repeats was performed. Number in the top state the expected or mean uncertainty at $\text{snr.c2.iraf} = 40$.

Table 4. These include a check of the χ^2 values (value 2), where we raise a warning, if the χ^2 value is above a very high S/N -depending threshold (estimated to be around 16 for $S/N = 10$, 20 for $S/N = 35$, and 160 for $S/N = 100$ from the general χ^2 - S/N trend for the elements, compared to the typical median χ^2 value of 0.5 to 1.0 at $S/N = 35$). A warning flag 4 for an imprecise or likely saturated measurement was raised, if the fitting uncertainty was above 0.3 dex or twice the expected uncertainty from repeat observations. We raise a flag value 8, if the wavelength solution around the Li line at 6708 Å is questionable, that is, when our Li fits with and without an additional v_{rad} fit just at this particular spectrum region result in a difference above 10 km s^{-1} . We report individual measurements, but raise a flag 16, if we do not trust the stellar parameters ($\text{flag_sp} \geq 128$). Flag value 32 is raised, if the measurement was not successful, that is if no stellar parameters were available or the line was too shallow or too blended.

As we elaborate in the next section, we have identified several possible caveats, for which we have not implemented an algorithm to raise a flag, either because we could not find a way to automatically identify the caveats, or we are unsure if the measurements should be flagged. For the abundances, we therefore advice to carefully consider the caveats described in Sections 6.4 and 6.5 in particular.

6 POSSIBLE CAVEATS: ANALYSIS SHORTCOMING OR PHYSICAL CORRELATION?

In the previous sections, we have laid out the methods by which we flag unphysical results and spectra with peculiarities for which our pipeline is likely to underperform. However, we cannot visually inspect all of the more than 30 million measurements that have been performed for this data release. Furthermore, we aim to not follow

up all of the possible correlations in full detail, because many of these pose problems to understand the possible astrophysical nature of these trends (as shown later in Section 6.3 for atomic diffusion causing systematic differences of surface abundances in open cluster stars). Instead, we choose to leave such efforts for future scientific follow-up.

In this section, we address several possible caveats, for which we either have not yet found or implemented a solution, or believe that these results could indeed be of an astrophysical nature. We give examples for peculiar abundance patterns and show an example where the pattern (of Am/Fm stars) is truly representing the observed surface abundances when assuming ionization equilibrium. In other cases, especially for the most metal-rich as well as coolest giant stars, we are aware that our pipeline is likely introducing systematic trends that may be ascribed first to our use of standard 1D hydrostatic model atmospheres (although the effect is partly mitigated by fudge parameters that can be tuned to mimic the effects of convection), secondly to our partly unreliable or incomplete molecular line data, and thirdly to the lack of true continuum points to use for the spectrum normalization in these stars. In the latter case, the pseudo-continuum placement can correlate strongly with the stellar parameters (especially [Fe/H]) and lead to systematic trends in the reported measurements. We address possible influences on the reliability of surface gravities and finally also lay out considerations of the uncertainties and describe how these will be improved in future data releases.

6.1 Abundance differences with SME version

SME is an actively developed software with regular improvements and bug fixes as part of version publications. For GALAH DR3, we used SME version 536. This particular version has recently been found to have a code inconsistency which may cause non-trivial changes in synthetic fluxes and abundances (A. Gavel and A. J. Korn, private communication) with our used synthesis library *linux.x86_64.64g*. It is unlikely that this bug significantly influences our results thanks to a cancellation effect in our abundance zero-point calibration. We have performed several tests with the more recent SME version 580 on a large sample of roughly 20 000 stars, including reference stars such as the GBS, the stars with asteroseismic data, and open/globular cluster stars. For the majority of stars, we find that effects on abundances will be essentially null. This is because the bug appears to introduce a bias in abundances for all stars, which cancels in our calculation of solar-relative abundances. In practice, these effects are on the order of 0.05 dex for dwarfs and giants. Less than 10 per cent of the latter stars with very low surface gravity exhibit complex effects with biases as large as 0.15 dex. We have unfortunately not found a predictable systematic trend with stellar parameters, that would have allowed us to correct all abundance measurements. We want to stress though that our accuracy and precision estimates point towards SME 536 delivering reliable results after the zero-point correction. In the future, we will implement newer versions of SME.

6.2 Stacked spectra

In this data release, for the first time we also include stacked spectra of repeat observations. We select the higher *S/N* observations for the main catalogue, but also report the individual spectra in the extended catalogue. We identify observations of the same star via matching coordinates. However, we have found few cases, where calibration observations were performed already with configurations of stellar observations, such as bias frames, sky, or dome flats. In few cases, the observations were not marked as calibration frames clearly, and have

been used for the stacking of stellar spectra. We therefore caution the use of metal-poor stacked spectra, which can be identified in the 11th digit of the `subject_id` being 2 instead of 1, for example 160522002102FFF, where some of the science observations 0023-0025 have been stacked with dome flat observations 0016-0018, causing underestimated [Fe/H], which cannot be picked up by the pipeline, because the analysis is reasonable for the wrongly stacked spectra. By comparison the differences of [Fe/H], v_{rad} , and T_{eff} for stacked and unstacked spectra, we find less than 800 observations²⁰ being potentially wrongly stacked – 753 with `flag_sp` > 256.

6.3 Radial velocities in table version 1

In the main tables with the suffix `v1`, we report the radial velocities as estimated with the reduced spectra, which already applied barycentric corrections. Right before this data release, we have identified a wrong implementation of barycentric corrections was used and the reported radial velocities as part of the main tables were shifted incorrectly (within less than 0.4 km s^{-1}).

In our updated table versions with suffix `v2`, we have corrected these incorrect estimates and provide correct measurements from SME in the VAC on v_{rad} with the columns `rv_sme_v2` together with the old, incorrect estimates under `rv_sme_v1`. Based on feedback from the scientific community, we have further exchanged the entries in the main catalogues for `rv_galah` and `e_rv_galah` by even more reliable measurements of `rv_obst` (when available) as outlined in Section 7.3.4 and provide a flag `use_rv_flag` in the VAC on v_{rad} to outline where the used values stem from.

6.4 Possible systematic trends

Below we present a list of possible systematic trends, as found up until the publication of GALAH+ DR3 during the validation. These do not appear in particular order.

6.4.1 High abundances of V, Co, Rb, Sr, Zr, Mo, Ru, La, Nd, and Sm

In this data release, we try to push the boundary of what can be extracted from the observed spectra with the aim to deliver as many abundance measurements as possible. This does, however, not only push the limits of deciding what measurement is reliable, that is, significantly different from a continuum measurement, but leads to complicated cases where lines are blended, leading to possible wrong systematics. We therefore especially caution the use of elevated abundance measurements (especially above [X/Fe] of 0.3 dex, as indicated in Fig. 21) for V, Co, Rb, Sr, Zr, Mo, Ru, La, Nd, and Sm, as we suspect that these are most likely affected by blending issues close to the detection limit. Only visual inspection could however confirm this, which is not possible for the vast number of measurements at hand and we therefore advise the user to inspect the published spectra before using these measurements blindly.

For V, we caution the use of measurements with `nr_v_fe` 2 and 3, that is, using VI 4832. For Co, we caution the use of measurements with `nr_co_fe` = 2 or 8, that is, measurements purely based on lines Co I 6490 and 7713. While we have not been able to narrow down the

²⁰More than 50 stacking issues per field were found for 1412310030, 1501010025, 1501030027, 1501030030, 1501080015, 1501120025, 1605220021, and 1710310021. 94 per cent of the spectra were already flagged. Further not all spectra of these fields wrongly stacked. We thus do not to flag all of them a priori.

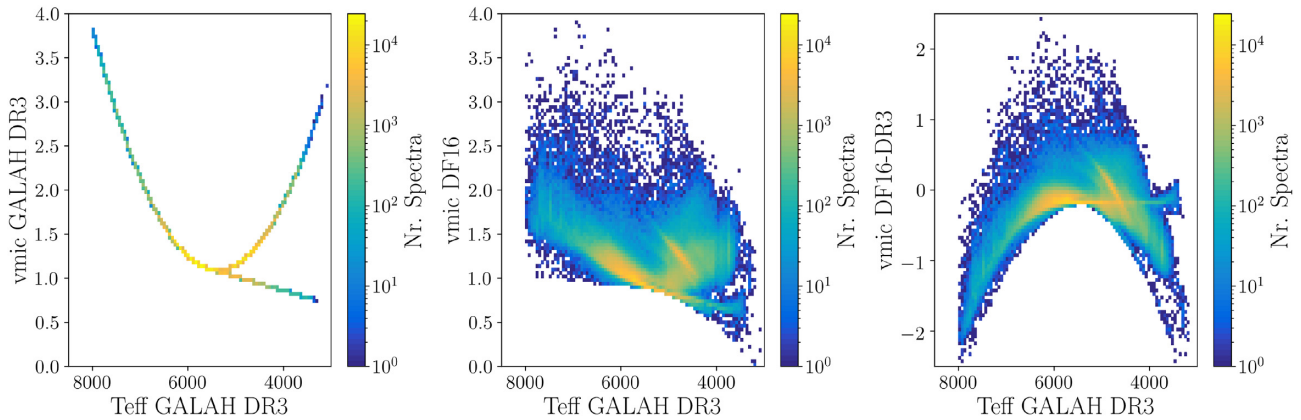


Figure 19. Comparison of v_{mic} calculated via relations used for GALAH+ DR3 and Dutra-Ferreira et al. (2016). Relations of v_{mic} as a function of T_{eff} calculated via relations used for GALAH+ DR3 and Dutra-Ferreira et al. (2016) in the left-hand and middle panels, respectively. A comparison of the two v_{mic} values as a function of T_{eff} is plotted in the right-hand panel and shows good agreement for the majority of stars, i.e. cool and warm dwarfs and stars around the RC. However, the two relations disagree strongly for the most luminous and hottest stars. For the latter, GALAH+ DR3 v_{mic} values are up to two times higher. We note that the relation by Dutra-Ferreira et al. (2016) is based on 3D models with $4500 \leq T_{\text{eff}} \leq 6500$ K and $2.5 \leq \log g \leq 4.5$ dex for strictly Solar [Fe/H].

exact cause, we assume that measurements only based on these lines are caused by imperfect telluric corrections in CCD 3 for Co I 6490 and spikes or imperfect telluric corrections in CCD4 for Co I 7713. Such reduction issues introduce strong emission and absorption lines, which will either weaken the line beyond detectability or strengthen it so that only high V or Co abundances can reproduce the observation. However, the resultant fits and their χ^2 values will not appear suspicious and such reduction issues are therefore hard to identify and flag automatically.

6.4.2 1D LTE / 1D non-LTE and microturbulence

Our spectrum synthesis is performed by assuming 1D LTE and 1D non-LTE. However, modelling stellar atmospheres with a 1D description is neglecting 3D, time-dependent effects, which can only partially be mitigated by fudge factors, like v_{mic} . While allowing this factor to be fitted as part of the analysis, our tests have shown that the abundance precision decreases. We have therefore implemented an empirical relation, estimated by Gao et al. (2018) for GALAH, over the whole parameter space, as outlined in Section 3.3, as shown in panel (a) of Fig. 19.

During the validation of element abundances, we have discovered several temperature-dependent trends. These occur in regions where our analysis approach is prone to systematic trends anyway, that is, the coolest/most line-rich (< 4500 K) and hottest/most line-poor (> 6500 K) regions. We cannot exclude that the found systematic trends can also be partially caused by over- or underestimated v_{mic} (in addition to a systematically incorrect normalization for the most line-rich spectra). Comparisons with other v_{mic} relations, see e.g. the relations by Dutra-Ferreira et al. (2016) based on 3D atmosphere calculations (see panel b) suggest large deviations for certain stars, leading to a difference of up to 2 km s^{-1} (see panel c). The tests by Jofré et al. (2017) also showed that different stellar types are affected differently by inaccurate v_{mic} , with strongest implications for (more metal-rich) giant stars among the analysed sample of GBS.

While our long-term goal is to implement 3D non-LTE calculations, we believe that it is worth testing the implementation of v_{mic} as a free parameter or the relations estimated by Dutra-Ferreira et al. (2016) for certain parts of the parameter space, if the advantages

outweigh the loss in abundance precision. Using v_{mic} as a free parameter showed for example significant improvements of trends with T_{eff} for the APOGEE survey (Holtzman et al. 2018).

6.4.3 Consistency of atmosphere composition for spectrum synthesis

For computational reasons, we estimate the abundances of all elements independently, and assume scaled-Solar patterns for most other elements during that optimization. However, our approach might introduce systematic trend for elements which are often correlated (e.g. C and O), surrounded by lines that are deviating from the scaled-Solar pattern, or when the abundance pattern in general differs from the scaled-Solar pattern, thus leading to differences in the continuum and molecular lines strengths. If computationally possible, it would therefore be preferable to fit all elements partially (Brewer et al. 2016) or fully self-consistent (Ting et al. 2019), which could also allow us to estimate abundances not only via atomic lines, but also molecular features, which follow molecular equilibria (Ting et al. 2018).

6.4.4 Metallicity/abundance trends

For numerous open and globular clusters, we have found trends of [Fe/H] with temperature and/or evolutionary stage at the coolest and hottest ends of the T_{eff} range or in general for young clusters.

Stellar clusters are not the main focus of our survey, and many of the observations that were performed for them are outside of the typical GALAH magnitude, distance, and age range. Most of the open and globular clusters targeted by our observations are much more distant, which leads to less reliable distance estimates, with implications for our distance-dependent $\log g$ estimates of their stars. Many of stars in the open clusters stars are typically younger than the GALAH targets, with astrophysical implications on additional features in their spectra.

Baratella et al. (2020) found that v_{mic} is overestimated and thus [Fe/H] is underestimated when using Fe lines in clusters, a trend that we also observe in some of our cluster observations. We therefore cannot a priori exclude wrong v_{mic} values as the influence of cluster abundance trends (see comments on v_{mic} above).

We note, however, that for open clusters, differences in [Fe/H] as well as other abundances have been found to be of astrophysical nature, e.g. atomic diffusion (e.g. Bertelli Motta et al. 2018; Gao et al. 2018; Souto et al. 2018, 2019; Liu et al. 2019; Semanova et al. 2020) or stellar activity (e.g. Spina et al. 2020). Furthermore, astrophysical abundance trends, like anticorrelations of light elements (see Bastian & Lardo 2018, and references therein), have also been found in globular clusters and are partially hard to disentangle from other abundance trends, e.g. those introduced by our analysis pipeline. We will follow this up for globular clusters with a dedicated study (D. M. Nataf et al., in preparation).

6.4.5 Binarity

A central assumption of our observations is that each fibre observes only one star. We try to ensure this by only selecting point sources from 2MASS with a sufficient separation from other bright neighbours. Our selection does however not exclude stars that are not extended within 2MASS, for example spectroscopic binaries.

Our means to identify (spectroscopic) binaries are, however, limited, because as part of GALAH we usually only take three spectra within typically 1 h per star, and can only resolve spectroscopic binaries if the lines of both components are resolved with the given broadening induced by our instrument and stellar rotation. Although we try to identify and flag stars as part of our validation (see Section 4.3), we expect that we are not able to identify a significant fraction of stars as binaries. Price-Whelan et al. (2020) find 19 635 high confidence close-binaries among 232 495 APOGEE sources (8 per cent), and El-Badry et al. (2018b) find that for 2645 of 20 142 analysed main sequence targets (13 per cent), more than one star contributes significantly to the spectrum. Based on the results of Price-Whelan et al. (2020) we would expect at least 10 per cent of the stars above > 6000 K (23 per cent of GALAH+ DR3) and more than 40 per cent of stars with > 7000 K (3 per cent of GALAH+ DR3) to be binaries.

The implications of not identifying a star as a binary can be manifold. First the binarity changes the astrometric solution, which is not always identified via *Gaia* warnings or quality values like the RUWE value. This can falsify the estimated distance of objects. Secondly, the photometry of a binary system can deviate significantly from that of the primary component, depending on the flux contribution of the secondary. Thirdly, the flux contribution within the spectrum lead to inaccurate fits when assuming a single star as quantified by El-Badry et al. (2018a, b), which leads to inaccurate stellar parameters as well as element abundances. For binaries, the measured v_{rad} also only reflects (at best) the value at the time of observation and is thus not indicative of its Galactic orbit. We note that we have not made use of the assessment of v_{rad} changes among our 51 539 spectra with dedicated repeat observations (typically on different nights).

6.4.6 Stars with uncertain/unreliable astrometry

As part of our spectroscopic analysis, we rely on the quality of astrometric measurements, to infer reliable absolute photometry and then $\log g$. While we flag stars with high RUWE values above 1.4 (Lindgren 2018; Lindgren et al. 2018), we caution the user to not blindly use all measurements, especially those of stars with uncertain astrometry.

We have used more elaborate distance estimates from Bailer-Jones et al. (2018) which infer more trustworthy distances based on a Galactic prior for stars with parallax uncertainties beyond 20 per cent. Especially for very distant stars, like some of our observations of LMC stars, this Galactic prior leads to an underestimated distance and thus likely overestimated $\log g$ (see equations 1 and 2).

In general, we note that for stars with more constrained distance estimates, like open clusters (Cantat-Gaudin & Anders 2020), globular clusters (Baumgardt et al. 2019) and stars of the LMC (de Grijs, Wicker & Bono 2014), a reanalysis would be leading to more reliable stellar parameters and abundances, when using these distances instead of the ones solely estimated from *Gaia* parallaxes.

6.4.7 Influences of isochrone choice

For computational reasons we have limited the isochrones used for the on-the-fly mass estimation to a grid of 0.5..(0.5)..13.5 Gyr. We note that for the youngest stars this might not be a good choice, as we see some nodding in the on-the-fly mass and age estimates, especially for hot stars and secondary RC stars. In the future we would like to make use of a better set of isochrones in terms of sampling (more ages on a logarithmic scale), which will hopefully also include different alpha-enhancements and will take into account atomic diffusion as well as stellar rotation. For a better quantification of the uncertainties, for example when using (Markov Chain) Monte Carlo sampling, it would also be useful to be able to sample ages above the age of the Universe.

6.4.8 High extinction

86 per cent of the stars of this data release have estimated $E(B - V) < 0.2$ mag from Schlegel et al. (1998) and 95 per cent below 0.2 mag. Similarly, 90 per cent and 98 per cent of the stars have estimated $A_{K_S} < 0.1$ mag and 0.2 mag, respectively. If a star has a high and uncertain extinction, this can influence the bolometric luminosity that we estimate and thus introduce biases in the surface gravity and thus all subsequent analyses. Our pipeline especially is only optimized for $E(B - V) < 0.48$ mag, the limit that includes 95 per cent of the initial input catalogue. We therefore caution that trends found among stars with high extinction, and where A_{K_S} estimated via the RJCE method and $E(B - V)$ differ significantly should be treated with caution.

Potassium is estimated from the KI 7699 resonance line. This line is also a good tracer of interstellar potassium which leads to contamination of the stellar line in highly extinct regions. In the future, we aim to estimate the extinction for example via diffuse interstellar bands and possibly use correlation of extinction and line strength of interstellar potassium (Munari & Zwitter 1997) to correct the spectra and measurements of stellar [K/Fe]. For this DR, we however caution the user to check the extinction of stars when using [K/Fe], as we measure this abundance without any corrections causing a rather hard to predict systematics (depending on the velocities of star and ISM) of [K/Fe].

6.4.9 Upper limits

While we report upper limits for advanced users, we strongly recommend that all users take great care in using these measurements. For all elements, but especially for neutron-capture elements, these estimates are pushing the limits of what can be extracted from the

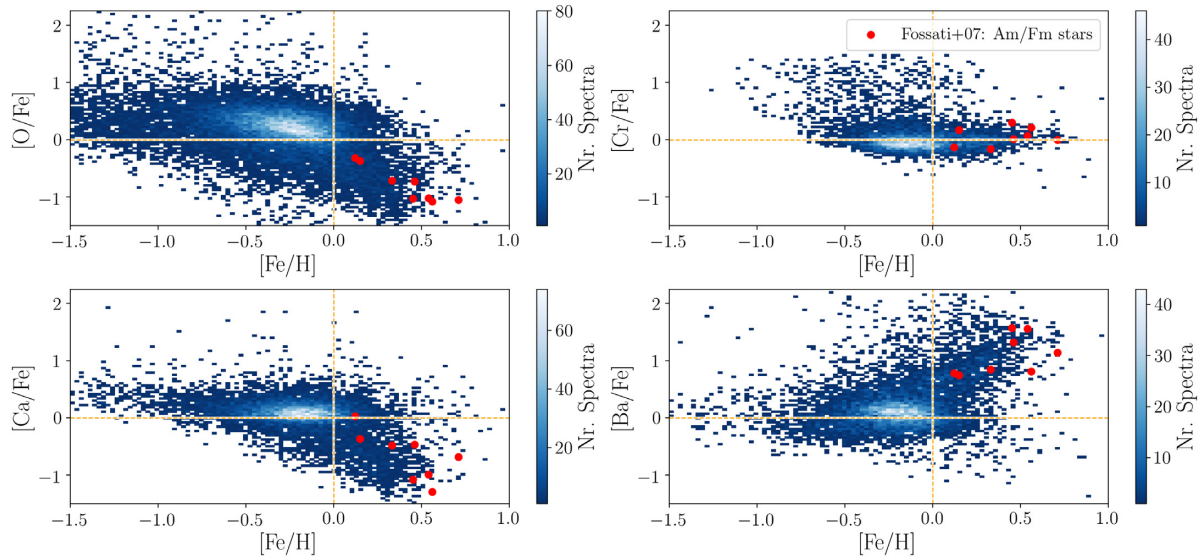


Figure 20. Element abundances $[O/Fe]$, $[Ca/Fe]$, $[Cr/Fe]$, and $[Ba/Fe]$ for GALAH stars with $T_{\text{eff}} > 6500$ K. Overplotted are studies of Am/Fm stars by Fossati et al. (2007) in red.

data and are by definition only an upper limit, not a measurement. We therefore strongly recommend to check upper limit estimates against the data and inspect spectra when possible.

6.5 Peculiarities for certain groups of stars

For some groups of stars, we have found peculiar trends of abundances, for which we cannot exclude astrophysical reasons rather than influences of our analysis and suggest follow-up studies to disentangle those.

6.5.1 Solar and metal-rich giants, especially red clump stars

An ongoing disagreement concerns the stellar parameters of metal-rich giants, and especially metal-rich red clump stars. Already in GALAH DR2 our analysis has yielded unreasonable stellar parameters (in the case of DR2 the estimated $\log g$ were deviating significantly by up to 0.7 dex from those expected from astrophotometry, while T_{eff} and $[Fe/H]$ agreed with other literature estimates/expectations).

For DR3, the use of astrometry and photometry allows us to get more accurate $\log g$. For the metal-rich ($[Fe/H] > 0$) giants and RC stars, however, we notice that the estimated iron abundances show a significant trend of underestimated $[Fe/H]$ with increasing metallicity, when comparing with GALAH DR2. This is an indicator that our synthetic spectra are inaccurate for this specific type of stars or spectra. As discussed above, Jofré et al. (2017) showed that for giant stars, an over-/underestimated v_{mic} can change the measured abundances of some lines significantly, by up to 1.5 dex. The reasons for underestimated $[Fe/H]$ are however more diverse and also include missing/unreliable molecular line data, the underestimation of blending and incorrect continuum normalization. We believe that we can exclude incorrect estimates of $\log g$ estimates, e.g. as a result of poor mass-estimates from missing isochrone models in the supersolar $[Fe/H]$ regime, because photometric and spectroscopic positions in the CMD and Kiel diagrams agree well.

We find systematically higher abundances of Na, Al, Sc, Ti II, Ni, and Ba among metal-rich RC stars when compared to RGB

stars²¹ with increasing disagreement from 0 at Solar $[Fe/H]$ to $\Delta[X/Fe] > 0.4$ dex above $[Fe/H] > 0.2$ dex for these elements. However, another neutron capture element Y is not as affected.

When using the K2 sample with asteroseismic classifications of evolutionary stages within this DR (Stello, private communication), we find a significant difference of around 0.3 dex between RC and RGB stars. The reasons for this might be manifold and could for example suggest non-scaled-Solar abundance patterns for C and N among the RC stars, as shown by Tautvaišienė et al. (2013). The follow-up of these spectroscopic shortcomings are beyond the scope of this paper, but should also assess line saturation and discuss the implications of different formation depths of atomic lines (see e.g. Gurtovenko & Sheminova 2015), which could possibly explain the different effect for different lines within the GALAH range as well.

6.5.2 Abundance patterns of Am/Fm stars

While following up peculiar abundance trends of the hottest stars, we identified a group of stars with high $[Ba/Fe]$ among the stars with $T_{\text{eff}} > 6500$ K, coinciding with those identified by Fossati et al. (2007, 2008) for a handful of stars, see the agreement of their measurements with peculiar pattern of some of the hot GALAH stars in Fig. 20. Similar to Xiang et al. (2020) who identified tens of thousands of these Am/Fm stars we measure typically higher $[Ba/Fe]$ than for the Sun, but lower alpha-enhancement than in the Sun for these typically young stars, when assuming ionization equilibrium.

6.5.3 Young star parameters

We stress that our stellar parameters for the youngest stars (below 0.5 Gyr) are likely unreliable. This is caused by our analysis setup with an isochrone grid selection favouring older stars, tying v_{mic} to an empirical relation and estimating stellar parameters mainly from

²¹These can be identified as unexpected extensions of high $[X/Fe]$ elevated above the majority of stars in Fig. 21, especially when selecting only high- S/N spectra of giants.

iron lines (Baratella et al. 2020), but also neglecting stellar rotation, possible stellar activity, and magnetic fields (Spina et al. 2020b) which can alter the shape of stellar lines quite drastically.

6.5.4 Unexpected over-/underdensities

Below we list several unexpected over- and underdensities, which are likely introduced by our analysis, that is, not the RC area or the red giant bump. While using the recent versions of SME, we have identified several overdensities in the parameter space, coinciding with grid points of the chosen atmosphere grids. We especially warn the user of these overdensities at 3500 K as well as 4750..(250)..8000 K. We further have found an underdensity around stars with temperatures below 4750 K, which coincide with regions of a different atmosphere grid spacing. Comparisons with the IRFM temperatures show however that the temperatures of these stars are not drastically different and we have therefore decided to not flag them. We have further identified an overdensity at 4650 K and $\log g$ of 4.7 dex, which we can ascribe to an issue in the isochrone interpolation due to sparsely available isochrone points.

6.6 Uncertainties

For this data release, we include more accuracy and precision estimates than for GALAH DR2. However, for several stellar parameters and abundances, the means of accuracy estimation are limited, because there are no benchmark values available. We therefore want to caution the user that the accuracy uncertainties might be underestimated and also not complete in terms of their parameter dependence.

For hot stars, we have identified a systematic trend causing increasingly underestimated T_{eff} for hotter stars above 6000 K. The comparison with the GBS shows agreement of our and the literature values within the uncertainties, but our absolute accuracy value for T_{eff} is likely underestimating the uncertainty for the hottest stars.

We have not been able to find enough benchmark values to test the accuracy of [Fe/H] as a function of stellar parameters and therefore only employ an absolute value for the [Fe/H] accuracy. More benchmark measurements, especially with similar conditions to the survey setup (instead of nearby bright stars as validators for distant faint stars), for all stellar parameters would be useful.

For GALAH+ DR3, our precision estimates are based on the repeat uncertainties and internal fitting uncertainties from SME, which for some parameters have been rescaled to match in overall shape. As we continue to develop our pipeline, and obtain more repeat observations in the future, we will be able to also expand the precision estimation not only as a function of an average S/N , but S/N in particular line regions as well as T_{eff} , $\log g$, and [Fe/H], similar to the APOGEE survey (Jönsson et al. 2020).

7 CATALOGUES INCLUDED IN THIS RELEASE

7.1 Catalogue versions before and after *Gaia* eDR3

We have published two versions of our data catalogues, version 1 before *Gaia* eDR3 and version 2 after *Gaia* eDR3. We recommend the use of version 2, as it includes the following updates and fixes:

(i) We have solved the bug concerning barycentric values of `rv_galah` (see Section 6.3). In version 2, we now report our recommended values of v_{rad} based on GALAH measurements, including a correct SME-estimate of v_{rad} , that is `rv_sme_v2`.

(ii) We have cross-matched our targets with the *Gaia* eDR3, parallax zero-point corrections by Lindegren et al. (2021a) and (photo-)geometric distance estimates from Bailer-Jones et al. (2021). We provide all this information in a new VAC (see Section 7.3.1).

(iii) (iv) We have propagated the information from *Gaia* eDR3 to estimate better added values for the VACs on stellar ages as well as dynamics.

7.2 Main catalogues

The main catalogues can be downloaded from the DataCentral²² and accessed via TAP.²³

We provide two main catalogues. The first one `allstar` includes one entry per star and is a cleaned version of the extended `allspec`, with each entry representing the highest S/N measurement for each star and only the combined, final abundance estimates that are unflagged or upper limits.

The `allspec` catalogue includes an entry for each spectrum (multiple entries for some stars). It extends the `allstar` catalogue by also having the raw stellar parameter and abundance measurements, that is, raw measurements without zero-point or bias corrections and uncalibrated fitting uncertainties (`cov*`) for each stellar parameter and individual line abundances (`ind*`), with more extensive flags.

The flags for both the main stellar parameters (`flag_sp`) and the final and raw abundance measurements are listed in Table 4 and explained in Sections 4.3 and 5.3, respectively.

For illustration we plot the distribution of all element abundances in Fig. 21.

After the publication of *Gaia* EDR3, we have added `dr3_source_id` to the main catalogues and updated the reported `rv_galah` and `e_rv_galah` as well as `rv_gaia` and `e_rv_gaia`, as described in Section 7.3.4. The new versions of the catalogues can be found via their suffix `v2`.

We list the table schema of the catalogue in Table A5, but they can also be found in the FITS header or online at <https://datacentral.org.au/services/schema/>. It includes the following categories for the `allstar` and `allspec` catalogues:

- (i) Stellar parameters (see Fig. 14)
- (ii) Stellar parameter flags (both warning and flags)
- (iii) Final uncertainties for each parameter
- (iv) Combined alpha-abundance (for unflagged/upper limit measurements, see Section 3.3)
- (v) Combined element abundances (for unflagged/upper limit measurements, see Section 3.3) and bitmask of the line selection
- (vi) Most important products of the reduction pipeline
- (vii) Cross-matches with *Gaia* DR2, Bailer-Jones et al. (2018), *Gaia* DR2 RUWE, 2MASS,

For the `allspec` catalogue, it also includes

- (i) Individual element abundances (including flagged measurements)
- (ii) Uncalibrated fitting uncertainties
- (iii) More products of the reduction pipeline WISE *W2*

²²<https://cloud.datacentral.org.au/teamdata/GALAH/public/>.

²³<https://datacentral.org.au/vo/tap>.

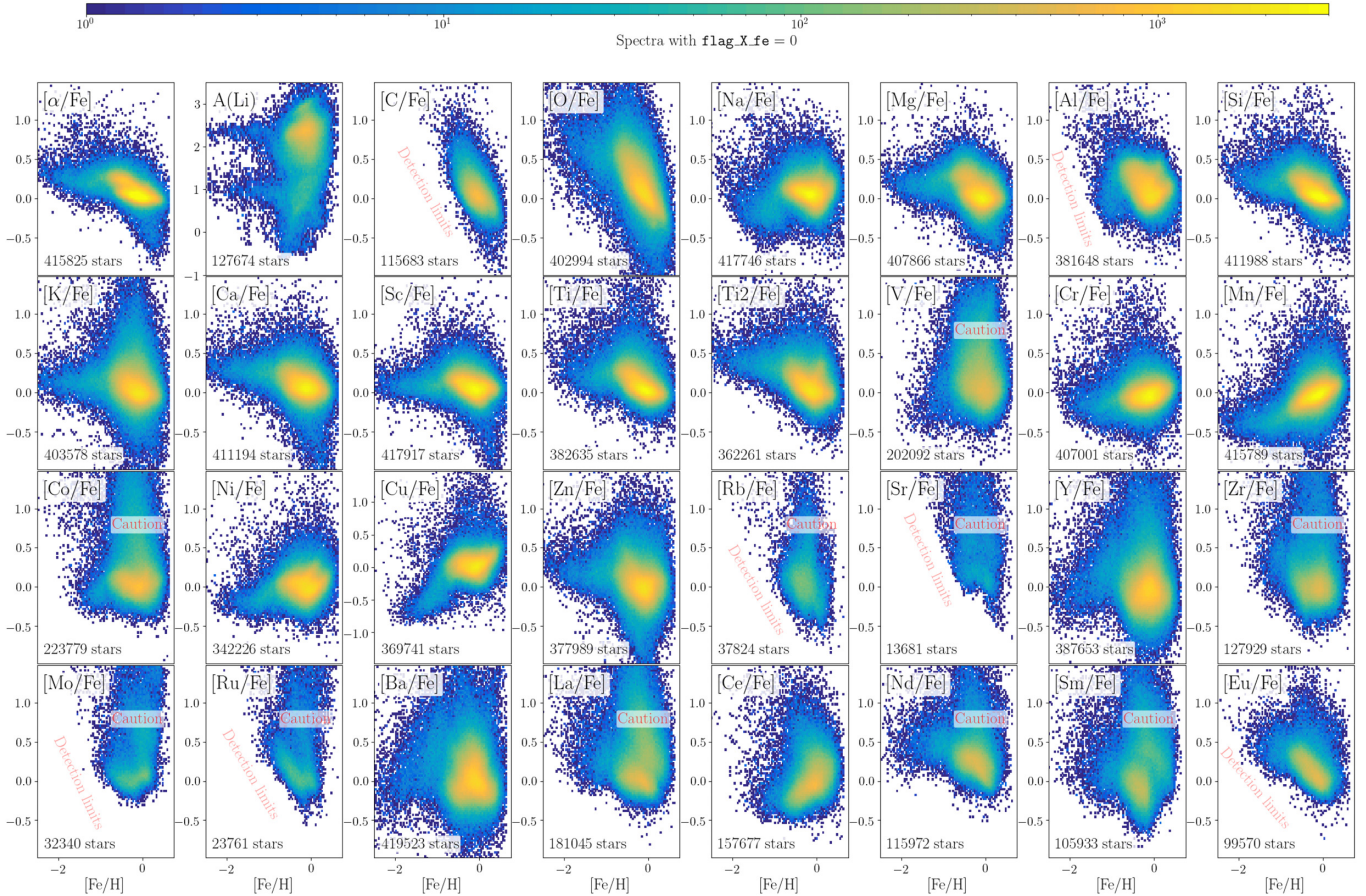


Figure 21. Distribution of the element abundances included in GALAH Data Release 3 over the iron abundance [Fe/H]. Shown are relative abundances [X/Fe] for stars with `X.FE.FLAG = 0` (with exception of Li, for which we show the absolute abundance). Colours indicate the stellar density, truncated at a maximum of 6000 per density bin.

7.3 Value-added-catalogues (VACs)

This data release of GALAH is accompanied by four value-added-catalogues, one for a cross-match with *Gaia* EDR3, one for stellar ages and masses, one with kinematic as well as dynamic information for each star/spectrum, one for more elaborate radial velocity estimates, and a fourth one with additional estimates for double-lined spectroscopic binaries. After the publication of *Gaia* EDR3, we have updated all our catalogues and their latest versions have the suffix v2. Subsequently, we outline the important information used to calculate the additional values for each VAC and note the changes from v1 to v2.

7.3.1 Cross-match with *Gaia* EDR3

As of 2020 December, we provide the cross-match of our allspec-catalogue with *Gaia* EDR3 (Gaia Collaboration 2020; Fabricius et al. 2021), with improved astrometric (Lindgren et al. 2021b) and photometric (Riello et al. 2021) information. We performed this match via the `dr2_source_id`, specifically with the smallest angular distance²⁴ within the internal cross-match catalogue of *Gaia*

²⁴In the future, we suggest to perform this cross-match via GALAH’s 2MASS ID and the yet-to-come match of *Gaia* EDR3 and 2MASS identifiers. We also note that for 57 sources, a sorting via *Gaia* G magnitude would have yielded different identifiers.

DR2 and *Gaia* EDR3 (Torra et al. 2021). For each star, we further list the parallax zero-point as queried from Lindgren et al. (2021a) to correct the parallaxes of the sources with 5 or 6-parameter astrometric solutions from *Gaia* EDR3 (Lindgren et al. 2021b). We further provide the photometric and geometric distance estimated by Bailer-Jones et al. (2021) which were matched via the `dr3_source_id`. The table schema of the VAC is included in the FITS file but can also be found at <https://datacentral.org.au/services/schema/>.

7.3.2 Stellar age and mass estimates

To estimate stellar properties like age, mass, and distance we use the Bayesian Stellar Parameter Estimation code BSTEP (Sharma et al. 2018). BSTEP provides a Bayesian estimate of intrinsic stellar parameters from observed parameters by making use of stellar isochrones. For details of the adopted priors see Sharma et al. (2018), in short, a flat prior on age and metallicity was used and for density distribution of stars a combination of an exponential stellar disc and a diffuse stellar halo was used. For results presented in this paper, we use the PARSEC release v1.2S + COLIBRI stellar isochrones (Marigo et al. 2017). We use the following observables, T_{eff} , $\log g$, [Fe/H], $[\alpha/\text{Fe}]$, 2MASS *J* and *Ks* photometry, and parallax from *Gaia*. The effective observed metallicity was estimated using the formula

$$\log\left(\frac{Z}{Z_{\odot}}\right) = [\text{Fe}/\text{H}] + \log(10^{[\alpha/\text{Fe}]} 0.694 + 0.306) \quad (10)$$

by Salaris & Cassisi (2006), with $Z_{\odot} = 0.0152$ in accordance with the isochrones used. This was compared with the surface metallicity reported by the isochrones, which takes the evolutionary changes in surface metallicity Z into account. The code provides an estimate of age, actual mass, initial mass, initial metallicity, surface metallicity, radius, distance, extinction $E(B - V)$, luminosity, surface gravity, temperature, and the probability of being a red clump star. For each estimated parameter we report a mean value and standard deviation together with the 16th, 50th, and 84th percentiles. The isochrone grid consisted of 16 768 422 grid points. An 81×121 grid spanning $-2 < \log Z/Z_{\odot} < 0.5$ and $6.6 < \log \text{age/Gyr} < 10.12$ was used. The mass dimension of the grid was resampled by interpolation, such that $\Delta \log T_{\text{eff}} < 0.004$ and $\Delta \log g < 0.01$. For each parameter, we report a mean value and standard deviation based on 16 and 84 percentiles. After the publication of *Gaia* EDR3, we have recalculated all entries in this VAC (provided in the table with suffix v2) based on new *Gaia* EDR3 parallaxes and their uncertainties, corrected by the zero-point shifts by Lindegren et al. (2021a). The table schema of the VAC is included in the FITS file but can also be found at <https://datacentral.org.au/services/schema/>.

7.3.3 Kinematic and dynamic information

We provide a Value-Added-Catalogue with kinematic and dynamic information, that builds upon the 5D astrometric information by *Gaia* DR2 and radial velocities preferably from GALAH+ DR3 (97.3 per cent) of all spectra and otherwise from *Gaia* DR2 (0.5 per cent of all spectra). Where possible, we use distance that take into account uncertainties, preferably those estimated via isochrone matching as part of the BSTEP grid-based modelling (95.7 per cent of all spectra, see description in Section 7.3.2), otherwise we use the prior-informed values (4.1 per cent of all spectra) by Bailer-Jones et al. (2018).

For the calculation of orbit information we use version 1.6 of the python package GALPY (Bovy 2015). More specifically, we use its ORBIT module for coordinate/velocity transformation as well as orbit energy computation. To estimate actions, eccentricity, maximum orbit Galactocentric height, and apocentre/pericentre radii, we use GALPY's ACTIONANGLESTAECKEL approximations via the Staechel fudge (Binney 2012) with a focus of 0.45 and the method by Mackereth & Bovy (2018).

For our calculations we use the best-fitting axisymmetric potential by McMillan (2017) with a Solar radius of 8.21 kpc, consistent with the latest measurement by Gravity Collaboration (2019) of $8.178 \pm 0.013_{\text{stat}} \pm 0.022_{\text{sys}}$ kpc, and circular velocity at this radius of 233.1 km s^{-1} . We use the total motion of the Sun in the V-direction of 248.27 km s^{-1} by evaluation of the proper motion measurements from Reid & Brunthaler (2004) at our chosen Solar radius. We further place the Sun 25 pc above the plane (Jurić et al. 2008) and use the peculiar Solar velocities $U_{\odot} = 11.1^{+0.69}_{-0.75} \text{ km s}^{-1}$ and $W_{\odot} = 7.25^{+0.37}_{-0.36} \text{ km s}^{-1}$ by Schönrich, Binney & Dehnen (2010), but $V_{\odot} = 15.17 \text{ km s}^{-1}$. This value is higher than the $12.24^{+0.47}_{-0.47} \text{ km s}^{-1}$ from Schönrich et al. (2010), but given the ongoing debate (see e.g. the discussion in Sharma et al. 2014) of this value, we choose our value for internal consistency between the chosen total and peculiar motions of the Sun in our reference frame with a given circular velocity.

For the Sun, this leads to actions of $J_R = 7.7 \text{ kpc km s}^{-1}$, $J_{\phi} = L_Z = 2038.3 \text{ kpc km s}^{-1}$, and $J_Z = 0.4 \text{ kpc km s}^{-1}$ on an orbit with eccentricity 0.073, a pericentre radius of 8.15 kpc, apocentre radius of 9.43 kpc, and a total energy of $E_{n,\odot} = -1.53 \cdot 10^5 \text{ km}^2 \text{ s}^{-2}$.

We provide columns for the heliocentric Cartesian coordinate (X , Y , Z) and velocity frames (U , V , W) as well as the Galactocentric cylindrical coordinate (R , ϕ , z) and velocity frames (v_R , tangential speed in azimuthal direction $v_T = R \cdot \frac{d\phi}{dt}$, v_z) together with the actions (J_R , $J_{\phi} = L_Z$, J_Z), eccentricity (e), maximum Galactocentric orbit height (z_{max}), pericentre and apocentre radii (R_{peri} , R_{ap}), as well as orbit energies for the best value input. We further realize 10 000 Monte Carlo samplings per star/spectrum by sampling *Gaia* astrometry within the uncertainties.²⁵ For the distance sampling in version 2, we sample with 2 Gaussians (half the sample with a standard deviation based on the 16th percentile below the median and the other half with 84th percentile above the median) linearly in the distance modulus. For version 1, we assumed Gaussian uncertainties when using the BSTEP distances or sample from a 2-sided Gaussian in distance based on the bold assumption that the distributions left and right of the mode stated by Bailer-Jones et al. (2018) are Gaussian and we can thus describe them via the stated lower and higher percentiles.²⁶ We then provide the 5th, 50th, and 95th percentile for the user for each orbit parameter. For the 269 spectra in version 2 and 101 spectra in version 1, where the dynamic calculations yield unbound orbits, we only report the kinematic properties.

After the publication of *Gaia* EDR3, we have recalculated all entries in this VAC based on updated distances as well as v_{rad} and provide them in a table with the suffix v2. We indicate, which distance is used, with the flag `use_dist_flag`, with the values 0 (649453 spectra for which we use the distances from version 2 of the VAC on ages described in Section 7.3.2), 1 (27639 spectra) when using the photogeometric distances from Bailer-Jones et al. (2021), 2 (41 spectra) when using the geometric distances from Bailer-Jones et al. (2021), and 4 when using distances by inverting parallaxes (0 spectra). All methods take into account the zero-point shifts by Lindegren et al. (2021a) and the flags are based on the availability of each distance method (preferring BSTEP over photogeometric over geometric over inverted-parallax distances), where flag `use_dist_flag = 8` indicated that no distance was available (1290 spectra). We use updated RV from version 2 of our RV VAC by selecting the RV based on the `use_rv_flag` described in Section 7.3.4. The table schema of the VAC is included in the FITS file but can also be found at <https://datacentral.org.au/services/schema/>.

The space velocities (V_R , V_T , V_z) in the Galactocentric frame are shown in a Toomre diagram in Fig. 22(a). Most of the stars observed as part of GALAH+ DR3 have disc-like kinematics similar to the local standard of rest, but an extension of stars with lower rotational velocity than the disc ($V \ll 0 \text{ km s}^{-1}$) are shown and indicate that several stars with halo-like kinematic properties are part of GALAH+ DR3.

For the computed phase space and dynamic properties, we report a variety of statistical values. In addition to the best value, that is computed by using the best values as input, we also sample the distribution for each property within the uncertainties via Monte Carlo sampling with size 1000 and report the 5th, 50th, and 95th

²⁵In version 2 we sample values using the *Gaia* covariances and replace the distance and radial velocity sample with our own independent sample. In version 1 we neglected the covariances, but also provide a script to take them into account.

²⁶We want to stress however, that given the excellent parallax quality for the vast majority of our sample (see Fig. 3), these choices are only affecting less than 5 per cent of the observed stars with parallax uncertainties above 20 per cent, for which we caution the user to carefully assess the quality of both the astrometry as well as our distance and thus kinematic/dynamic estimates.

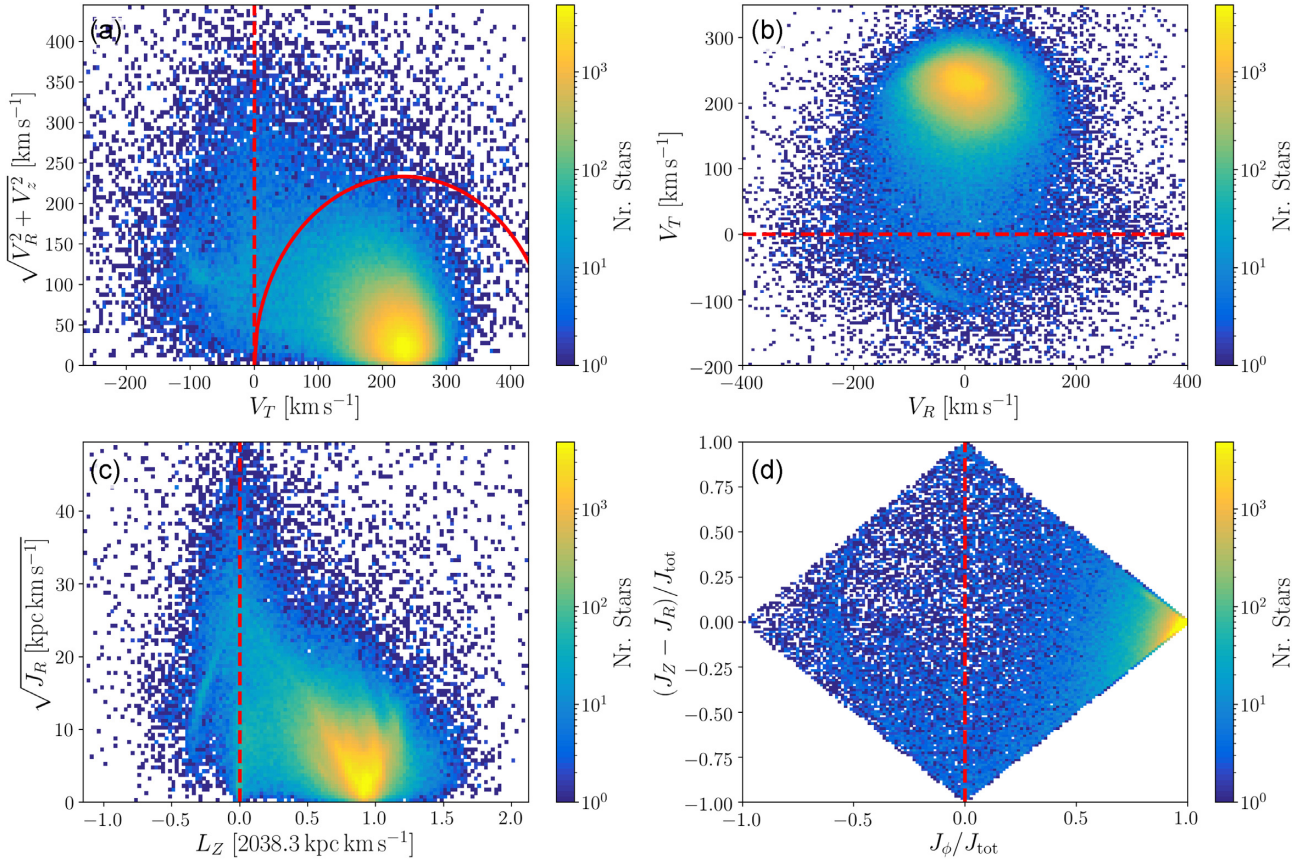


Figure 22. Coverage of stellar kinematics (space velocities) and dynamics (actions) for the stars observed as part of GALAH. Panel (a) shows a Galactocentric version of the Toomre diagram (compare to e.g. Bonaca et al. 2017; Feuillet et al. 2020), panel (b) the Galactic space velocities (compare to e.g. Belokurov et al. 2018; Feuillet et al. 2020), panel (c) two actions (compare to e.g. Trick, Coronado & Rix 2019; Feuillet et al. 2020), and panel (d) the distribution of actions (compare to e.g. Vasiliev 2019). The vast majority of stars in GALAH+ DR3 has both azimuthal / transversal Galactocentric velocities and angular momenta very similar to the Sun ($V_{\odot} = 248.27 \text{ km s}^{-1}$, $J_{\phi} = L_z = 2038.3 \text{ kpc km s}^{-1}$). The red dashed lines in each panel indicate an angular momentum or azimuthal velocity of 0 kpc km s^{-1} or 0 kkm s^{-1} respectively. The red line in panel (a) indicates a total velocity of 233.1 km s^{-1} . We note that the overdensity at low $V_T \sim -85 \text{ km s}^{-1}$ in panels (a) and (b) as well as the streak at $-0.25L_{z,\odot}$ in panel (c) and $-0.6J_{\phi}/J_{\text{tot}}$ in panel (d) coincide with the location of the distant targeted star of the globular cluster $\omega \text{ Cen}$ with mean *Gaia* parallax uncertainties of 46 per cent.

percentiles of these distributions. An example of the sampling of parameters for 100 randomly selected stars is shown in Fig. 23. We also provide the code to perform this sampling with different sampling choices. Whereas we currently sample the properties by assuming their input parameters are uncorrelated, we also provide the code to sample with the *Gaia* correlation matrices. The latter are currently not applying a distance prior and are thus problematic for large distances. However, we stress, that the vast majority of the stars from GALAH+ DR3 have very precise parallax measurements, for which the sampling choice is negligible (see Fig. 3).

The distribution of heliocentric coordinates (X , Y) and Galactocentric cylindrical coordinates (R , z) is shown in Figs. 24(a) and (d). The vast majority of targets are distributed within 4 kpc from the Sun and covers a large fraction of the disc. Because of the target selection of the GALAH main programme ($|b| > 10 \text{ deg}$), relatively few stars are observed close to the Galactic plane. We remind, however, that GALAH+ DR3 includes also observations from TESS-HERMES, K2-HERMES, and several smaller projects that targeted the Galactic bulge and clusters. The distribution in Fig. 24(a) is hence also including observations with $|b| < 10 \text{ deg}$ especially towards the Galactic centre at $(R, z) = 0$. A combination of distance uncertainties and special targeting of clusters and K2/TESS fields is causing unrealistic streaks in both Figs 24(a) and (d).

7.3.4 Radial velocities

As outlined in Section 4.1.9, we provide a value-added-catalogue for radial velocities. In version 2 of this VAC, we list all values of measurements from SME (now with suffix *sme*, rather than suffix *galah* as in version 1), measurements from Zwitter et al. (2020) with suffix *obst* based on an improved algorithm based on the work by Zwitter et al. (2018). The latter estimates were performed with a grid of 718 template spectra (created from observed HERMES spectra in selected T_{eff} , $\log g$, $[\text{Fe}/\text{H}]$, and $[\alpha/\text{Fe}]$ bins). These make use of the whole spectrum rather than just a specific wavelength regions used for the stellar parameter estimation with the main pipeline (providing v_{rad} estimates under *rv_sme_v2*). We furthermore provide v_{rad} estimates which correct for gravitational redshift (*rv_obst*, which we recommend to use). The catalogue also includes corrections for incorrect barycentric velocity shifts as outlined in Section 6.3 and v_{rad} from *Gaia* DR2, as reported in *Gaia* EDR3. Based on feedback from the scientific community, we report our recommendation for v_{rad} estimated from GALAH in the columns *rv_galah* and *rv_galah*, together with a flag *use_rv_flag* to indicate their origin (0 for 563260 spectra using *rv_obst*, 1 for 86173 spectra using *rv_sme_v2* and 2 for 14190 spectra, when we the latter column is empty, but we recommend to use the available

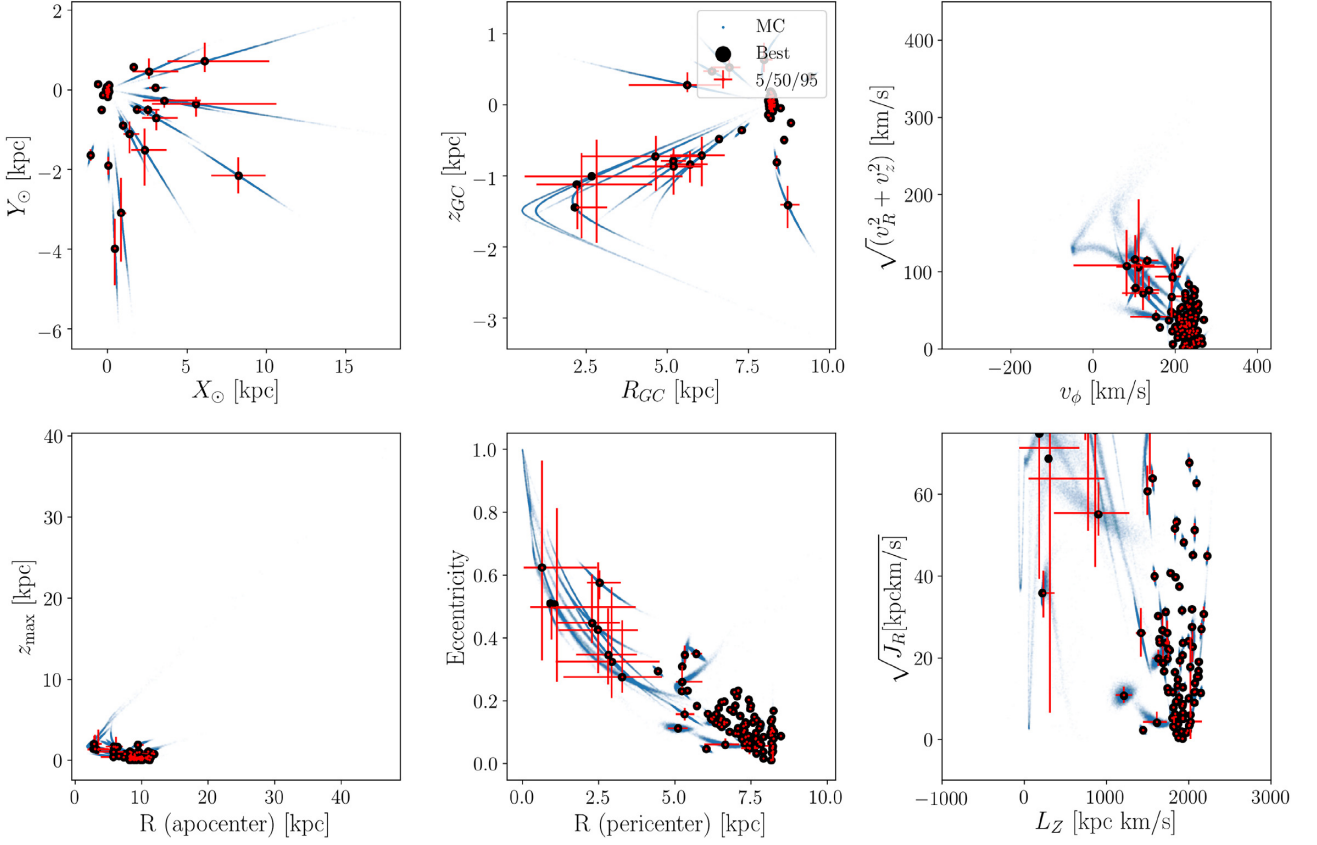


Figure 23. Overview of phase space and dynamic stellar properties for randomly chosen stars from GALAH+ DR3, including their sampling within the measurement uncertainties. The black points indicate the values calculated from the best 6D information. The blue points indicate 1000 samples from the 6D information per star within the uncertainties. The red error bars indicate the distribution between 50th percentile (middle of the cross) and the 5th and 95th percentile, respectively.

`dr2_radial_velocity` value from *Gaia* DR2 or 4 for 14800 spectra for which no RV is available in either survey. The table schema of the VAC is included in the FITS file but can also be found at <https://datacentral.org.au/services/schema/>.

7.3.5 Double-lined spectroscopic binary stars

Binary stellar systems represent a significant fraction of stars in our Galaxy. Therefore, their effect on observations, as well as their impact on the Galactic environment, have to be properly taken into account when studying Galactic structure and evolution. To this end, we present a sample of 12 760 binary systems for which the properties of their stellar components were derived in a separate analysis from that described in Section 3. In order to compute individual parameters for both stars ($T_{\text{eff}[1,2]}$, $\log g_{[1,2]}$, $V_{r[1,2]}$, $v_{\text{mic}[1,2]}$, $v_{\text{broad}[1,2]}$, $R_{[1,2]}$), together with a common metallicity and extinction for the binary system ($[\text{Fe}/\text{H}]$, $E(B - V)$), we combine information from GALAH spectra, *Gaia* DR2 parallax, and data from several photometric surveys (APASS; Henden et al. 2015, *Gaia* DR2; Gaia Collaboration 2018, 2MASS; Skrutskie et al. 2006, WISE; Cutri et al. 2014) into a joint Bayesian scheme. The details of the analysis are described in Traven et al. (2020), and the catalogue of derived parameters is available at CDS.²⁷

²⁷<http://cdsarc.u-strasbg.fr/viz-bin/cat/J/A+A/638/A145>

The binary stars presented in this VAC were detected in a sample of 587 153 spectra from the second GALAH internal data release. We investigated direct products of the reduction pipeline before implementation of some improvements described in Section 2.3. Detection of binarity was performed using a t-SNE classification and a cross-correlation analysis (Merle et al. 2017; Traven et al. 2017) of GALAH spectra. The final sample of this catalogue consists of systems with mostly dwarf components, a significant fraction of evolved stars, and also several dozen members of the giant branch. The statistical distributions of derived stellar properties can be further used for population studies (G. Traven et al., in preparation), and show trends which are expected for a population of close binary stars ($a < 10$ au) with mass ratios $0.5 \leq q \leq 1$. Our results also indicate that the derived metallicity of binary stars is statistically lower than that of single dwarf stars observed in the same magnitude-limited sample of the GALAH survey. Among other reasons, this might point to an anticorrelation between the binary fraction and metallicity of close binary stars, as recently explored by e.g. Moe, Kratter & Badenes (2019), Bate (2019), and Price-Whelan et al. (2020).

8 GALAH+ DR3 IN CONTEXT

The GALAH collaboration releases millions of abundance measurements for 678 423 spectra of 588 571 stars. In this section, we put this achievement into perspective. This release provides, to the best of our knowledge, the largest number of element abundances from high-resolution ($R \sim 28\,000$) spectra published so far for a well-

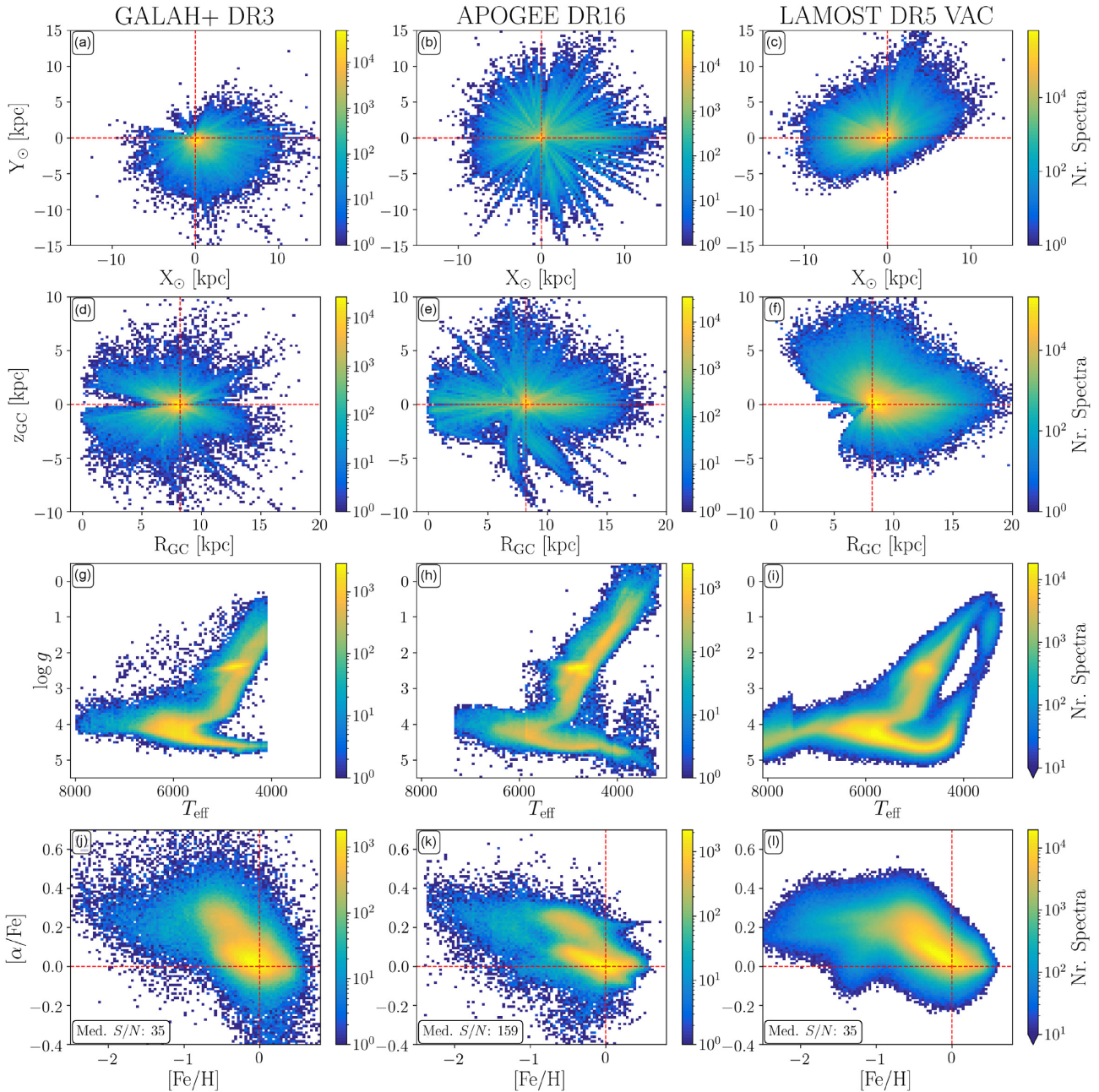


Figure 24. Comparison of GALAH+ DR3 (left-hand panels) with APOGEE DR16 (middle panels) and LAMOST DR5 VAC (right-hand panels). The surveys trace different Galactic regions as shown in the heliocentric Cartesian frame (a–c) as well as the Galactocentric cylindrical frame (d–f) across different stellar types (seen in the overview of the T_{eff} - $\log g$ coverage in panels (g)–(i) across different stellar populations (shown in the Tinsley-Wallerstein diagrams, $[\text{Fe}/\text{H}]$ versus $[\alpha/\text{Fe}]$, in panels (j)–(l). Numbers in the bottom left-hand of panels (j)–(l) indicate the median SNR for CCD2 of GALAH, SNR for APOGEE, and SNR G for LAMOST for the shown stars, which are indicative of the precision that can be reached by the spectrum analysis. We note that the colour bars of all panels are having different scales.

selected sample of stars with the promise of most precise dynamic and age information. This number is, however, still rather small compared to the roughly 1.5 billion stars observed by *Gaia* (Gaia Collaboration 2016b), which aims to observe about 1 per cent of all Milky Way stars, and also limited mainly to stars in the Solar vicinity within 4 kpc. However thanks to our information on stellar orbits, we can learn or infer results beyond the volume of the present day stellar positions in the Galaxy (May & Binney 1986).

To be able to perform Galactic archaeology on a truly galactic scale, it is therefore vital to be able to use the measurements of other large-scale stellar surveys. In Section 8.1 we compare some key properties, like spatial coverage as well as observed stellar types and the major abundance tracers $[\text{Fe}/\text{H}]$ and $[\alpha/\text{Fe}]$ from GALAH+ DR3 with those from two other ongoing surveys, namely APOGEE (DR16 Ahumada et al. 2020; Jönsson et al. 2020) and LAMOST (DR5 Deng et al. 2012; Zhao et al. 2012; Xiang et al. 2020). Both of these surveys provide millions of measurements for multiple elements, but we note

that there are several other surveys which also provide abundance measurements (but for typically fewer elements and/or stars), like the Geneva–Copenhagen Survey (Nordström et al. 2004; Casagrande et al. 2011), SEGUE (Yanny et al. 2009), RAVE (Steinmetz et al. 2020a,b), and *Gaia*-ESO (Gilmore et al. 2012). In Section 8.2, we highlight the potential to further our understanding of Galactic and stellar chemical evolution with Li, one of the 30 elements measured by GALAH. In Section 8.3, we then showcase some of the specific advantages of GALAH for the exploration of the chemodynamic evolution of the Milky Way.

8.1 Galactic archaeology on a global scale

To understand how we can use the available surveys on a global scale, two key points need to be considered. First, if the surveys are complementary and secondly if the surveys are on the same scale.

While a detailed comparison of overlapping stars between the surveys would be very helpful to assess systematic trends, it should be performed in a dedicated study and include comparisons of stellar parameters as well as abundances for different parameter selections. Some basic comparisons can be found in our open-source repository, but a detailed study is beyond the scope of this paper.

In this section, we are rather aiming to give explanations why different surveys may not depict the same trends on first glance (based on different selection functions), while highlighting the potential of combining the different surveys.

GALAH+ DR3 includes 678 423 combined spectra of 588 571 stars, obtained at high-resolution (28 000) in 4 narrow optical bands (covering 1000 Å). APOGEE DR16 includes 473 307 combined spectra of 437 445 stars, obtained at high-resolution (22 500) in the H-band (15 000–17 000 Å). LAMOST DR5 VAC includes 8 162 566 combined spectra of 6 091 116 stars, obtained as low-resolution (1800) in the full optical range (4000–9000 Å). It is important to note that this VAC is estimated by data-driven models trained on GALAH DR2 and APOGEE DR14.

The overlap of GALAH+ DR3 and APOGEE DR16 is 15 047 stars, that is 3 per cent of the each survey. The overlap of GALAH+ DR3 and LAMOST DR5 is 47 118 stars, that is 8 per cent and 1 per cent of the respective survey. The overlap of APOGEE DR16 and LAMOST DR5 is 111 626 stars, that is 26 per cent and 2 per cent of the respective surveys.

These numbers show that the surveys are very complementary in the stars that they target, but also have a non-negligible overlap between them. Even more important, this overlap allows us to test if these surveys are on the same scale and even to cross-calibrate them to bring them on the same scale (see Casey et al. 2017; Ho et al. 2017; Nandakumar et al. 2020; Wheeler et al. 2020; Xiang et al. 2020).

For the subsequent comparison we limit the samples to those stars with `flag_sp = 0`, `flag_fe = 0`, and `flag_alpha_fe = 0` for GALAH, `ASPCAPFLAG = 0` for APOGEE, and `FLAG_SINGLESTAR = 0`, `QFLAG_CHI2 = 'good'` as well as SNR ratios for at least 30 for either G, R, or I for LAMOST's DR5 VAC.

Because the three surveys operate on different sites, they are typically observing different regions of the sky. This can be seen in Figs 24(a)–(f), where we show the spatial distribution of stars in heliocentric Cartesian coordinates (X versus Y in Figs 24a–c) and Galactocentric cylindrical coordinates (R versus z in Figs 24d–f). While GALAH observes stars of the Southern hemisphere, LAMOST targets mainly the Northern hemisphere (compare Figs 24a and c), and APOGEE observes both hemispheres. When looking at the Galactic spatial distribution, we see the selection function of GALAH, especially $|b| > 10$ deg introducing a lack of stars in the

plane (panel d), whereas APOGEE is mainly targeting the plane (small z in panel e) and LAMOST (panel f) targets all regions except the inner Galaxy.

Figs 24(f)–(h) depicts the distribution of T_{eff} and $\log g$ for the surveys, which now all deliver results for all different stellar types and evolutionary stages (for example APOGEE, which mainly focused on the observation and analysis of giants in previous releases, now also delivers dwarf parameters with DR16).

The elemental abundances obtained by these surveys are data of particular interest for Galactic archaeology. A detailed comparison of those between the surveys is beyond the scope of this paper. Typically, different surveys operate at different resolutions and reach different S/N in different wavelength regions, thus selecting different lines for their analyses. Different lines again, can form at different optical depths and may be blended differently; all possible factors for possibly different abundance measurements (Jofré et al. 2019).

For α -element abundances another important consideration is how these are defined and computed. For GALAH+ DR3, we provide individual element abundances for Mg, Si, Ca, and Ti, but also compute a combined $[\alpha/\text{Fe}]$ value from error-weighted combinations of well selected individual lines from these elements (see Section 3.3), resulting in the distribution shown in Fig. 24(j). Because of the differences in yields between these different α -elements, the enhancement pattern of different α -process elements looks slightly different to each other, and a combined α -enhancement label is only a compromise to reach a higher precision. For DR3, this compromise is dominated by Si and Ti, followed by Mg as the most precisely measured elements, with rather little contribution from Ca. For APOGEE DR16, on the other hand, $[\alpha/M]$, which we convert to $[\alpha/\text{Fe}]$ in Fig. 24(k) is computed using all lines in the APOGEE wavelength range and adjusting all of the $[X/\text{Fe}]$ at the same time by the same amount. For LAMOST DR5, we show the VAC estimates trained on GALAH DR2 by Xiang et al. (2020). When comparing these distributions, it is important to keep in mind the quality of data that was used for the analysis. The median S/N for GALAH and LAMOST is 35, which is 4.5 times lower than the median S/N of 159 achieved by APOGEE. We therefore expect that the scatter for GALAH and LAMOST is larger, as can be seen in Figs 24(j)–(l). Furthermore it is important to keep in mind that these distributions trace different regions of the sky, different distributions of stellar types, and thus likely also different distributions of stellar populations. Especially for APOGEE, we expect a larger ratio of stars from the bulge and high- α disc, which will change the colourmap distribution.

When comparing with APOGEE DR16 abundances quantitatively (see Table A2), we find an excellent agreement for most abundance zero points, that is sky flats and vesta, including 0.00 ± 0.01 dex for $[\text{Fe}/\text{H}]$ and -0.01 ± 0.05 dex for $[\alpha/\text{Fe}]$. The difference for all stars with unflagged abundances between APOGEE DR16 and GALAH shows a slightly lower $[\text{Fe}/\text{H}]$ for GALAH (-0.05 ± 0.14 dex) and slightly higher $[\alpha/\text{Fe}]$ (0.02 ± 0.07 dex). For a comparison of the other elements we refer to Table A2.

8.2 Galactic and stellar chemical evolution

In this section, we briefly aim to show the potential of GALAH+ DR3 for the exploration of Galactic and stellar chemical evolution, while leaving the true exploration to the scientific community. One would ideally like to take all abundance measurements into account for such an endeavour, including GALAH's main goal of the chemical tagging experiment, but here we aim to show how much potential the exploration of a single element has to offer.

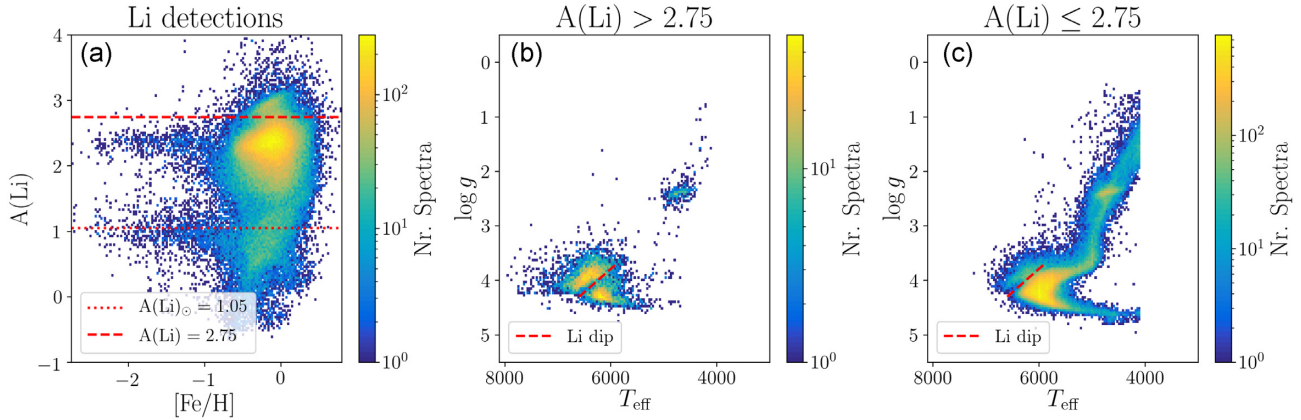


Figure 25. Overview of Lithium in the abundance and parameter plane. Panel (a) shows the distribution of $A(\text{Li})$ as a function of $[\text{Fe}/\text{H}]$ for all successful measurements (no flags). The abundances cover a range of almost 5 dex, with the majority of stars between 2 and 3 dex. We also show dotted and dashed lines of Solar and primordial $A(\text{Li})$, respectively. Several stars extend towards low $[\text{Fe}/\text{H}]$ with $A(\text{Li})$ on the Spite plateau ($A(\text{Li}) \sim 2.3$ dex). Panels (b) and (c) show the distribution of stars in the Kiel diagram with $A(\text{Li})$ above or below the primordial ($A(\text{Li}) = 2.75$ dex). Li-rich stars are either warm and cool dwarfs (with the exception of stars at the Li dip, indicated as dashed red line) or Li-rich giants, mainly in the red clump stage. Detected Li-poorer stars, however, cover the whole parameter range.

In Fig. 25, we plot the distribution of lithium in different projections. Fig. 25(a) shows the absolute abundance $A(\text{Li})$, as a function of $[\text{Fe}/\text{H}]$. We indicate two important values, the theoretical prediction of $A(\text{Li}) = 2.75$ from the big bang Nucleosynthesis (Pitrou et al. 2018) and the photospheric abundance of the Sun $A(\text{Li})_{\odot} = 1.05$ (Asplund et al. 2009). First of all, it is important to notice that we only plot the stars with unflagged Li measurements (`flag_sp = 0` and `flag_li_fe = 0`). These are 127 674 measurements or 18.8 per cent of all GALAH+ DR3 stars.

In this projection, several substructures are noticeable. While the mean abundance of all stars is $A(\text{Li}) = 2.2^{+0.3}_{-0.7}$ dex, we actually see a large spread of $A(\text{Li})$ between -0.5 and 4.0 dex across for $[\text{Fe}/\text{H}] > -1$ dex. Among many others, Ramírez et al. (2012) and Bensby & Lind (2018) explored this pattern in their studies extensively by analysing its correlation with stellar parameters, stellar populations as well as age and temperature and found a strong correlation for example between temperature and $A(\text{Li})$. When we only plot the stars with the largest $A(\text{Li})$, especially above the theoretical primordial value of 2.75, we find that only specific groups of stars exhibit these abundances, see Fig. 25b, namely hot dwarf stars and few lithium-rich giants. Because of the dredge-up, we would not expect such high amounts of Li in giants, which questions our understanding of stellar physics and evolution. With the new more reliable data from GALAH+ DR3, more scenarios of Li production during binary interaction or the He-flash in giant stars (see e.g. Casey et al. 2019; Kumar et al. 2020) can be tested more reliably, indicating that lithium-rich giant stars require multiple formation channels (Martell et al. 2020).

Thanks to the hundreds of thousands of Li measurements, we are also able to study phenomena which previously have mainly been analysed in cluster stars, such as the occurrence of the Li dip (Boesgaard & Tripicco 1986), a region among the warm dwarf stars, for which deep mixing induced by rotation and meridional circulation causes strong Li depletion. The first analysis of this region with GALAH+ DR3 by Gao et al. (2020) has identified a significant offset between the warm and cool side of this Li dip of $0.4 - 0.5$ dex. Down to metallicities of $[\text{Fe}/\text{H}] \sim -1$ dex this offset appears metallicity-independent which sheds new light on the famous disagreement between predicted Li abundance and the one measured in cool, old, metal-poor on the Spite plateau of $A(\text{Li}) \sim 2.3$ dex

(Spite & Spite 1982). In particular, Gao et al. (2020) speculate that the most metal-poor stars on the warm side of the dip may have experienced insignificant Li depletion as well as insignificant Galactic Li enrichment, naturally explaining why their abundances closely reflect those predicted by standard big bang nucleosynthesis.

Several of these metal-poor stars ($[\text{Fe}/\text{H}] < -1$ dex) have actually been identified as stars of the accreted *Gaia*-Enceladus-Sausage. With GALAH data, both Molaro, Cescutti & Fu (2020) and Simpson et al. (2020) show that the distribution of $A(\text{Li})$ from the accreted stars, like the GES agrees with different populations of the Milky Way, an important confirmation that the Cosmological Lithium problem is not a consequence of formation environment (see also Nissen & Schuster 2012; Cescutti, Molaro & Fu 2020).

8.3 Chemodynamical evolution

To assess the potential of GALAH+ DR3 in terms of exploring the chemodynamic evolution of the Milky Way, we show the distribution of the data in plots that have been used in seminal studies for Galactic exploration.

Similar to Hayden et al. (2015), we plot the distribution of α -enhancement versus iron abundance for stars of GALAH+ DR3 in different spatial bins, that is different bins in Galactic radius (from inner Galaxy on the left to outer Galaxy on the right) as well as Galactic height (from the Galactic plane in the bottom to more than 1 kpc above or below the plane in the top) in Fig. 26. The Solar vicinity, which is located in the bottom centre of this figure hosts by far the most stars of GALAH+ DR3 and consists mainly of low- α (thin) disc stars. When looking at larger Galactic heights, stars of the high- α (thick) disc become dominant, in good agreement with the results by Hayden et al. (2015) based on APOGEE data. However, we find a less pronounced abundance gradient of the low- α disc with Galactic radius, which we believe is attributed to less reliable iron abundances of distant, metal-rich giants (mainly expected in the inner Galaxy), as outlined in Section 6.5. In agreement with Hayden et al. (2015), we see a clear separation of the overdensities of low- and high- α disc stars and a spatial invariance of the position of the peak/distribution of the high- α disc stars. With the improved distances thanks to the *Gaia* mission, we are able to also explore

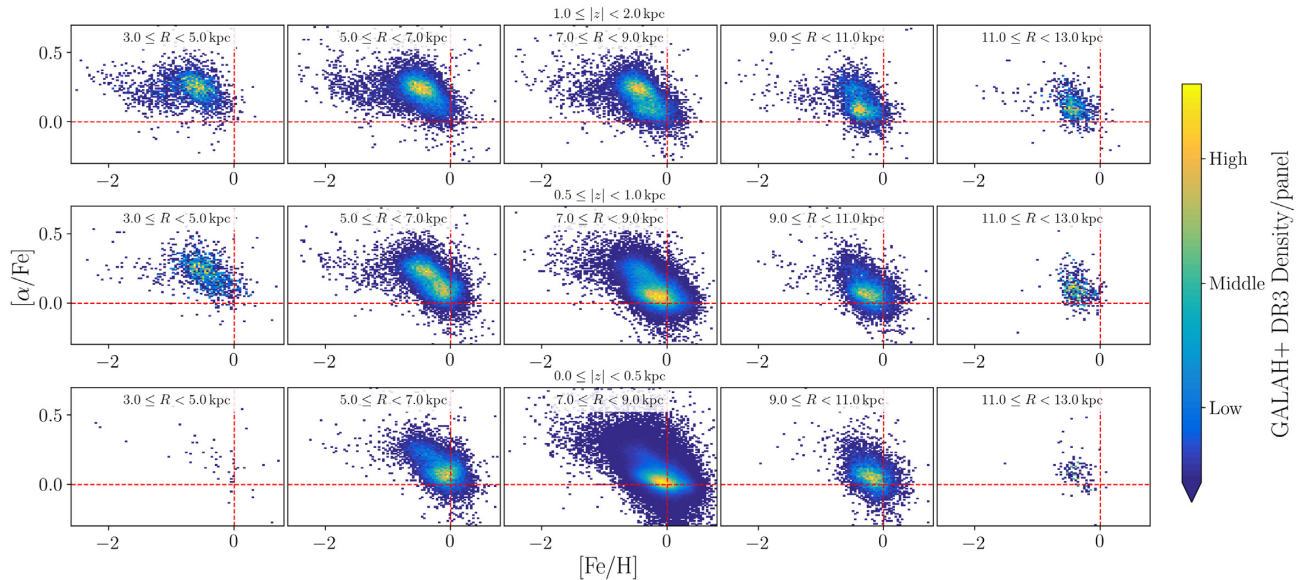


Figure 26. Spatial coverage of GALAH shown with Tinsley–Wallerstein diagrams, $[\text{Fe}/\text{H}]$ versus $[\alpha/\text{Fe}]$, for different regions (R , z) of the Galaxy. With 81.2 per cent of stars within 2 kpc, the majority of stars are located in the bottom middle panels. However, we see an evidence of a similar structure as was observed by Hayden et al. (2015) with APOGEE data, that is, first a gradient of $[\text{Fe}/\text{H}]$ for the low- α disc with decreasing $[\text{Fe}/\text{H}]$ towards larger radii, and secondly a coordinate independent chemical composition of the majority of high- α disc.

the most distant bins (beyond 2 kpc) of this spatial distribution and find several stars with $[\text{Fe}/\text{H}]$ below -1 dex at larger Galactic heights ($|z| > 0.5$ kpc), coinciding with the chemical composition of the metal-weak extension of the high- α disc as well as most halo stars, including the recently identified *Gaia*–Enceladus–Sausage stars (see further explanations below).

With the provided VAC on stellar ages, we are also able to assess the data set by this important property. Many recent studies (e.g. Haywood et al. 2013, 2019; Bensby et al. 2014; Hayden et al. 2017; Minchev et al. 2017) have shown the potential of including ages when assessing the Milky Way populations. Buder et al. (2019) have further shown that age and chemistry combined (as more conserved properties than kinematics/dynamics) can help us to dissect the disc populations. Among the 415653 stars in GALAH+DR3 with unflagged stellar parameters, $[\text{Fe}/\text{H}]$, and $[\alpha/\text{Fe}]$ as well as ages, we find 1.8 per cent with $[\text{Fe}/\text{H}] \leq -1$. When assigning the other stars to young (≤ 8 Gyr) and old (> 8 Gyr) as well as low- α ($[\alpha/\text{Fe}] \leq 0.2$) and high- α ($[\alpha/\text{Fe}] > 0.2$) groups, we find 62.5 per cent young low- α stars, 8.8 per cent young high- α stars (compare to 5.8 per cent found within APOKASC by Martig et al. 2015), and 26.9 per cent old stars (21.5 per cent low- α and 5.4 per cent high- α).

The vast majority of GALAH targets, especially the 62.5 per cent young low- α stars, are expected to move on orbits very similar to the Sun. In Fig. 22 this is confirmed in all panels of kinematic and dynamic properties, where most stars are located close to the Sun ($V_{\odot} = 248.27 \text{ km s}^{-1}$, $J_{\phi} = L_Z = 2038.3 \text{ kpc km s}^{-1}$) and exhibit only small radial and vertical velocities / actions.

Although halo stars are not the main target of GALAH, roughly 1 per cent of all GALAH targets are expected to belong to the chemical or kinematic halo (De Silva et al. 2015). While the definition of halo stars is contentious, we at least aim to assess their rough number by looking at different kinematic and dynamic properties. For this, we look at the distribution of azimuthal / transversal velocity V_T with respect to the combined radial and vertical velocity $\sqrt{V_R^2 + V_z^2}$ in Fig. 22.

The majority of stars move on almost circular orbits at Solar radius ($V_T \sim v_{\text{circ}} = 233.1 \text{ km s}^{-1}$). Half of all GALAH stars differ by less than 57 km s^{-1} from this total velocity. Only 8.2 per cent, 4.4 per cent, and 2.4 per cent are more than 140, 180, and 233.1 km s^{-1} from this total velocity. In the literature, the latter two values have been used to assign stars to the kinematic halo, and while such distinct cuts are debatable, their numbers are significantly higher than the initially estimated 1 per cent (De Silva et al. 2015), partially due to the additional surveys like K2-HERMES contributing to GALAH+DR3. These stars do not move coherently with the (local) disc, but are on kinematically hotter orbits. This suggests that they are for example halo stars or belong to the bulge. 1.2 per cent of the stars even move on retrograde orbits.

Similar to Belokurov et al. (2018) we can identify an overdensity of the *Gaia*–Enceladus–Sausage (GES) (see e.g. Helmi 2020, and references therein) in Fig. 22(b) along an extended range of $-400 < V_R < 400 \text{ km s}^{-1}$ along small Galactocentric azimuthal velocities, that is, following closely the dashed red line indicating $V_T \sim 0 \text{ km s}^{-1}$. While the stars stick out in this projection, the shown properties are not conserved and it is therefore advisable to also inspect the conserved properties of actions.

The distribution of stars in action space is shown in a view of vertical angular momentum (normalized to the Solar value) and radial action in Fig. 22(c). Most of the stars in this diagram show a similar vertical angular momentum radial action as the Sun ($L_Z = 2038.3 \text{ kpc km s}^{-1}$, $J_R = 7.7 \text{ kpc km s}^{-1}$). Similar to the analyses by Trick et al. (2019), a much richer substructure can be seen when compared to Fig. 22(b). The overdensity of stars around $L_Z \sim 0 \text{ kpc km s}^{-1}$ with higher radial actions is typical for stars of the Galactic halo, especially those of the GES (see e.g. Helmi 2020, and references therein). When looking at the distribution of stellar actions relative to their total actions in Fig. 22(d), it again becomes evident that most stars are on near-circular orbits ($L_Z \sim L_{\text{tot}}$). However, this projection also allows the identification of accreted stars and stars of streams (see e.g. Myeong et al. 2019; Vasiliev 2019; Monty et al.

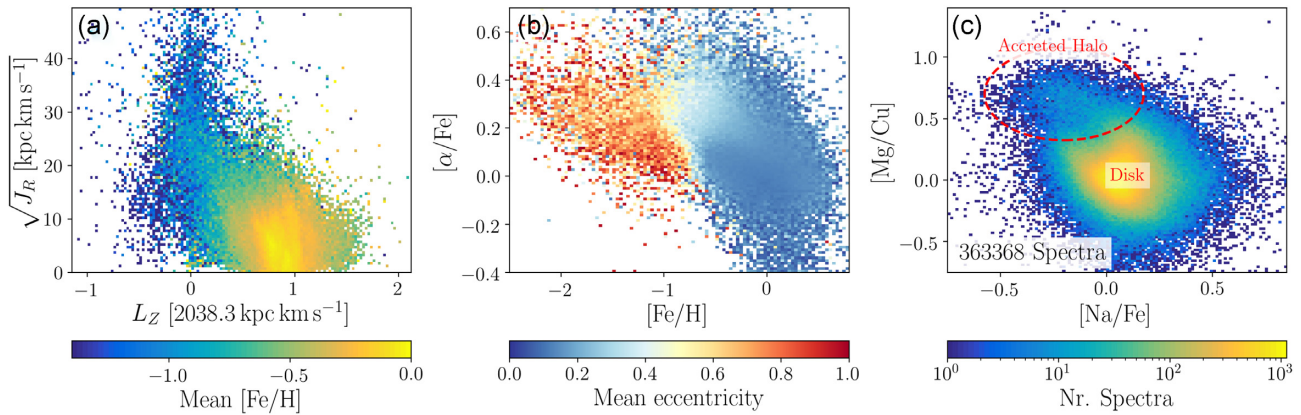


Figure 27. The potential of chemodynamic studies, shown with an overview of actions and abundances. Panel (a) shows the action distribution from Fig. 22(c), but here coloured by mean $[\text{Fe}/\text{H}]$ per bin (see e.g. Trick et al. 2019; Feuillet et al. 2020). Panel (b) shows the Tinsley–Wallerstein diagram, $[\alpha/\text{Fe}]$ over $[\text{Fe}/\text{H}]$ from Fig. 24(j), but here coloured by mean eccentricity per bin (see Mackereth et al. 2019). Panel (c) shows another abundance plane, but the elements Na, Fe, Mg, and Cu tracing different element/nucleosynthesis groups with the majority of GALAH stars around (0,0), where the majority of disc stars is located, and a distinct overdensity of accreted halo stars in the upper left (see Das, Hawkins & Jofré 2020).

2020). Stars of the GES are to be found in the lower corner of this plot, and stars of the Sequoia (Myeong et al. 2019) in the left-hand corner.

It should be noted, that the globular cluster ω Cen, targeted by GALAH and thus part of this data release, sticks out in all panels of Fig. 22 either as overdensity at low $V_T \sim -85 \text{ km s}^{-1}$ in Figs 22(a) and (b) or as streak at $-0.25L_{Z,\odot}$ in Fig. 22(c) and $-0.6J_\phi/J_{\text{tot}}$ in Fig. 22(d). Although beyond the scope of this paper, our release provides new and diverse data to follow up the connection of this globular cluster and possible remnant of a tidally disrupted dwarf galaxy (e.g. Bekki & Freeman 2003) in combination with other stars with similar chemodynamic properties (Myeong et al. 2018) and assess if the streaks are only mainly caused by the high parallax uncertainty of 46 per cent for stars in ω Cen or might coincide with a true extension.

When combining dynamic information (such as actions and eccentricities) with chemistry (like $[\text{Fe}/\text{H}]$ and α -enhancement) in chemodynamic projections, we can see the potential of GALAH+ DR3 in action. Until the recent years, analyses of the Milky Way had usually been performed either from a spectroscopic/chemical or dynamical point of view. Thanks to the advent of *Gaia* and stellar spectroscopic surveys, we can now bring together both disciplines.

In Fig. 27(a), we plot the distributions in action bins coloured by their mean $[\text{Fe}/\text{H}]$. Similar to Fig. 22(c), we see a right substructure, which strongly suggests a correlation of resonances with certain iron abundances. Furthermore, we see a gradient of iron abundance with lower angular momenta dropping from $[\text{Fe}/\text{H}] = -0.13^{+0.20}_{-0.22}$ dex at $1.00^{+0.05}_{-0.05} L_{Z,\odot}$ to $[\text{Fe}/\text{H}] = -0.99^{+0.39}_{-0.47}$ dex at $0.00^{+0.05}_{-0.05} L_{Z,\odot}$. In Fig. 27(b) we plot a chemical overview, coloured by the dynamic property of eccentricity, as performed previously (e.g. Schuster et al. 2012; Mackereth et al. 2019). Here we see that the low- α disc stars are typically on rather circular orbits (with eccentricities well below 0.5), whereas high- α disc stars exhibit higher eccentricities around mean values of 0.5. The most striking feature in this projection is the stars with low $[\text{Fe}/\text{H}]$, which almost exclusively show eccentricities above 0.5 (stars with $[\text{Fe}/\text{H}]$ below -1.0 dex move on orbits with typical eccentricities of $e = 0.70^{+0.23}_{-0.39}$). This is strong evidence that these stars, with chemical composition that are very distinct from the stellar disc and bulge, and orbits very different from the disc are accreted (see discussions in Belokurov et al. 2018; Helmi et al. 2018; Mackereth et al. 2019; Helmi 2020).

That these stars are not only different in their dynamics, can be seen in a chemical projection in Fig. 27(c), where we follow up the distinct chemical signatures of accreted halo stars as found by Nissen & Schuster (2010, 2011) in the projections similar to those proposed by Hawkins et al. (2015) and Das et al. (2020). When assessing different nucleosynthesis channels via different elements, that is Al or Na, α like Mg, and Cu or Mn, the accreted halo stars clearly stick out as a distinct overdensity because of their different chemical enrichment history compared to the majority of the Milky Way disc stars. A follow-up of these findings will be presented in the chemodynamical study of accreted halo stars by S. Buder et al. (in preparation).

9 CONCLUSIONS AND OUTLOOK

With this third data release of the Galactic Archaeology with HERMES (GALAH) survey, we are providing the most complete set of information in terms of chemical composition, dynamics, and stellar ages to the public. The new data provides abundances for up to 30 elements and with the additional astrometric information provided by the *Gaia* satellite, we are able to estimate very precise orbits for almost all stars. These data are extremely valuable for different disciplines of astrophysics and will bring together observers with theorists.

9.1 The data and their usage

In this paper, we describe the methodology behind the newly released data. This release incorporates data from GALAH’s partner surveys, namely the K2/HERMES and TESS-HERMES surveys, yielding a total sample of 678 423 spectra for 588 571 stars. Regarding the use of our data, we conclude:

- (i) Use version 2 of our data catalogues. They include fixes to previously reported erroneous values for the radial velocities `rv_galah` and a new VAC for the cross-match with *Gaia* eDR3 (see Section 7.1 and references therein for more details) updates to the VACs based on the new *Gaia* data.
- (ii) Select the measurement method of v_{rad} based on the science cases from our VAC on v_{rad} . For comparison with other surveys, we recommend preferably `rv_nogr_obst` or otherwise `rv_sme_v2`.

For dynamical studies, we recommend the use of `rv_obst` (including gravitational redshift corrections) if available and report the best measurement for such dynamical studies as `rv_galah` (see Section 7.3.4 for details).

(iii) Use only unflagged measurements of our main stellar parameter quality flag (`flag_sp = 0`).

(iv) Use only unflagged abundance measurements for each element X (`flag_X_fe = 0`). Even in this case, be careful of suspicious abundances and trends, which may not have been caught by our flagging algorithms. Systematic trends may be introduced through inherent limitations of the analysis pipeline. Please consult Section 6 on caveats, including high abundances of V, Co, Rb, Sr, Zr, Mo, Ru, La, Nd, and Sm.

(v) We report both individual as well as stacked visit spectra. The latter result in higher S/N and are generally the preferred values reported per star in the `allstar` catalogues. For studies of individual stars we recommend, however, to also compare all results of individual spectra of the stars from the `allspec` catalogues to confirm that the automatic stacking process was successful (see Section 6.2 for details).

9.2 Scientific avenues for the use of GALAH DR3

Since the advent of galactic archaeology (Freeman & Bland-Hawthorn 2002, and references therein), many large stellar surveys attempt to establish a narrative for the Galaxy by comparing vast amounts of stellar data (ages, kinematics, chemistry) to cosmological N -body + hydrodynamic simulations (e.g. Kobayashi & Nakasato 2011; El-Badry et al. 2018a; Buck et al. 2019). These comparisons assume the present-day Milky Way to be an axisymmetric system in dynamical equilibrium where measurables can be expressed as a function of Galactocentric radius, R (Sharma et al. 2011).

Astronomers have long suspected there is much to learn from examining dynamical perturbations and their dependence on the stellar properties (Minchev et al. 2009; Widrow et al. 2012). We refer this field as Galactic seismology and identify it as a subset of Galactic archaeology. Bland-Hawthorn & Tepper-Garcia (2021, their Appendix A) provide a brief history of Galactic seismology dating back to its first use in 1985. Indeed, in the *Gaia* second data release (DR2) just two years ago (Antoja et al. 2018), a remarkable signature of incomplete phase-mixing was uncovered. If we consider a Galactic cylindrical coordinate frame defined by (R, ϕ, z) , with velocity components (V_R, V_ϕ, V_z) , the *Gaia* team discovered a ‘phase spiral’ in the $z - V_z$ plane. The vertical (z) oscillation frequency is anharmonic so this signal arises from a corrugated wave propagating across the Galactic disc. GALAH has been used to study this phenomenon in terms of stellar ages, actions, and abundances (Bland-Hawthorn et al. 2019; Laporte et al. 2019), with further analyses already under way.

The exact formation of the halo and disc remains enigmatic, but the progress of cosmological simulations is now allowing us to compare properties like the chemical bimodality of the Milky Way’s stellar disc those of simulated galaxies (e.g. Buck 2020; Vincenzo & Kobayashi 2020, and references therein).

The large amount of stellar data provided by stellar spectroscopic surveys is bringing together expertise of previously independent research. Based on our data, the exoplanet community improves our understanding of exoplanets through their host stars with improved stellar parameters (e.g. Clark et al. 2021), more realistic input for planet formation simulations (e.g. Bitsch & Battistini 2020) and will be able to explore exoplanet host stars in a chemokinematic or dynamic context (see e.g. Carrillo et al. 2020).

With the publication of the reduced spectra, we are going another step towards an open data community. Using the spectra will allow other scientists to not only verify our results, but also apply their analyses techniques for parts of the parameter space, for which our own pipeline is not optimized, e.g. the analysis of very hot stars, emission line stars, or very cool stars, among others. Furthermore does the publication of the spectra allow scientists to apply machine learning or clustering algorithms on to the data (see e.g. Price-Jones & Bovy 2019).

Starting from such studies of spatially and dynamically bound groups of stars or solar twins, we are just at the beginning of understanding the correlations for field stars between abundances and orbits (see e.g. Coronado et al. 2020) as well as the abundances and ages for field stars (see e.g. Hayden et al. 2020; Sharma et al. 2020; Morel et al. 2021) as well as their limitations (see e.g. Feltzing et al. 2017; Ness et al. 2018).

9.3 GALAH DR4 and a sharper focus with GALAH Phase 2

We have learned several lessons in the analysis for this data release, which will help us to improve our analysis in the future, that is for the fourth data release of GALAH and thereafter. We have found several interesting trends, of which some are likely astrophysical, while others are not. We will follow these up in the future to hopefully minimize the unphysical trends. Several of these are likely to be addressed by improvements in the reduction of spectra with improved telluric corrections and improved stacking routines. While an in-depth comparison of the data-driven versus model-driven approaches is still to be conducted, first results from our work indicates that a quadratic model reaches its limitations when used to describe a very high-dimensional space, covering the stellar parameters along A-M type stars, as well as 30 element abundances. With the introduction of more higher order models or flexible models and methods, for example neural networks or Gaussian process regression in stellar spectroscopy (Ting et al. 2019; Wang et al. 2021), we believe that such limitations can be overcome and will allow us to further overcome the significant computational costs of on-the-fly spectrum synthesis. A major limitation of all spectroscopic analyses remains with the immensely uncertain oscillator strengths used to create synthetic spectra, with significantly more effort needed. In the future, we aim to not only use improved synthetic model grids, based on 3D non-LTE computations, but also implement these more sophisticated interpolation routines combined with a Bayesian framework. The latter would allow us to include non-spectroscopic information like information from *Gaia* eDR3 and DR3 in a probabilistic way and help us to assess the uncertainties of our estimates more reliably.

One of the most limiting bottlenecks of Galactic archaeology are the still significant uncertainties of stellar ages which can be estimated to no better than 10 per cent (Soderblom 2010), but are typically significantly higher. With the start of GALAH Phase 2, for which we adjust our target selection to observe more main-sequence turn-off stars to get more reliable age estimates, we also adjusted our observing strategy with longer exposure time to achieve higher spectral quality (and thus higher accuracy and precision). These adjustments will help us to more efficiently collect high-dimensional data of stars in our Solar vicinity and provide the community with a promising data set of chemistry, dynamics, and reliable ages.

ACKNOWLEDGEMENTS

Based on data acquired through the Australian Astronomical Observatory, under programmes: A/2013B/13 (The GALAH pilot survey);

A/2014A/25, A/2015A/19, A2017A/18 (The GALAH survey phase 1), A2018 A/18 (Open clusters with HERMES), A2019A/1 (Hierarchical star formation in Ori OB1), A2019A/15 (The GALAH survey phase 2), A/2015B/19, A/2016A/22, A/2016B/10, A/2017B/16, A/2018B/15 (The HERMES-TESS program), and A/2015A/3, A/2015B/1, A/2015B/19, A/2016A/22, A/2016B/12, A/2017A/14, (The HERMES K2-follow-up program). We acknowledge the traditional owners of the land on which the AAT stands, the Gamilaraay people, and pay our respects to elders past, present, and emerging.

This work has made use of data from the European Space Agency (ESA) mission *Gaia* (<http://www.cosmos.esa.int/gaia>), processed by the *Gaia* Data Processing and Analysis Consortium (DPAC, <http://www.cosmos.esa.int/web/gaia/dpac/consortium>). Funding for the DPAC has been provided by national institutions, in particular the institutions participating in the *Gaia* Multilateral Agreement. This publication makes use of data products from the Two Micron All Sky Survey, which is a joint project of the University of Massachusetts and the Infrared Processing and Analysis Center/California Institute of Technology, funded by the National Aeronautics and Space Administration and the National Science Foundation. This work was supported by the Australian Research Council Centre of Excellence for All Sky Astrophysics in 3 Dimensions (ASTRO 3D), through project number CE170100013 and the Swedish strategic research programme eSSANCE. This work was supported by computational resources provided by the Australian Government through the National Computational Infrastructure (NCI) under the National Computational Merit Allocation Scheme (project y89).

The following software and programming languages made this research possible: IRAF (Tody 1986, 1993), CONFIGURE (Miszalski et al. 2006), TOPCAT (version 4.4; Taylor 2005); Python (version 3.7) and its packages ASTROPY (version 2.0; Astropy Collaboration 2013, 2018), SCIPY (Virtanen et al. 2001), MATPLOTLIB (Hunter 2007), PANDAS (version 0.20.2; McKinney 2011), NUMPY (Walt, Colbert & Varoquaux 2011), IPYTHON (Pérez & Granger 2007), and GALPY (version 1.3; Bovy 2015). This research has made use of the VizieR catalogue access tool, CDS, Strasbourg, France. The original description of the VizieR service was published in A&AS 143, 23. This research made use of the TOPCAT tool, described in Taylor (2005). This publication makes use of data products from the Two Micron All Sky Survey, which is a joint project of the University of Massachusetts and the Infrared Processing and Analysis Center/California Institute of Technology, funded by the National Aeronautics and Space Administration and the National Science Foundation.

SB and KL acknowledge funds from the Alexander von Humboldt Foundation in the framework of the Sofja Kovalevskaja Award endowed by the Federal Ministry of Education and Research. SB acknowledges travel support from Universities Australia and Deutsche Akademische Austauschdienst. JK and TZ acknowledge financial support of the Slovenian Research Agency (research core funding No. P1-0188) and the European Space Agency (PRODEX Experiment Arrangement No. C4000127986). AMA acknowledges support from the Swedish Research Council (VR 2016-03765), and the project grants ‘The New Milky Way’ (KAW 2013.0052) and ‘Probing charge- and mass-transfer reactions on the atomic level’ (KAW 2018.0028) from the Knut and Alice Wallenberg Foundation. KL acknowledges funds from the European Research Council (ERC) under the European Union’s Horizon 2020 research and innovation programme (Grant agreement No. 852977). KCF acknowledges support from the Australian Research Council under award number DP160103747. LS acknowledges financial support from the Australian Research Council (Discovery Project 170100521) and

from the Australian Research Council Centre of Excellence for All Sky Astrophysics in 3 Dimensions (ASTRO 3D), through project number CE170100013. CK acknowledges funding from the UK Science and Technology Facility Council (STFC) through grant ST/R000905/1, and the Stromlo Distinguished Visitorship at the ANU. DMN acknowledges support from NASA under award Number 80NSSC19K0589, and support from the Allan C. And Dorothy H. Davis Fellowship. YST is supported by the NASA Hubble Fellowship grant *HST*-HF2-51425 awarded by the Space Telescope Science Institute. GT was supported by the project grant ‘The New Milky Way’ from the Knut and Alice Wallenberg foundation and by the grant 2016-03412 from the Swedish Research Council. GT acknowledges financial support of the Slovenian Research Agency (research core funding No. P1-0188 and project N1-0040). MŽ acknowledges funding from the Australian Research Council (grant DP170102233).

We thank Chris Onken for cross-matching GALAH and SkyMapper DR3 data (see Onken et al. 2019, for more information). We thank Kareem El-Badry for providing a vetted version of wide binaries from *Gaia* DR2 data and GALAH+ DR3 radial velocities. We thank Alvin Gavel and Andreas J. Korn for bringing the bug in SME 536 to our attention. We thank Scott Trager and many other colleagues who started a discussion about acknowledging the pioneering work by Beatrice M. Tinsley. We thank the SDSS collaboration and APOGEE team for their efforts in documentation, which greatly benefited our efforts in documentation and validation.

DATA AVAILABILITY

The data underlying this article are available in the Data Central at https://cloud.datacentral.org.au/teamdata/GALAH/public/GALAH_DR3/ and can be accessed with the unique identifier `galah_dr3` for this release and `subject_id` for each spectrum. For more information (including the single object viewer options and bulk downloads) we refer the reader to the Data Central documentation at <https://docs.datacentral.org.au/galah/dr3/overview/>.

REFERENCES

- Ahumada R. et al., 2020, *ApJS*, 249, 3
 Amarsi A. M., Asplund M., 2017, *MNRAS*, 464, 264
 Amarsi A. M., Barklem P. S., Asplund M., Collet R., Zatsarinny O., 2018b, *A&A*, 616, A89
 Amarsi A. M., Barklem P. S., Collet R., Grevesse N., Asplund M., 2019, *A&A*, 624, A111
 Amarsi A. M., Lind K., Asplund M., Barklem P. S., Collet R., 2016, *MNRAS*, 463, 1518
 Amarsi A. M., Nordlander T., Barklem P. S., Asplund M., Collet R., Lind K., 2018a, *A&A*, 615, A139
 Amarsi A. M. et al., 2020, *A&A*, 642, A62
 Antoja T. et al., 2018, *Nature*, 561, 360
 Asplund M., 2005, *ARA&A*, 43, 481
 Asplund M., Grevesse N., Sauval A. J., Scott P., 2009, *ARA&A*, 47, 481
 Astropy Collaboration, 2013, *A&A*, 558, A33
 Astropy Collaboration, 2018, *AJ*, 156, 123
 Bailer-Jones C. A. L., Rybizki J., Foesneau M., Demleitner M., Andrae R., 2021, *AJ*, 161, 147
 Bailer-Jones C. A. L., Rybizki J., Foesneau M., Mantelet G., Andrae R., 2018, *AJ*, 156, 58
 Baratella M. et al., 2020, *A&A*, 634, A34
 Barbay B., Chiappini C., Gerhard O., 2018, *ARA&A*, 56, 223
 Bard A., Kock A., Kock M., 1991, *A&A*, 248, 315
 Bard A., Kock M., 1994, *A&A*, 282, 1014

- Barden S. C. et al., 2010, in McLean I. S., Ramsay S. K., Takami H., eds, Proc. SPIE Conf. Ser. Vol. 7735, Ground-based and Airborne Instrumentation for Astronomy III. SPIE, Bellingham, p. 773509
- Bastian N., Lardo C., 2018, *ARA&A*, 56, 83
- Bate M. R., 2019, *MNRAS*, 484, 2341
- Baumgardt H., Hilker M., Sollima A., Bellini A., 2019, *MNRAS*, 482, 5138
- Bedding T. R. et al., 2010, *ApJ*, 713, L176
- Bedell M. et al., 2018, *ApJ*, 865, 68
- Bekki K., Freeman K. C., 2003, *MNRAS*, 346, L11
- Belokurov V., Erkal D., Evans N. W., Koposov S. E., Deason A. J., 2018, *MNRAS*, 478, 611
- Bensby T., Feltzing S., Oey M. S., 2014, *A&A*, 562, A71
- Bensby T., Lind K., 2018, *A&A*, 615, A151
- Bergemann M. et al., 2019, *A&A*, 631, A80
- Bertelli Motta C. et al., 2018, *MNRAS*, 478, 425
- Biemont E., Grevesse N., Hanaforf P., Lowe R. M., 1981, *ApJ*, 248, 867
- Binney J., 2012, *MNRAS*, 426, 1324
- Bitsch B., Battistini C., 2020, *A&A*, 633, A10
- Blackwell-Whitehead R. J., Lundberg H., Nave G., Pickering J. C., Jones H. R. A., Lyubchik Y., Pavlenko Y. V., Viti S., 2006, *MNRAS*, 373, 1603
- Blackwell D. E., Booth A. J., Menon S. L. R., Petford A. D., 1986, *MNRAS*, 220, 289
- Blackwell D. E., Ibbetson P. A., Petford A. D., Shallis M. J., 1979, *MNRAS*, 186, 633
- Blackwell D. E., Menon S. L. R., Petford A. D., 1983, *MNRAS*, 204, 883
- Blackwell D. E., Petford A. D., Shallis M. J., Simmons G. J., 1982a, *MNRAS*, 199, 43
- Blackwell D. E., Petford A. D., Simmons G. J., 1982b, *MNRAS*, 201, 595
- Bland-Hawthorn J., Gerhard O., 2016, *ARA&A*, 54, 529
- Bland-Hawthorn J., Tepper-Garcia T., 2021, *MNRAS*, 504, 3168
- Bland-Hawthorn J. et al., 2019, *MNRAS*, 486, 1167
- Boesgaard A. M., Tripicco M. J., 1986, *ApJ*, 302, L49
- Bonaca A., Conroy C., Wetzel A., Hopkins P. F., Kereš D., 2017, *ApJ*, 845, 101
- Bonanno A., Schlattl H., Paternò L., 2002, *A&A*, 390, 1115
- Bovy J., 2015, *ApJS*, 216, 29
- Bressan A., Marigo P., Girardi L., Salasnich B., Dal Cero C., Rubele S., Nanni A., 2012, *MNRAS*, 427, 127
- Brewer J. M., Fischer D. A., Valenti J. A., Piskunov N., 2016, *ApJS*, 225, 32
- Brzeski J., Case S., Gers L., 2011, in Hatheway A. E., ed., *Proc. SPIE Conf. Ser. Vol. 8125, Optomechanics 2011: Innovations and Solutions*. SPIE, Bellingham, p. 812504
- Buck T., 2020, *MNRAS*, 491, 5435
- Buck T., Ness M., Obreja A., Macciò A. V., Dutton A. A., 2019, *ApJ*, 874, 67
- Buder S. et al., 2018, *MNRAS*, 478, 4513
- Buder S. et al., 2019, *A&A*, 624, A19
- Burbidge E. M., Burbidge G. R., Fowler W. A., Hoyle F., 1957, *Rev. Mod. Phys.*, 29, 547
- Cantat-Gaudin T., Anders F., 2020, *A&A*, 633, A99
- Cardon B. L., Smith P. L., Scalo J. M., Testerman L., Whaling W., 1982, *ApJ*, 260, 395
- Carlsson J., Sturesson L., Svanberg S., 1989, *Z. Phys. D Atoms Molecules Clusters*, 11, 287
- Carretta E., Bragaglia A., Gratton R., D'Orazi V., Lucatello S., 2009b, *A&A*, 508, 695
- Carretta E. et al., 2009a, *A&A*, 505, 117
- Carrillo A., Hawkins K., Bowler B. P., Cochran W., Vanderburg A., 2020, *MNRAS*, 491, 4365
- Casagrande L., Ramírez J., Meléndez J., Bessell M., Asplund M., 2010, *A&A*, 512, A54
- Casagrande L., Schönrich R., Asplund M., Cassisi S., Ramírez I., Meléndez J., Bensby T., Feltzing S., 2011, *A&A*, 530, A138
- Casagrande L., Vandenberg D. A., 2014, *MNRAS*, 444, 392
- Casagrande L., Vandenberg D. A., 2018, *MNRAS*, 475, 5023
- Casagrande L. et al., 2020, preprint ([arXiv:2011.02517](https://arxiv.org/abs/2011.02517))
- Casey A. R. et al., 2017, *ApJ*, 840, 59
- Casey A. R. et al., 2019, *ApJ*, 880, 125
- Cescutti G., Molaro P., Fu X., 2020, *Mem. Soc. Astron. Ital.*, 91, 153
- Chang T. N., Tang X., 1990, *J. Quant. Spec. Radiat. Transf.*, 43, 207
- Clark J. T. et al., 2020, preprint ([arXiv:2008.05372](https://arxiv.org/abs/2008.05372))
- Corliss C. H., Bozman W. R., 1962, Experimental transition probabilities for spectral lines of seventy elements; derived from the NBS Tables of spectral-line intensities. NBS Monograph Vol. 53. US Government Printing Office, Washington, D.C.
- Coronado J., Rix H.-W., Trick W. H., El-Badry K., Rybizki J., Xiang M., 2020, *MNRAS*, 495, 4098
- Cui X.-Q. et al., 2012, *Res. Astron. Astrophys.*, 12, 1197
- Cutri R. M. et al., 2014, VizieR Online Data Catalog, p. 2328
- D'Orazi V., Gratton R., Lucatello S., Carretta E., Bragaglia A., Marino A. F., 2010, *ApJ*, 719, L213
- Dalton G. et al., 2018, in Evans C. J., Simard L., Takami H., eds., *Proc. SPIE Conf. Ser. Vol. 10702, Ground-based and Airborne Instrumentation for Astronomy VII*. SPIE, Bellingham, p. 107021B
- Das P., Hawkins K., Jofré P., 2020, *MNRAS*, 493, 5195
- Davidson M. D., Snoek L. C., Volten H., Doenszelmann A., 1992, *A&A*, 255, 457
- de Grijs R., Wicker J. E., Bono G., 2014, *AJ*, 147, 122
- de Jong R. S. et al., 2019, *Messenger*, 175, 3
- De Laverny P., Recio-Blanco A., Worley C. C., Plez B., 2012, *A&A*, 544, A126
- Deng L.-C. et al., 2012, *Res. Astron. Astrophys.*, 12, 735
- Den Hartog E. A., Lawler J. E., Sneden C., Cowan J. J., 2003, *ApJS*, 148, 543
- Den Hartog E. A., Lawler J. E., Sobeck J. S., Sneden C., Cowan J. J., 2011, *ApJS*, 194, 35
- Den Hartog E. A., Ruffoni M. P., Lawler J. E., Pickering J. C., Lind K., Brewer N. R., 2014, *ApJS*, 215, 23
- De Silva G. M. et al., 2015, *MNRAS*, 449, 2604
- Donor J. et al., 2020, *AJ*, 159, 199
- Dutra-Ferreira L., Pasquini L., Smljanic R., Porto de Mello G. F., Steffen M., 2016, *A&A*, 585, A75
- Edgar M. L. et al., 2018, in Navarro R., Geyl R., eds, Proc. SPIE Conf. Ser. Vol. 10706, Advances in Optical and Mechanical Technologies for Telescopes and Instrumentation III. SPIE, Bellingham, p. 1070633
- Edvardsson B., Andersen J., Gustafsson B., Lambert D. L., Nissen P. E., Tomkin J., 1993, *A&A*, 275, 101
- El-Badry K., Rix H.-W., 2018, *MNRAS*, 480, 4884
- El-Badry K., Rix H.-W., Ting Y.-S., Weisz D. R., Bergemann M., Cargile P., Conroy C., Eilers A.-C., 2018a, *MNRAS*, 473, 5043
- El-Badry K. et al., 2018b, *MNRAS*, 476, 528
- ESA ed., 1997, The HIPPARCOS and TYCHO catalogues. Astrometric and photometric star catalogues derived from the ESA HIPPARCOS Space Astrometry Mission, Vol. 1200. ESA Special Publication, Paris
- Ester M., Krieger H.-p., Jorg S., Xu X., 1996, in Simoudis E., Han J., Fayyad U., eds., Proc. of 2nd Intern. Conf. on KDD. AAAI Press, Portland, p. 226
- Fabricius C. et al., 2021, *A&A*, 649, A5
- Farrell T. J., Birchall M. N., Heald R. W., Shortridge K., Vuong M. V., Sheinis A. I., 2014, in Chiozzi G., Radziwill N. M., eds, *Proc. SPIE Conf. Ser. Vol. 9152, Software and Cyberinfrastructure for Astronomy III*. SPIE, Bellingham, p. 915223
- Feltzing S., Howes L. M., McMillan P. J., Stokutė E., 2017, *MNRAS*, 465, L109
- Feuillet D. K., Feltzing S., Sahlholdt C. L., Casagrande L., 2020, *MNRAS*, 497, 109
- Feuillet D. K. et al., 2018, *MNRAS*, 477, 2326
- Fossati L., Bagnulo S., Landstreet J., Wade G., Kochukhov O., Monier R., Weiss W., Gebran M., 2008, *A&A*, 483, 891
- Fossati L., Bagnulo S., Monier R., Khan S. A., Kochukhov O., Landstreet J., Wade G., Weiss W., 2007, *A&A*, 476, 911
- Frankel N., Rix H.-W., Ting Y.-S., Ness M., Hogg D. W., 2018, *ApJ*, 865, 96
- Freeman K., Bland-Hawthorn J., 2002, *ARA&A*, 40, 487
- Froese Fischer C., Tachiev G., Irimia A., 2006, *At. Data Nucl. Data Tables*, 92, 607

- Fuhr J. R., Martin G. A., Wiese W. L., 1988, *J. Phys. Chem. Ref. Data*, 17, 504
- Gaia Collaboration, 2016a, *A&A*, 595, A1
- Gaia Collaboration, 2016b, *A&A*, 595, A2
- Gaia Collaboration, 2018, *A&A*, 616, A1
- Gaia Collaboration, 2021, *A&A*, 649, A1
- Gallagher A. J., Bergemann M., Collet R., Plez B., Leenaerts J., Carlsson M., Yakovleva S. A., Belyaev A. K., 2020, *A&A*, 634, A55
- Gao X. et al., 2018, *MNRAS*, 481, 2666
- Gao X. et al., 2020, *MNRAS*, 497, L30
- Garz T., 1973, *A&A*, 26, 471
- Gilmore G., Reid N., 1983, *MNRAS*, 202, 1025
- Gilmore G. et al., 2012, *Messenger*, 147, 25
- Gravity Collaboration, 2019, *A&A*, 625, L10
- Grevesse N., Asplund M., Sauval A. J., 2007, *Space Sci. Rev.*, 130, 105
- Grevesse N., Blackwell D. E., Petford A. D., 1989, *A&A*, 208, 157
- Grevesse N., Scott P., Asplund M., Sauval A. J., 2015, *A&A*, 573, A27
- Gurtovenko E. A., Sheminova V. A., 2015, preprint ([arXiv:1505.00975](https://arxiv.org/abs/1505.00975))
- Gustafsson B., Edvardsson B., Eriksson K., Jørgensen U. G., Nordlund Å., Plez B., 2008, *A&A*, 486, 951
- Harris W. E., 1996, *AJ*, 112, 1487
- Hawkins K., Jofré P., Masseron T., Gilmore G., 2015, *MNRAS*, 453, 758
- Hawkins K. et al., 2016, *A&A*, 592, A70
- Hayden M. R., Recio-Blanco A., de Laverny P., Mikolaitis S., Worley C. C., 2017, *A&A*, 608, L1
- Hayden M. R. et al., 2015, *ApJ*, 808, 132
- Hayden M. R. et al., 2020, *MNRAS*, 493, 2952
- Haywood M., Di Matteo P., Lehnert M. D., Katz D., Gómez A., 2013, *A&A*, 560, A109
- Haywood M., Snaith O., Lehnert M. D., Di Matteo P., Khoperskov S., 2019, *A&A*, 625, A105
- Heijmans J. et al., 2012, in McLean I. S., Ramsay S. K., Takami H., eds, Proc. SPIE Conf. Ser. Vol. 8446, Ground-based and Airborne Instrumentation for Astronomy IV. SPIE, Bellingham, p. 84460W
- Heiter U., 2020, *IAUGA*, 30, 458
- Heiter U., Jofré P., Gustafsson B., Korn A. J., Soubiran C., Thévenin F., 2015b, *A&A*, 582, A49
- Heiter U. et al., 2015a, *Phys. Scr.*, 90, 054010
- Heiter U. et al., 2021, *A&A*, 645, A106
- Helmi A., 2020, *ARA&A*, 58, 205
- Helmi A., Babusiaux C., Koppelman H. H., Massari D., Veljanoski J., Brown A. G. A., 2018, *Nature*, 563, 85
- Henden A. A., Levine S., Terrell D., Welch D., 2015, *AAS*, 225, 336.16
- Henden A. A., Levine S. E., Terrell D., Smith T. C., Welch D., 2012, *J. Am. Assoc. Var. Star Obs.*, 40, 430
- Hibbert A., Biemont E., Godefroid M., Vaecq N., 1993, *A&AS*, 99, 179
- Ho A. Y. Q. et al., 2017, *ApJ*, 836, 5
- Holtzman J. A. et al., 2018, *AJ*, 156, 125
- Hon M., Stello D., García R. A., Mathur S., Sharma S., Colman I. L., Bugnet L., 2019, *MNRAS*, 485, 5616
- Huber D., Stello D., Bedding T. R., Chaplin W. J., Arentoft T., Quirion P. O., Kjeldsen H., 2009, *Commun. Asteroseismol.*, 160, 74
- Huber D. et al., 2017, *ApJ*, 844, 102
- Hunter J. D., 2007, *Comput. Sci. Eng.*, 9, 90
- Jofré P., Heiter U., Soubiran C., 2019, *ARA&A*, 57, 571
- Jofré P., Heiter U., Tucci Maia M., Soubiran C., Worley C. C., Hawkins K., Blanco-Cuaresma S., Rodrigo C., 2018, *Res. Notes Am. Astron. Soc.*, 2, 152
- Jofré P. et al., 2014, *A&A*, 564, A133
- Jofré P. et al., 2015, *A&A*, 582, A81
- Jofré P. et al., 2017, *A&A*, 601, A38
- Jönsson H. et al., 2020, *AJ*, 160, 120
- Jurić M. et al., 2008, *ApJ*, 673, 864
- Karovicova I., White T. R., Nordlander T., Casagrande L., Ireland M., Huber D., Jofré P., 2020, *A&A*, 640, A25
- Karovicova I. et al., 2018, *MNRAS*, 475, L81
- Kausch W. et al., 2015, *A&A*, 576, A78
- Kelleher D. E., Podobedova L. I., 2008, *J. Phys. Chem. Ref. Data*, 37, 709
- Kjeldsen H., Bedding T. R., 1995, *A&A*, 293, 87
- Kobayashi C., Karakas A. I., Lugaro M., 2020, *ApJ*, 900, 179
- Kobayashi C., Nakasato N., 2011, *ApJ*, 729, 16
- Kock M., Richter J., 1968, *ZA*, 69, 180
- Kollmeier J. A. et al., 2017, preprint ([arXiv:1711.03234](https://arxiv.org/abs/1711.03234))
- Kos J. et al., 2017, *MNRAS*, 464, 1259
- Kos J. et al., 2018, *MNRAS*, 473, 4612
- Kumar Y. B., Reddy B. E., Campbell S. W., Maben S., Zhao G., Ting Y.-S., 2020, *Nat. Astron.*, 4, 1059
- Kurucz R. L., 2006, Database of observed and predicted atomic transitions
- Kurucz R. L., 2007, Database of observed and predicted atomic transitions
- Kurucz R. L., 2008, Database of observed and predicted atomic transitions
- Kurucz R. L., 2009, Database of observed and predicted atomic transitions
- Kurucz R. L., 2010, Database of observed and predicted atomic transitions
- Kurucz R. L., 2013, Database of observed and predicted atomic transitions
- Kurucz R. L., 2014, Database of observed and predicted atomic transitions
- Laporte C. F. P., Minchev I., Johnston K. V., Gómez F. A., 2019, *MNRAS*, 485, 3134
- Lawler J. E., Bonvallet G., Sneden C., 2001a, *ApJ*, 556, 452
- Lawler J. E., Dakin J. T., 1989, *J. Opt. Soc. Am. B Opt. Phys.*, 6, 1457
- Lawler J. E., Den Hartog E. A., Sneden C., Cowan J. J., 2006, *ApJS*, 162, 227
- Lawler J. E., Guzman A., Wood M. P., Sneden C., Cowan J. J., 2013, *ApJS*, 205, 11
- Lawler J. E., Sneden C., Cowan J. J., 2015, *ApJS*, 220, 13
- Lawler J. E., Sneden C., Cowan J. J., Ivans I. I., Den Hartog E. A., 2009, *ApJS*, 182, 51
- Lawler J. E., Sneden C., Nave G., Den Hartog E. A., Emrahoğlu N., Cowan J. J., 2017, *ApJS*, 228, 10
- Lawler J. E., Wickliffe M. E., den Hartog E. A., Sneden C., 2001b, *ApJ*, 563, 1075
- Lawler J. E., Wood M. P., Den Hartog E. A., Feigenson T., Sneden C., Cowan J. J., 2014, *ApJS*, 215, 20
- Leenaerts J., Carlsson M., 2009, in Lites B., Cheung M., Magara T., Mariska J., Reeves K., eds, ASP Conf. Ser. Vol. 415, The Second Hinode Science Meeting. Astron. Soc. Pac., San Francisco, p. 87
- Lewis I. J. et al., 2002, *MNRAS*, 333, 279
- Lindgren L., 2018, GAIA-C3-TN-LU-LL-124-01: Re-normalising the astrometric chi-square in Gaia DR2
- Lindgren L. et al., 2018, *A&A*, 616, A2
- Lindgren L. et al., 2021a, *A&A*, 649, A4
- Lindgren L. et al., 2021b, *A&A*, 649, A2
- Lind K., Asplund M., Barklem P. S., 2009, *A&A*, 503, 541
- Lind K., Asplund M., Barklem P. S., Belyaev A. K., 2011, *A&A*, 528, A103
- Lind K. et al., 2017, *MNRAS*, 468, 4311
- Liu F., Asplund M., Yong D., Feltzing S., Dotter A., Meléndez J., Ramírez I., 2019, *A&A*, 627, A117
- Liu F., Asplund M., Yong D., Meléndez J., Ramírez I., Karakas A. I., Carlos M., Marino A. F., 2016b, *MNRAS*, 463, 696
- Liu F., Yong D., Asplund M., Ramírez I., Meléndez J., 2016a, *MNRAS*, 457, 3934
- Mackereth J. T., Bovy J., 2018, *PASP*, 130, 114501
- Mackereth J. T. et al., 2019, *MNRAS*, 482, 3426
- Majewski S. R., Zasowski G., Nidever D. L., 2011, *ApJ*, 739, 25
- Mamajek E. E., 2012, *ApJ*, 754, L20
- Marigo P. et al., 2017, *ApJ*, 835, 77
- Martell S. et al., 2020, preprint ([arXiv:2006.02106](https://arxiv.org/abs/2006.02106))
- Martell S. L. et al., 2017, *MNRAS*, 465, 3203
- Martig M. et al., 2015, *MNRAS*, 451, 2230
- Martin G., Fuhr J., Wiese W., 1988, *J. Phys. Chem. Ref. Data Suppl.*, 17, 1
- May A., Binney J., 1986, *MNRAS*, 221, 857
- May M., Richter J., Wichelmann J., 1974, *A&AS*, 18, 405
- McKinney W., 2010, in van der Walt S., Millman J., eds., Proceedings of the 9th Python in Science Conference, Austin, p. 55
- McMillan P. J., 2017, *MNRAS*, 465, 76
- Meggers W. F., Corliss C. H., Scribner B. F., 1975, Tables of spectral-line intensities. Part I, II- arranged by elements. NBS, Chicago, IL
- Meléndez J., Barbuy B., 2009, *A&A*, 497, 611

- Merle T. et al., 2017, *A&A*, 608, A95
- Mészáros S. et al., 2013, *AJ*, 146, 133
- Mihalas D., Athay R. G., 1973, *ARA&A*, 11, 187
- Minchev I., Quillen A. C., Williams M., Freeman K. C., Nordhaus J., Siebert A., Bienaymé O., 2009, *MNRAS*, 396, L56
- Minchev I., Steinmetz M., Chiappini C., Martig M., Anders F., Matijevec G., de Jong R. S., 2017, *ApJ*, 834, 27
- Miszalski B., Shortridge K., Saunders W., Parker Q. A., Croom S. M., 2006, *MNRAS*, 371, 1537
- Moe M., Kratter K. M., Badenes C., 2019, *ApJ*, 875, 61
- Molaro P., Cescutti G., Fu X., 2020, *MNRAS*, 496, 2902
- Monty S., Venn K. A., Lane J. M. M., Lokhorst D., Yong D., 2020, *MNRAS*, 497, 1236
- Morel T., Creevey O. L., Montalbán J., Miglio A., Willett E., 2021, *A&A*, 646, A78
- Munari U., Zwitter T., 1997, *A&A*, 318, 269
- Myeong G. C., Evans N. W., Belokurov V., Sanders J. L., Koposov S. E., 2018, *MNRAS*, 478, 5449
- Myeong G. C., Vasiliev E., Iorio G., Evans N. W., Belokurov V., 2019, *MNRAS*, 488, 1235
- Nahar S. N., 1993, *Phys. Scr.*, 48, 297
- Nandakumar G. et al., 2020, preprint (arXiv:2011.02783)
- Ness M., Hogg D. W., Rix H.-W., Ho A. Y. Q., Zasowski G., 2015, *ApJ*, 808, 16
- Ness M. et al., 2018, *ApJ*, 853, 198
- Nissen P. E., 2015, *A&A*, 579, A52
- Nissen P. E., Gustafsson B., 2018, *A&AR*, 26, 6
- Nissen P. E., Schuster W. J., 2010, *A&A*, 511, L10
- Nissen P. E., Schuster W. J., 2011, *A&A*, 530, A15
- Nissen P. E., Schuster W. J., 2012, *A&A*, 543, A28
- Nitz D. E., Kunau A. E., Wilson K. L., Lentz L. R., 1999, *ApJS*, 122, 557
- Nitz D. E., Wickliffe M. E., Lawler J. E., 1998, *ApJS*, 117, 313
- Nordlander T., Lind K., 2017, *A&A*, 607, A75
- Nordström B. et al., 2004, *A&A*, 418, 989
- O'brian T. R., Lawler J. E., 1991, *Phys. Rev. A*, 44, 7134
- O'Brian T. R., Wickliffe M. E., Lawler J. E., Whaling W., Brault J. W., 1991, *J. Opt. Soc. Am B Opt. Phys.*, 8, 1185
- Onken C. A. et al., 2019, *Publ. Astron. Soc. Aust.*, 36, e033
- Osorio Y., Allende Prieto C., Hubeny I., Mészáros S., Shetrone M., 2020, *A&A*, 637, A80
- Osorio Y., Barklem P. S., Lind K., Belyaev A. K., Spielfiedel A., Guitou M., Feautrier N., 2015, *A&A*, 579, A53
- Osorio Y., Lind K., Barklem P. S., Allende Prieto C., Zatsariny O., 2019, *A&A*, 623, A103
- Palmeri P., Quinet P., Lundberg H., Engström L., Nilsson H., Hartman H., 2017, *MNRAS*, 471, 532
- Palmeri P., Quinet P., Wyart J.-F., Biémont E., 2000, *Phys. Scr.*, 61, 323
- Perryman M. A. C. et al., 1997, *A&A*, 323, L49
- Pérez F., Granger B. E., 2007, *Comput. Sci. Eng.*, 9, 21
- Piskunov N., Valenti J. A., 2017, *A&A*, 597, A16
- Pitrou C., Coc A., Uzan J.-P., Vangioni E., 2018, *Phys. Rep.*, 754, 1
- Price-Jones N., Bovy J., 2019, *MNRAS*, 487, 871
- Price-Jones N. et al., 2020, *MNRAS*, 496, 5101
- Price-Whelan A. M. et al., 2020, *ApJ*, 895, 2
- Prša A. et al., 2016, *AJ*, 152, 41
- Raassen A. J. J., Uylings P. H. M., 1998, *A&A*, 340, 300
- Ralchenko Y., Kramida A., Reader J., NIST ASD Team, 2010, NIST Atomic Spectra Database (ver. 4.0.0), [Online]
- Ramírez I., Allende Prieto C., 2011, *ApJ*, 743, 135
- Ramírez I., Fish J. R., Lambert D. L., Allende Prieto C., 2012, *ApJ*, 756, 46
- Reggiani H. et al., 2019, *A&A*, 627, A177
- Reid M. J., Brunthaler A., 2004, *ApJ*, 616, 872
- Riello M. et al., 2021, *A&A*, 649, A3
- Rix H.-W., Bovy J., 2013, *A&AR*, 21, 61
- Ruffoni M. P., Den Hartog E. A., Lawler J. E., Brewer N. R., Lind K., Nave G., Pickering J. C., 2014, *MNRAS*, 441, 3127
- Salaris M., Cassisi S., 2006, *Evolution of Stars and Stellar Populations*. J. Wiley, Hoboken, NJ
- Savage B. D., Mathis J. S., 1979, *ARA&A*, 17, 73
- Schlegel D. J., Finkbeiner D. P., Davis M., 1998, *ApJ*, 500, 525
- Schönrich R., Binney J., Dehnen W., 2010, *MNRAS*, 403, 1829
- Schuster W. J., Moreno E., Nissen P. E., Pichardo B., 2012, *A&A*, 538, A21
- Semenova E. et al., 2020, *A&A*, 643, A164
- Sharma S., Bland-Hawthorn J., Johnston K. V., Binney J., 2011, *ApJ*, 730, 3
- Sharma S., Stello D., Bland-Hawthorn J., Huber D., Bedding T. R., 2016, *ApJ*, 822, 15
- Sharma S. et al., 2014, *ApJ*, 793, 51
- Sharma S. et al., 2018, *MNRAS*, 473, 2004
- Sharma S. et al., 2019, *MNRAS*, 490, 5335
- Sharma S. et al., 2020, preprint (arXiv:2011.13818)
- Sheinis A. et al., 2015, *J. Astron. Telesc. Instrum. Syst.*, 1, 035002
- Simpson J. D. et al., 2020, preprint (arXiv:2011.02659)
- Skrutskie M. F. et al., 2006, *AJ*, 131, 1163
- Smette A. et al., 2015, *A&A*, 576, A77
- Smiljanic R. et al., 2014, *A&A*, 570, A122
- Smith G., 1988, *J. Phys. B*, 21, 2827
- Smith G., Raggett D. S. J., 1981, *J. Phys. B At. Mol. Phys.*, 14, 4015
- Sobeck J. S., Lawler J. E., Sneden C., 2007, *ApJ*, 667, 1267
- Soderblom D. R., 2010, *ARA&A*, 48, 581
- Souto D. et al., 2018, *ApJ*, 857, 14
- Souto D. et al., 2019, *ApJ*, 874, 97
- Spina L., Meléndez J., Karakas A. I., Ramírez I., Monroe T. R., Asplund M., Yong D., 2016, *A&A*, 593, A125
- Spina L. et al., 2020, *ApJ*, 895, 52
- Spina L. et al., 2021, *MNRAS*, 503, 3279
- Spite F., Spite M., 1982, *A&A*, 115, 357
- Stassun K. G. et al., 2019, *AJ*, 158, 138
- Steinmetz M. et al., 2020a, *AJ*, 160, 82
- Steinmetz M. et al., 2020b, *AJ*, 160, 83
- Stello D. et al., 2015, *ApJ*, 809, L3
- Stello D. et al., 2017, *ApJ*, 835, 83
- Takada M. et al., 2014, *PASJ*, 66, R1
- Tautvaišienė G., Barisevičius G., Chorniy Y., Ilyin I., Puzeras E., 2013, *MNRAS*, 430, 621
- Taylor M. B., 2005, in Shopbell P., Britton M., Ebert R., eds, ASP Conf. Ser. Vol. 347, *Astronomical Data Analysis Software and Systems XIV*. Astron. Soc. Pac., San Francisco, p. 29
- Ting Y.-S., Conroy C., Rix H.-W., 2016, *ApJ*, 816, 10
- Ting Y.-S., Conroy C., Rix H.-W., Asplund M., 2018, *ApJ*, 860, 159
- Ting Y.-S., Conroy C., Rix H.-W., Cargile P., 2019, *ApJ*, 879, 69
- Ting Y.-S., Weinberg D. H., 2021, preprint (arXiv:2102.04992)
- Tinsley B. M., 1979, *ApJ*, 229, 1046
- Tinsley B. M., 1980, *Fund. Cosmic Phys.*, 5, 287
- Tody D., 1986, in Crawford D. L., ed., Proc. SPIE Conf. Ser. Vol. 627, *Instrumentation in Astronomy VI*. SPIE, Bellingham, p. 733
- Tody D., 1993, in Hanisch R. J., Brissenden R. J. V., Barnes J., eds, ASP Conf. Vol. 52, *Astronomical Data Analysis Software and Systems II*. Astron. Soc. Pac., San Francisco, p. 173
- Torra F. et al., 2021, *A&A*, 649, A10
- Traven G. et al., 2017, *ApJS*, 228, 24
- Traven G. et al., 2020, *A&A*, 638, A145
- Trick W. H., Coronado J., Rix H.-W., 2019, *MNRAS*, 484, 3291
- Trubko R., Gregoire M. D., Holmgren W. F., Cronin A. D., 2017, *Phys. Rev. A*, 95, 052507
- Vaeck N., Godefroid M., Hansen J. E., 1988, *Phys. Rev. A*, 38, 2830
- Valenti J. A., Piskunov N., 1996, *A&AS*, 118, 595
- van der Maaten L., Hinton G., 2008, *J. Mach. Learn. Res.*, 9, 2579
- van Dokkum P. G., 2001, *PASP*, 113, 1420
- van Leeuwen F., 2007, *A&A*, 474, 653
- Vasiliev E., 2019, *MNRAS*, 484, 2832
- Vincenzo F., Kobayashi C., 2020, *MNRAS*, 496, 80
- Virtanen P. et al., 2020, *Nature Methods*, 17, 261
- Wallerstein G., 1962, *ApJS*, 6, 407
- Walt S. v. d., Colbert S. C., Varoquaux G., 2011, *Comput. Sci. Eng.*, 13, 22

Wang E. X., Nordlander T., Asplund M., Amarsi A. M., Lind K., Zhou Y., 2021, *MNRAS*, 500, 2159
 Wheeler A. et al., 2020, *ApJ*, 898, 58
 Wickliffe M. E., Salih S., Lawler J. E., 1994, *J. Quant. Spec. Radiat. Transf.*, 51, 545
 Widrow L. M., Gardner S., Yanny B., Dodelson S., Chen H.-Y., 2012, *ApJ*, 750, L41
 Wittenmyer R. A. et al., 2018, *AJ*, 155, 84
 Wittenmyer R. A. et al., 2020, *MNRAS*, 496, 851
 Wood M. P., Lawler J. E., Sneden C., Cowan J. J., 2013, *ApJS*, 208, 27
 Wood M. P., Lawler J. E., Sneden C., Cowan J. J., 2014, *ApJS*, 211, 20
 Xiang M.-S. et al., 2020, *ApJ*, 898, 28
 Xiang M. et al., 2019, *ApJS*, 245, 34
 Yanny B. et al., 2009, *AJ*, 137, 4377
 Yan Z.-C., Tambasco M., Drake G. W. F., 1998, *Phys. Rev. A*, 57, 1652
 Yoshii Y., 1982, *PASJ*, 34, 365
 Zacharias N., Finch C. T., Girard T. M., Henden A., Bartlett J. L., Monet D. G., Zacharias M. I., 2013, *AJ*, 145, 44
 Zhao G., Zhao Y.-H., Chu Y.-Q., Jing Y.-P., Deng L.-C., 2012, *Res. Astron. Astrophys.*, 12, 723
 Zinn J. C. et al., 2020, *ApJS*, 251, 23

Zwitter T. et al., 2018, *MNRAS*, 481, 645
 Zwitter T. et al., 2020, preprint ([arXiv:2012.12201](https://arxiv.org/abs/2012.12201))

SUPPORTING INFORMATION

Supplementary data are available at *MNRAS* online.

suppl_data

Please note: Oxford University Press is not responsible for the content or functionality of any supporting materials supplied by the authors. Any queries (other than missing material) should be directed to the corresponding author for the article.

APPENDIX A: LINELIST, REFERENCE VALUES, AND TABLE SCHEMA OF THE MAIN CATALOGUE

Here we append all additional information used for the analysis.

Table A1. Selected lines for the elemental abundance analysis. The full table is available online as supplementary material.

Elem.	Ion	Wavelength (Å)	LEP (eV)	log (gf)	Reference	Line mask (Å)	Segment mask (Å)
Li	1	6707.7635	0.00000	-0.00200000	1998PhRvA...57.1652Y	6707.3000-6708.3000	6705.76-6709.76
Li	1	6707.9145	0.00000	-0.303000	1998PhRvA...57.1652Y	6707.3000-6708.3000	6705.76-6709.76
Li	1	6707.9215	0.00000	-0.00200000	1998PhRvA...57.1652Y	6707.3000-6708.3000	6705.76-6709.76
Li	1	6708.0725	0.00000	-0.303000	1998PhRvA...57.1652Y	6707.3000-6708.3000	6705.76-6709.76
C	1	6587.6100	8.53700	-1.02100	1993A&AS...99..179H	6587.2610-6587.9860	6585.61-6589.61
O	1	7771.9440	9.14600	0.369000	NIST	7771.3590-7772.5090	7769.50-7777.50
O	1	7774.1660	9.14600	0.223000	NIST	7773.5220-7774.7820	7769.50-7777.50
O	1	7775.3880	9.14600	0.00200000	NIST	7774.9120-7775.9620	7769.50-7777.50
Na	1	5682.6333	2.10200	-0.706000	GESMCHF	5682.5170-5682.9970	5680.63-5691.20
Na	1	5688.2050	2.10400	-0.404000	GESMCHF	5687.9170-5688.3920	5680.63-5691.20
Mg	1	5711.0880	4.34600	-1.72400	1990JQSRT...43..207C	5710.7570-5711.4280	5710.00-5713.09
Al	1	6696.0230	3.14300	-1.56900	2008JPCRD...37..709K	6695.7780-6696.1730	6695.00-6699.87
Al	1	6698.6730	3.14300	-1.87000	2008JPCRD...37..709K	6698.3920-6698.8950	6695.00-6699.87
Al	1	7835.3090	4.02200	-0.689000	2008JPCRD...37..709K	7834.8840-7835.5720	7834.00-7837.50
Al	1	7836.1340	4.02200	-0.534000	2008JPCRD...37..709K	7835.8130-7836.4310	7834.00-7837.50
Al	1	7836.1340	4.02200	-1.83400	2008JPCRD...37..709K	7835.8130-7836.4310	7834.00-7837.50
...

Note. References: 1982ApJ...260..395C: Cardon et al. (1982), 1983MNRAS.204..883B|1989A&A...208..157G: Blackwell, Menon & Petford (1983), Grevesse, Blackwell & Petford (1989), 1990JQSRT...43..207C: Chang & Tang (1990), 1992A&A...255..457D: Davidson et al. (1992), 1993A&AS...99..179H: Hibbert et al. (1993), 1993PhysS...48..297N: Nahar (1993), 1998PhRvA...57.1652Y: Yan, Tambasco & Drake (1998), 1999ApJS...122..557N: Nitz et al. (1999), 2008JPCRD...37..709K: Kelleher & Podobedova (2008), 2009A&A...497..611M: Meléndez & Barbuy (2009), 2009A&A...497..611M:solar-gf: Meléndez & Barbuy (2009), 2014ApJS...211...20W: Wood et al. (2014), 2014ApJS...215...20L: Lawler et al. (2014), 2014ApJS...215...23D: Den Hartog et al. (2014), 2014MNRAS.441.3127R: Ruffoni et al. (2014), 2015ApJS...220...13L: Lawler et al. (2015), 2015ApJS...220...13L: 1982ApJ...260..395C: Lawler et al. (2015), Cardon et al. (1982), 2017MNRAS.471..532P: Palmeri et al. (2017), 2017PhRvA...95e2507T: Trubko et al. (2017), BGHL: Biemont et al. (1981), BIPS: Blackwell et al. (1979), BK: Bard & Kock (1994), BK+BWL: Bard & Kock (1994), O'Brian et al. (1991), BK+GESB82c+BWL: Bard & Kock (1994), Blackwell, Petford & Simmons (1982b), O'Brian et al. (1991), BKK: Bard, Kock & Kock (1991), BKK+GESB82c+BWL: Bard et al. (1991), Blackwell et al. (1982a), O'Brian et al. (1991), BLNP: Blackwell-Whitehead et al. (2006), BWL: O'Brian et al. (1991), BWL+2014MNRAS.441.3127R: O'Brian et al. (1991), Ruffoni et al. (2014), BWL+GESHRL14: O'Brian et al. (1991), Den Hartog et al. (2014), CB: Corliss & Bozman (1962), DLSSC: Den Hartog et al. (2011), FMW: Fuhr, Martin & Wiese (1988), GARZ|BL: Garz (1973), O'brian & Lawler (1991), GESB82c+BWL: Blackwell et al. (1982a), O'Brian et al. (1991), GESB86: Blackwell et al. (1986), GESB86+BWL: Blackwell et al. (1986), O'Brian et al. (1991), GESMCHF: Froese Fischer, Tachiev & Irimia (2006), Grevesse2015: Grevesse et al. (2015), HLSC: Den Hartog et al. (2003), K06: Kurucz (2006), K07: Kurucz (2007), K08: Kurucz (2008), K09: Kurucz (2009), K10: Kurucz (2010), K13: Kurucz (2013), K14: Kurucz (2014), KL-astro: astrophysical, KR|1989ZPhyD...11..287C: Kock & Richter (1968), Carlsson, Sturesson & Svanberg (1989), LBS: Lawler, Bonvallet & Sneden (2001a), LD: Lawler & Dakin (1989), LD-HS: Lawler et al. (2006), LGWSC: Lawler et al. (2013), LSCI: Lawler et al. (2009), LWHS: Lawler et al. (2001b), MA-astro: astrophysical, MC: Meggers, Corliss & Scribner (1975), MFW: Martin, Fuhr & Wiese (1988), MRW: May, Richter & Wichelmann (1974), NIST: Ralchenko et al. (2010), NWL: Nitz, Wickliffe & Lawler (1998), PQWB: Palmeri et al. (2000), RU: Raassen & Uylings (1998), S: Smith (1988), SLS: Sobek, Lawler & Sneden (2007), SR: Smith & Raggatt (1981), VGH: Vaeck, Godefroid & Hansen (1988), WLSC: Wood et al. (2013), WSL: Wickliffe, Salih & Lawler (1994).

Table A2. Reference values for Sun from GALAH DR3 (this work), Asplund et al. (2009), and APOGEE DR16 VESTA (Ahumada et al. 2020). $[M/H]$ is the pseudo-iron abundance sme.feh for GALAH DR3 and $M.H$ from APOGEE DR16. For APOGEE DR16 we use the a quadratic sum of v_{macro} and $v_{\text{sin } i}$ as v_{broad} value. We use values from the SDSS website, computed via $[X/Fe] = [X/M] - [Fe/M]$ for the Vesta abundances of O, Na, V, and Ce.

Element	λ (Å-)	$A(X_{\odot})$	$A(X_{\odot})$	$[X/Fe]$	$[X/Fe]$	$[X/Fe]$	$[X/Fe]$
		GALAH DR3 Zero point	Asplund et al. (2009) Photosphere	GALAH DR3 Skyflat	GALAH DR3 Solar Circle	APOGEE DR16 VESTA	APOGEE DR16 Overlap
Fe	combined	7.38	7.50 ± 0.04	0.00 ± 0.04	−0.00 ± 0.06	−0.00 ± 0.01	−0.05 ± 0.14
alpha	combined	–	–	−0.00 ± 0.02	0.01 ± 0.05	−0.01 ± 0.01	0.02 ± 0.07
Li	6708	1.05	1.05 ± 0.10	–	1.16 ± 0.49	–	–
C	6588	8.45	8.43 ± 0.05	–	0.02 ± 0.10	0.02 ± 0.02	−0.02 ± 0.12
O	combined	8.77	8.69 ± 0.05	−0.12 ± 0.05	0.05 ± 0.14	0.05 ± –	0.14 ± 0.22
Na	combined	6.06	6.24 ± 0.04	0.01 ± 0.02	−0.00 ± 0.10	−0.01 ± –	0.09 ± 0.20
Mg	5711	7.60	7.60 ± 0.04	0.00 ± 0.03	0.01 ± 0.09	−0.00 ± 0.01	0.00 ± 0.10
Al	combined	6.41	6.45 ± 0.03	−0.00 ± 0.02	0.03 ± 0.10	0.01 ± 0.02	0.10 ± 0.15
Si	combined	7.47	7.51 ± 0.03	−0.02 ± 0.03	0.00 ± 0.06	−0.00 ± 0.01	0.03 ± 0.11
K	7699	5.07	5.03 ± 0.09	−0.09 ± 0.04	0.02 ± 0.15	−0.07 ± 0.03	0.03 ± 0.23
Ca	combined	6.18	6.34 ± 0.04	0.00 ± 0.03	0.03 ± 0.08	−0.01 ± 0.02	0.07 ± 0.12
Sc	combined	3.16	3.15 ± 0.04	−0.00 ± 0.02	0.02 ± 0.08	–	–
Ti	combined	–	4.95 ± 0.05	−0.01 ± 0.03	0.02 ± 0.07	−0.02 ± 0.05	0.03 ± 0.13
Ti	4758	4.70	4.95 ± 0.05	−0.01 ± 0.03	0.02 ± 0.07	–	–
Ti	4759	4.72	4.95 ± 0.05	−0.01 ± 0.03	0.02 ± 0.07	–	–
Ti	4782	5.04	4.95 ± 0.05	−0.01 ± 0.03	0.02 ± 0.07	–	–
Ti	4802	5.05	4.95 ± 0.05	−0.01 ± 0.03	0.02 ± 0.07	–	–
Ti	4820	4.80	4.95 ± 0.05	−0.01 ± 0.03	0.02 ± 0.07	–	–
Ti	5739	4.82	4.95 ± 0.05	−0.01 ± 0.03	0.02 ± 0.07	–	–
Ti2	combined	–	4.95 ± 0.05	−0.00 ± 0.03	−0.01 ± 0.08	0.11 ± 0.09	−0.01 ± 0.22
Ti2	4720	5.12	4.95 ± 0.05	−0.00 ± 0.03	−0.01 ± 0.08	–	–
Ti2	4765	4.85	4.95 ± 0.05	−0.00 ± 0.03	−0.01 ± 0.08	–	–
Ti2	4799	4.85	4.95 ± 0.05	−0.00 ± 0.03	−0.01 ± 0.08	–	–
Ti2	4866	5.12	4.95 ± 0.05	−0.00 ± 0.03	−0.01 ± 0.08	–	–
V	combined	–	3.93 ± 0.08	−0.01 ± 0.02	0.01 ± 0.19	−0.02 ± –	0.26 ± 0.36
V	4797	3.99	3.93 ± 0.08	−0.01 ± 0.02	0.01 ± 0.19	–	–
V	4832	3.99	3.93 ± 0.08	−0.01 ± 0.02	0.01 ± 0.19	–	–
Cr	combined	5.63	5.64 ± 0.04	−0.00 ± 0.03	−0.05 ± 0.06	0.04 ± 0.06	0.02 ± 0.16
Mn	combined	5.33	5.43 ± 0.04	0.00 ± 0.03	−0.01 ± 0.06	0.05 ± 0.02	−0.01 ± 0.09
Co	combined	–	4.99 ± 0.07	–	0.09 ± 0.27	0.29 ± 0.14	0.03 ± 0.28
Co	5647	5.00	4.99 ± 0.07	–	0.09 ± 0.27	–	–
Co	6490	4.85	4.99 ± 0.07	–	0.09 ± 0.27	–	–
Co	6632	4.93	4.99 ± 0.07	–	0.09 ± 0.27	–	–
Co	7713	5.06	4.99 ± 0.07	–	0.09 ± 0.27	–	–
Ni	combined	–	6.22 ± 0.04	0.01 ± 0.02	−0.05 ± 0.08	0.02 ± 0.02	0.01 ± 0.10
Ni	5847	6.23	6.22 ± 0.04	0.01 ± 0.02	−0.05 ± 0.08	–	–
Ni	6586	6.23	6.22 ± 0.04	0.01 ± 0.02	−0.05 ± 0.08	–	–
Cu	combined	–	4.19 ± 0.04	0.01 ± 0.02	−0.01 ± 0.10	−0.05 ± 0.07	0.02 ± 0.25
Cu	5700	3.74	4.19 ± 0.04	0.01 ± 0.02	−0.01 ± 0.10	–	–
Cu	5782	4.06	4.19 ± 0.04	0.01 ± 0.02	−0.01 ± 0.10	–	–
Zn	combined	–	4.56 ± 0.05	−0.03 ± 0.03	−0.03 ± 0.10	–	–
Zn	4722	4.49	4.56 ± 0.05	−0.03 ± 0.03	−0.03 ± 0.10	–	–
Zn	4811	4.46	4.56 ± 0.05	−0.03 ± 0.03	−0.03 ± 0.10	–	–
Rb	7800	2.60	2.52 ± 0.10	–	−0.08 ± 0.28	–	–
Sr	6550	3.30	2.87 ± 0.07	–	0.50 ± 0.37	–	–
Y	combined	2.14	2.21 ± 0.05	−0.23 ± 0.05	−0.02 ± 0.18	–	–
Y	4855	2.13	2.21 ± 0.05	−0.23 ± 0.05	−0.02 ± 0.18	–	–
Y	4884	2.09	2.21 ± 0.05	−0.23 ± 0.05	−0.02 ± 0.18	–	–
Zr	combined	–	2.58 ± 0.04	–	0.14 ± 0.30	–	–
Zr	4739	2.31	2.58 ± 0.04	–	0.14 ± 0.30	–	–
Zr	4772	2.48	2.58 ± 0.04	–	0.14 ± 0.30	–	–
Zr	4806	2.43	2.58 ± 0.04	–	0.14 ± 0.30	–	–
Zr	4828	2.66	2.58 ± 0.04	–	0.14 ± 0.30	–	–
Zr	5681	3.05	2.58 ± 0.04	–	0.14 ± 0.30	–	–
Mo	combined	–	1.88 ± 0.08	–	0.82 ± 0.42	–	–
Mo	5858	2.65	1.88 ± 0.08	–	0.82 ± 0.42	–	–
Mo	6619	1.92	1.88 ± 0.08	–	0.82 ± 0.42	–	–

Table A2 – *continued*

Element	λ (Å-)	A(X_{\odot}) GALAH DR3 Zero point	A(X_{\odot}) Asplund et al. (2009) Photosphere	[X/Fe] GALAH DR3 Skyflat	[X/Fe] GALAH DR3 Solar Circle	[X/Fe] APOGEE DR16 VESTA	[X/Fe] APOGEE DR16 Overlap
Ru	combined	–	1.75 ± 0.08	–	1.09 ± 0.49	–	–
Ru	4739	2.31	1.75 ± 0.08	–	1.09 ± 0.49	–	–
Ru	4739	2.31	1.75 ± 0.08	–	1.09 ± 0.49	–	–
Ba	combined	2.17	2.18 ± 0.09	–0.14 ± 0.04	–0.00 ± 0.16	–	–
La	combined	–	1.10 ± 0.04	–	0.36 ± 0.21	–	–
La	4749	1.27	1.10 ± 0.04	–	0.36 ± 0.21	–	–
La	4804	1.23	1.10 ± 0.04	–	0.36 ± 0.21	–	–
La	5806	1.13	1.10 ± 0.04	–	0.36 ± 0.21	–	–
Ce	4774	2.14	1.58 ± 0.04	–0.01 ± 0.01	0.12 ± 0.14	–0.11 ± –	–0.05 ± 0.34
Nd	combined	–	1.42 ± 0.04	–	0.37 ± 0.24	–	–
Nd	4811	1.62	1.42 ± 0.04	–	0.37 ± 0.24	–	–
Nd	5812	1.40	1.42 ± 0.04	–	0.37 ± 0.24	–	–
Sm	combined	–	0.96 ± 0.04	–	0.19 ± 0.25	–	–
Sm	4720	1.36	0.96 ± 0.04	–	0.19 ± 0.25	–	–
Sm	4848	1.66	0.96 ± 0.04	–	0.19 ± 0.25	–	–
Eu	6645	0.57	0.52 ± 0.04	–	0.13 ± 0.21	–	–

Table A3. Reference values for Sun from GALAH DR3 (this work, from skyflats), literature, and APOGEE DR16 VESTA (Ahumada et al. 2020). The literature is a combination of IAU Solar values (Prša et al. 2016), ages from Bonanno et al. (2002), $M_{\text{bol}, \odot}$ from Mamajek (2012), velocity estimates (v_{mic} and v_{broad}) from Jofré et al. (2018), and abundances from Asplund et al. (2009). [M/H] is the pseudo-iron abundance sme.feh for GALAH DR3 and M_{H} from APOGEE DR16. For APOGEE DR16 we use the a quadratic sum of v_{macro} and $v_{\text{sin } i}$ as v_{broad} value. We use values from the SDSS website, computed via $[X/\text{Fe}] = [X/M] - [\text{Fe}/M]$ for the Vesta abundances of O, Na, V, and Ce.

Parameter	Unit	GALAH DR3	Literature	APOGEE DR16
T_{eff}	(K)	5779 ± 69	5772 ± –	5712 ± 115
log g	(dex)	4.42 ± 0.18	4.438 ± –	4.40 ± 0.08
[M/H]	(dex)	0.01 ± 0.06	0.00 ± –	0.00 ± 0.01
[Fe/H]	(dex)	0.00 ± 0.04	0.00 ± –	–0.00 ± 0.01
Mass	(M_{\odot})	0.97 ± –	1.00 ± –	–
Age	(Gyr)	5.83 ± –	4.57 ± 0.11	–
$M_{\text{bol}, \odot}$	(mag)	–	4.7554 ± 0.0004	–
L_{bol}	($L_{\text{bol}, \odot}$)	1.01 ± –	1.00 ± –	–
v_{mic}	(km s^{-1})	1.16 ± –	1.74 ± –	0.94 ± –
v_{broad}	(km s^{-1})	6.52 ± 2.06	–	5.85 ± –

Table A4. Reference values for Arcturus from GALAH DR3 (this work), Ramirez+11 (Ramírez & Allende Prieto 2011), and APOGEE DR16 (Ahumada et al. 2020). [M/H] is the pseudo-iron abundance sme.feh for GALAH DR3, not reported by Ramírez & Allende Prieto (2011) and M_{H} from APOGEE DR16. For APOGEE DR16 we use the reported v_{macro} as v_{broad} value, because their was no $v_{\text{sin } i}$ fitted.

Parameter	Unit	GALAH DR3	Ramirez+11	APOGEE DR16
T_{eff}	(K)	4289 ± 69	4286 ± 30	4292 ± 76
log g	(dex)	1.65 ± 0.18	1.66 ± 0.05	1.75 ± 0.06
[M/H]	(dex)	–0.53 ± 0.06	–	–0.53 ± 0.01
[Fe/H]	(dex)	–0.55 ± 0.04	–0.52 ± 0.04	–0.55 ± 0.01
Mass	(M_{\odot})	0.96 ± –	1.08 ± 0.06	–
Age	(Gyr)	9.42 ± –	7.1 $^{+1.5}_{-1.2}$	–
L_{bol}	($L_{\text{bol}, \odot}$)	179.87 ± –	196.94 ± –	–
v_{mic}	(km s^{-1})	1.57 ± –	1.74 ± –	1.43 ± –
v_{broad}	(km s^{-1})	6.20 ± 2.05	–	4.04 ± –
[α /Fe]	(dex)	0.28 ± 0.01	–	0.23 ± 0.01
[Li/Fe]	(dex)	–	–	–
[C/Fe]	(dex)	–	0.43 ± 0.07	0.18 ± 0.01
[O/Fe]	(dex)	0.55 ± 0.05	0.50 ± 0.03	0.24 ± 0.01
[Na/Fe]	(dex)	0.27 ± 0.02	0.11 ± 0.03	–0.03 ± 0.05
[Mg/Fe]	(dex)	0.48 ± 0.03	0.37 ± 0.03	0.25 ± 0.01

Table A4 – continued

Parameter	Unit	GALAH DR3	Ramirez+11	APOGEE DR16
[Al/Fe]	(dex)	0.35 ± 0.02	0.34 ± 0.03	0.14 ± 0.02
[Si/Fe]	(dex)	0.36 ± 0.03	0.33 ± 0.04	0.20 ± 0.01
[K/Fe]	(dex)	0.03 ± 0.04	0.20 ± 0.07	0.16 ± 0.04
[Ca/Fe]	(dex)	0.14 ± 0.03	0.11 ± 0.04	0.10 ± 0.02
[Sc/Fe]	(dex)	0.14 ± 0.02	0.15 ± 0.08	–
[Ti/Fe]	(dex)	0.26 ± 0.02	0.27 ± 0.05	–
[Ti2/Fe]	(dex)	0.19 ± 0.02	0.21 ± 0.04	0.48 ± 0.06
[V/Fe]	(dex)	–	0.20 ± 0.05	–0.07 ± 0.05
[Cr/Fe]	(dex)	–0.11 ± 0.03	–0.05 ± 0.04	–0.03 ± 0.04
[Mn/Fe]	(dex)	–0.19 ± 0.03	–	–0.09 ± 0.02
[Co/Fe]	(dex)	0.09 ± 0.01	0.09 ± 0.04	0.15 ± 0.04
[Ni/Fe]	(dex)	0.13 ± 0.02	0.06 ± 0.03	0.10 ± 0.02
[Cu/Fe]	(dex)	0.19 ± 0.01	–	0.29 ± 0.04
[Zn/Fe]	(dex)	0.05 ± 0.03	0.22 ± 0.06	–
[Rb/Fe]	(dex)	–	–	–
[Sr/Fe]	(dex)	–	–	–
[Y/Fe]	(dex)	–0.40 ± 0.05	–	–
[Zr/Fe]	(dex)	–	–	–
[Mo/Fe]	(dex)	0.03 ± 0.03	–	–
[Ru/Fe]	(dex)	–	–	–
[Ba/Fe]	(dex)	0.04 ± 0.04	–	–
[La/Fe]	(dex)	–	–	–
[Ce/Fe]	(dex)	–0.28 ± 0.00	–	–0.14 ± 0.05
[Nd/Fe]	(dex)	–	–	–
[Sm/Fe]	(dex)	–0.05 ± 0.02	–	–
[Eu/Fe]	(dex)	0.20 ± 0.00	–	–

Table A5. Table schema of version 2 the GALAH DR3 main catalogue for all spectra (GALAH_DR3_main_allspec.v2). All columns are part of the extended main catalogue (allspec) and only a subset of the listed columns are included in the clean version (allstar with only one entry per star). For table schemas of other catalogs (including version 1), we refer the reader to the FITS headers and the table schema website: <https://datacentral.org.au/services/schema/>.

Column name	Units	Description	Data type
star_id	–	2MASS identifier	string
subject_id	–	GALAH identifier	integer
dr2_source_id	–	Gaia DR2 source_id	integer
dr3_source_id	–	Gaia DR3 source_id	integer
survey_name	–	Name of survey as part of GALAH+DR3	string
field_id	–	GALAH fco field	integer
flag_repeat	–	Repeat observation flag, indicating if used for clean catalogue	integer
wg4_field	–	GALAH WG4 field	string
wg4_pipeline	–	SME pipeline version free/lbol/seis	string
flag_sp	–	Stellar parameter quality flag	integer
teff	K	Spectroscopic effective temperature (used for fitting)	float
e_teff	K	Uncertainty teff	float
irfm_teff	K	IRFM temperature (not used for synthesis)	float
irfm_ebv	mag	E(B-V) used for IRFM teff estimation	float
irfm_ebv_ref	–	Reference irfm_ebv	string
cov_e_teff	K	SME covariance fitting uncertainty teff	float
init_teff	K	SME initial teff	float
logg	log(cm.s***-2)	Surface gravity (not fitted via spectra if wg4_pipeline not free)	float
e_logg	log(cm.s***-2)	Uncertainty logg	float
cov_e_logg	log(cm.s***-2)	MonteCarlo uncertainty logg	float
init_logg	log(cm.s***-2)	SME initial logg	float
fe_h	–	Fe atomic abundance from Fe lines (final, 1D-NLTE)	float
e_fe_h	–	Uncertainty fe_h	float
cov_e_fe_h	–	SME covariance fitting uncertainty fe_h	float
flag_fe_h	–	Quality flag fe_h	integer
fe_h_atmo	–	sme.feh from stellar parameter run, fitted from H, Ti, Sc, Fe	float
e_fe_h_atmo	–	Uncertainty fe_h_atmo	float

Table A5 – continued

Column name	Units	Description	Data type
cov_e_fe_h_atmo	–	SME covariance fitting uncertainty sme.feh	float
init_fe_h_atmo	–	SME initial sme.feh	float
vmic	km s ⁻¹	Microturbulence velocity (from empirical relation)	float
vbroad	km s ⁻¹	Broadening velocity (fitted sme.vcini with sme.vmac=0)	float
e_vbroad	km s ⁻¹	Uncertainty of vbroad	float
cov_e_vbroad	km s ⁻¹	SME covariance fitting uncertainty sme.vcini	float
init_vbroad	km s ⁻¹	SME initial broadening velocity	float
mass	solMass	Stellar parameter fitting product of stellar mass	float
lbol	solLum	Stellar parameter fitting product of bolometric luminosity	float
age	Gyr	Stellar parameter fitting product of stellar age	float
chi2_sp	–	Chi2 value of stellar parameter fitting	float
alpha_fe	–	Combined, weighted alpha-process element abundance	float
e_alpha_fe	–	Uncertainty of alpha_fe	float
nr_alpha_fe	–	Bitmask of used measurements for alpha_fe	float
flag_alpha_fe	–	Quality flag of measurements for alpha_fe	integer
flux_A_Fe	–	Normalized maximum absorption strength of in iron lines	float
chi_A_Fe	–	Chi2 value of iron abundance fitting	float
ind_X1234_fe	dex	Individual uncalibrated measurmenet of line/combo X1234	float
ind_cov_e_X1234	dex	SME covariance fitting uncertainty ind_X1234_fe	float
ind_flag_X1234	–	Quality flag fit for ind_X1234_fe	integer
X_fe	dex	Neutral/ionized X atomic abundance (final, 1D-LTE or NLTE)	float
e_X_fe	dex	Uncertainty X_fe	float
nr_X_fe	–	Bitmask of used X ind lines	integer
flag_X_fe	–	Quality flag of X_fe	integer
ra_dr2	deg	Right Ascension Gaia DR2	float
dec_dr2	deg	Declination Gaia DR2	float
parallax_dr2	mas	propagated from Gaia DR2	float
parallax_error_dr2	mas	propagated from Gaia DR2	float
r_est_dr2	pc	propagated from 2018AJ....156...58B	float
r_lo_dr2	pc	propagated from 2018AJ....156...58B	float
r_hi_dr2	pc	propagated from 2018AJ....156...58B	float
r_len_dr2	pc	propagated from 2018AJ....156...58B	float
rv_galah	–	Best-method radial velocity from GALAH spectra	float
e_rv_galah	–	Uncertainty of rv_galah	float
rv_gaia_dr2	km s ⁻¹	propagated from <i>Gaia</i> DR2	float
e_rv_gaia_dr2	km s ⁻¹	propagated from <i>Gaia</i> DR2	float
red_flag	–	reduction pipeline quality flag	integer
ebv	mag	SFD extinction value	float
snr_c1_iraf	–	Average SNR/px CCD1	float
snr_c2_iraf	–	Average SNR/px CCD2	float
snr_c3_iraf	–	Average SNR/px CCD3	float
snr_c4_iraf	–	Average SNR/px CCD4	float
flag_guess	–	GUESS reduction pipeline quality flag	integer
rv_guess	km s ⁻¹	Reduction pipeline best radial velocity	float
e_rv_guess	km s ⁻¹	Reduction pipeline uncertainty radial velocity	float
teff_guess	K	Reduction pipeline best teff	float
logg_guess	log(cm.s**−2)	Reduction pipeline best logg	float
feh_guess	–	Reduction pipeline best fe_h	float
rv_5854	km s ⁻¹	Local best fit to RV when fitting A(Ba5854)	float
rv_6708	km s ⁻¹	Local best fit to RV when fitting A(Li6708)	float
rv_6722	km s ⁻¹	Local best fit to RV when fitting A(Si6722)	float
v_jk	mag	V magnitude estimated from 2MASS J and Ks mag	float
j_m	mag	propagated from 2MASS	float
j_msgcom	mag	propagated from 2MASS	float
h_m	mag	propagated from 2MASS	float
h_msgcom	mag	propagated from 2MASS	float
ks_m	mag	propagated from 2MASS	float
ks_msgcom	mag	propagated from 2MASS	float
ph_qual_tmass	–	propagated from 2MASS ph_qual	string
w2mpro	mag	propagated from AllWISE	float
w2mpro_error	mag	propagated from AllWISE	float
ph_qual_wise	–	propagated from AllWISE ph_qual	string

Table A5 – continued

Column name	Units	Description	Data type
a_ks	mag	Used Ks band extinction	float
e_a_ks	mag	Uncertainty of a_ks	float
bc_ks	mag	Used Bolometric Correction for Ks band	float
ruwe_dr2	–	propagated from <i>Gaia</i> DR2	float

¹Research School of Astronomy and Astrophysics, Australian National University, ACT 2611, Australia

²Center of Excellence for Astrophysics in Three Dimensions (ASTRO-3D), Australia

³Max Planck Institute for Astronomy (MPIA), Königstuhl 17, D-69117 Heidelberg, Germany

⁴Sydney Institute for Astronomy, School of Physics, A28, The University of Sydney, NSW 2006, Australia

⁵Faculty of Mathematics and Physics, University of Ljubljana, Jadranska 19, 1000 Ljubljana, Slovenia

⁶Theoretical Astrophysics, Department of Physics and Astronomy, Uppsala University, Box 516, SE-751 20 Uppsala, Sweden

⁷Department of Astronomy, Stockholm University, AlbaNova, Roslagstullbacken 21, SE-10691 Stockholm, Sweden

⁸School of Physics, UNSW, Sydney, NSW 2052, Australia

⁹Max Planck Institute for Astrophysics, Karl-Schwarzschild-Str. 1, D-85741 Garching, Germany

¹⁰Monash Centre for Astrophysics, Monash University, Wellington Rd, Clayton, VIC 3800, Australia

¹¹School of Physics and Astronomy, Monash University, Wellington Rd, Clayton, VIC 3800, Australia

¹²Australian Astronomical Optics, Faculty of Science and Engineering, Macquarie University, Macquarie Park, NSW 2113, Australia

¹³Department of Physics and Astronomy, Macquarie University, Sydney, NSW 2109, Australia

¹⁴Istituto Nazionale di Astrofisica, Osservatorio Astronomico di Padova, vicolo dell'Osservatorio 5, I-35122 Padova, Italy

¹⁵Stellar Astrophysics Centre, Department of Physics and Astronomy, Aarhus University, Ny Munkegade 120, DK-8000 Aarhus C, Denmark

¹⁶Macquarie University Research Centre for Astronomy, Astrophysics and Astrophotonics, Sydney, NSW 2109, Australia

¹⁷Leibniz-Institut für Astrophysik Potsdam (AIP), An der Sternwarte 16, D-14482 Potsdam, Germany

¹⁸Centre for Astrophysics, University of Southern Queensland, West Street, Toowoomba, QLD 4350, Australia

¹⁹International Space Science Institute–Beijing, 1 Nanertiao, Zhongguancun, Hai Dian District, Beijing 100190, China

²⁰Lund Observatory, Department of Astronomy and Theoretical Physics, Box 43, SE-221 00 Lund, Sweden

²¹ICRAR, The University of Western Australia, 35 Stirling Highway, Crawley, WA 6009, Australia

²²Kapteyn Astronomical Institute, University of Groningen, Landleven 12, NL-9747 AD Groningen, the Netherlands

²³Centre for Astrophysics Research, Department of Physics, Astronomy and Mathematics, University of Hertfordshire, Hatfield AL10 9AB, UK

²⁴Centre for Astrophysics and Supercomputing, Swinburne University of Technology, Hawthorn, Victoria 3122, Australia

²⁵Center for Astrophysical Sciences and Department of Physics and Astronomy, The Johns Hopkins University, Baltimore, MD 21218, USA

²⁶Department of Astronomy, Columbia University, Pupin Physics Laboratories, New York, NY 10027, USA

²⁷Center for Computational Astrophysics, Flatiron Institute, 162 Fifth Avenue, New York, NY 10010, USA

²⁸Istituto Nazionale di Astrofisica, Osservatorio Astronomico di Padova, vicolo dell'Osservatorio 5, I-35122 Padova, Italy

²⁹Centre for Integrated Sustainability Analysis, School of Physics, The University of Sydney, NSW 2006, Australia

³⁰Institute for Advanced Study, Princeton, NJ 08540, USA

³¹Department of Astrophysical Sciences, Princeton University, Princeton, NJ 08544, USA

³²Observatories of the Carnegie Institution of Washington, 813 Santa Barbara Street, Pasadena, CA 91101, USA

This paper has been typeset from a $\text{\TeX}/\text{\LaTeX}$ file prepared by the author.